LA-UR-12-22389
Approved for public release; distribution is unlimited.

Title:	Simulation and Analysis of Converging Shock Wave Test Problems
Author(s):	Ramsey, Scott D. Shashkov, Mikhail J.
Intended for:	Report

Simulation and Analysis of Converging Shock Wave Test Problems

Scott D. Ramsey, XCP-8
Mikhail J. Shashkov, XCP-4

LA-UR-12-0XXXX

ABSTRACT

Results and analysis pertaining to the simulation of the Guderley converging shock wave test problem (and associated code verification hydrodynamics test problems involving converging shock waves) in the LANL ASC radiation-hydrodynamics code xRAGE are presented. One-dimensional (1D) spherical and two-dimensional (2D) axi-symmetric geometric setups are utilized and evaluated in this study, as is an instantiation of the xRAGE adaptive mesh refinement capability. For the 2D simulations, a 'Surrogate Guderley' test problem is developed and used to obviate subtleties inherent to the true Guderley solution's initialization on a square grid, while still maintaining a high degree of fidelity to the original problem, and minimally straining the general credibility of associated analysis and conclusions.

TABLE OF CONTENTS

I. INTRODUCTION AND PREVIOUS RESULTS

An effort to simulate the Guderley converging shock wave problem (a member of the enhanced Tri-Lab Test Suite or eTLTS[1]) in one or more LANL ASC codes has been ongoing since 2006.[2-4] To date, this effort has culminated in a modern canonical definition of the Guderley test problem[5], and contributions to the Eulerian Applications Project (EAP) including a code verification/spatial convergence rate study using the xRAGE compressible flow solver[6], an implementation of the Guderley problem in the EAP test suite, and the construction of a more comprehensive set of preliminary results[7,8].

.

The Guderley test problem itself is based on the self-similar implosion model first investigated by Guderley[8] (and independently by Sedov and Stanyukovich[9]), and examined in detail by many others, including Lazarus[10] and Ramsey[3]. In this problem, an infinitely strong shock wave of indeterminate origin converges in one-dimensional (1D) cylindrical or spherical symmetry through a polytropic, quiescent, negligible-pressure/specific internal energy (SIE) gas with arbitrary adiabatic index γ and uniform density ρ_0. The shock proceeds to focus on the point or axis of symmetry at $r = 0$ (resulting in ostensibly infinite pressure, velocity, etc.) and reflect back out into the incoming perturbed gas.

Many authors (e.g., Caramana and Whalen[11]) have investigated versions of the Guderley problem in the context of code verification. A recent effort – possibly the first to include a formal spatial convergence analysis of a compressible flow solver using the Guderley problem – was made by Ramsey, et al.[6], using the xRAGE code and 1D spherical symmetry. First order L_1-norm spatial convergence was observed for both the converging and diverging phases of the problem.

The current study is concerned with simulations of the spherically-symmetric Guderley problem, especially on 2D axi-symmetric, square grids with and without adaptive mesh refinement (AMR) capability enabled. To this end, in Sec. II a Guderley-like test problem is introduced to facilitate initialization in LANL ASC codes. Various 1D results are presented and analyzed In Sec. III, and various 2D results are presented and analyzed in Sec. IV. A summary and recommendations for further study are presented in Sec. V; extensive additional content appears in Appendices A-E.

II. DEFINITION OF THE SURROGATE GUDERLEY PROBLEM

The principal concern of this study – the simulation of the spherical Guderley problem on an Eulerian, 2D axi-symmetric, square grid – may present an initialization-related subtlety in addition to those encountered for the Guderley problem on uniform 1D grids.

Since the spherical Guderley velocity field is spherically symmetric, its initialization in a 2D axi-symmetric square grid may, depending on code input archetype, require velocity (v) decomposition and input according to

$$\begin{aligned} \mathrm{v}_r &= \mathrm{v}_R \cos\theta \,, \\ \mathrm{v}_z &= \mathrm{v}_R \sin\theta \,, \end{aligned} \tag{1}$$

where θ denotes the angle between the velocity vector and the cylindrical radial axis, R denotes the spherical radial coordinate, r denotes the cylindrical radial coordinate, and z denotes the cylindrical z-coordinate, such that

$$R^2 = \sqrt{r^2 + z^2}\,. \tag{2}$$

In these cases, where velocity vector initialization is required (as is the case in xRAGE), cell-averaged values corresponding to Eq. (1) must be specified for each computational zone, in addition to remaining consistent cell-averaged flow quantities (e.g., density and SIE). The modification of an existing Guderley exact solution code to provide data of this type represents an ongoing but currently incomplete task.

In parallel with the code development effort, a new, Guderley-like test problem has been developed to circumvent velocity vector initialization. This 'Surrogate Guderley Problem' (SGP) consists of two concentric spherical regions in a $\gamma = 1.4$ gas, is essentially a two-region 'spherical shock tube' (or a 'spherical driven implosion,' as noted by Whalen[12]), and is defined in Table I.

Parameter	Inner spherical region	Outer spherical region
Inner radius	0.0	4.0
Outer radius	4.0	10.0
Initial density	1.0	6.0
Initial specific internal energy (SIE)	1.0e-10	0.06
Initial velocity	0.0	0.0

Table I: Surrogate Guderley problem (SGP) definition. The SGP may be defined using these parameters in any consistent set of units (e.g., cgs, 'HE').

The configuration described in Table I does not result in any known closed-form mathematical solution to the Euler equations, but like the Guderley problem it ultimately results in the formation of a strong converging shock wave that reflects about the spherical origin. While the converging and reflected shocks are in the vicinity of the origin, the SGP is expected to limit – at least in a qualitative sense – to the true Guderley solution.

The SGP is intended to be significantly easier to initialize in compressible flow codes than its conventional counterpart (e.g., on grids not aligned with the Guderley initial velocity vector), and despite the fact that it represents a calculation verification test problem, it is expected to capture the general flow behavior exhibited by the Guderley problem.

II.A. Guderley/Surrogate Guderley Problem Comparison

An effective method for comparing 1D spherical Guderley and SGP simulation results is to plot the converging and reflected shock positions as a function of time for both problems. The Guderley solution for this trajectory [$R_S(t)$] is given by

$$R_S(t) = \begin{cases} k(t_0 - t)^\alpha\,, & t \le t_0 \\ kb(t - t_0)^\alpha\,, & t > t_0 \end{cases} \tag{3}$$

where the similarity exponent $\alpha = 0.717$ and the trajectory multiplier $b = 0.492$ for $\gamma = 1.4$ and spherical symmetry[6]. Equation (2) also contains two arbitrary dimensional constants, the time offset t_0 and the scaling parameter k. Setting these parameters to $t_0 = 14.05$ and $k = 0.58$ (in any consistent set of units) allows the Guderley solution to be scaled to the SGP solution, as shown in Fig. 1. Under this choice of scaling, the two solutions are in close agreement for a wide range of times of interest, but begin to substantially deviate as the SGP shock moves sufficiently far from the origin.

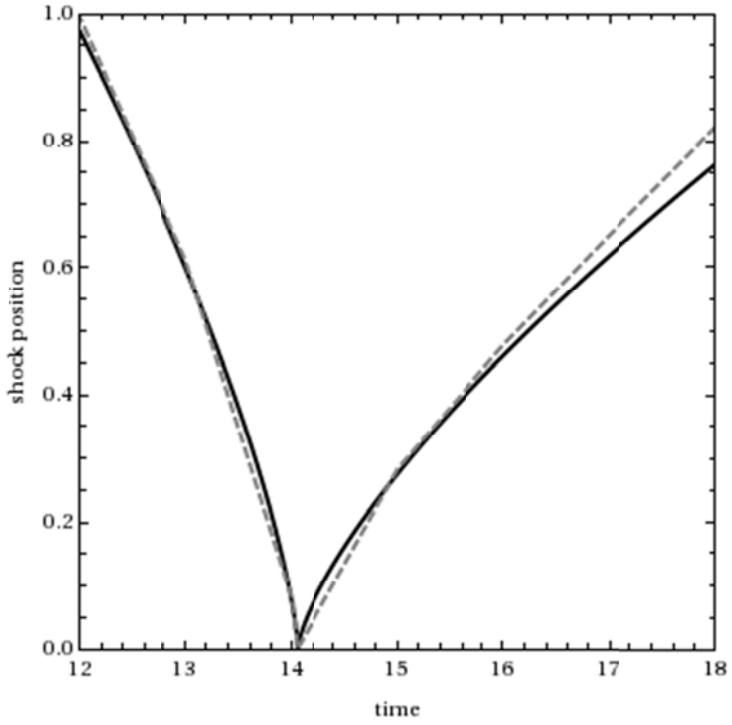

Figure 1: Shock space-time trajectories for the scaled/translated Guderley (solid black line)/surrogate Guderley (dashed gray line) problems.

The values of t_0 and k can also be used to translate and scale the Guderley density (ρ), velocity (u), and pressure (P) profiles for comparison with 1D spherical SGP simulation results. The Guderley solution is given by

$$\begin{aligned} \rho &= \rho_0 g(\xi) \\ u &= \dot{R}_S(t) v(\xi) \\ P &= \rho_0 \dot{R}_S^2(t) \pi(\xi) \\ \xi &= r/\dot{R}_S(t) \end{aligned} \tag{4}$$

where the over-dot represents time differentiation, and g, v, and π are dimensionless functions of the dimensionless independent variable ξ, determined by the solution of a double nonlinear eigenvalue problem depending only on the choice of symmetry and adiabatic index[6]. The members of Eq. (4) are plotted in Fig. 2 for spherical symmetry, $\gamma = 1.4$, $t_0 = 14.05$, $k = 0.58$, and two selected times (with the corresponding SGP results). As was the case in Fig. 1, the two

solutions are in close agreement, but will diverge in accordance with the shock trajectory behavior.

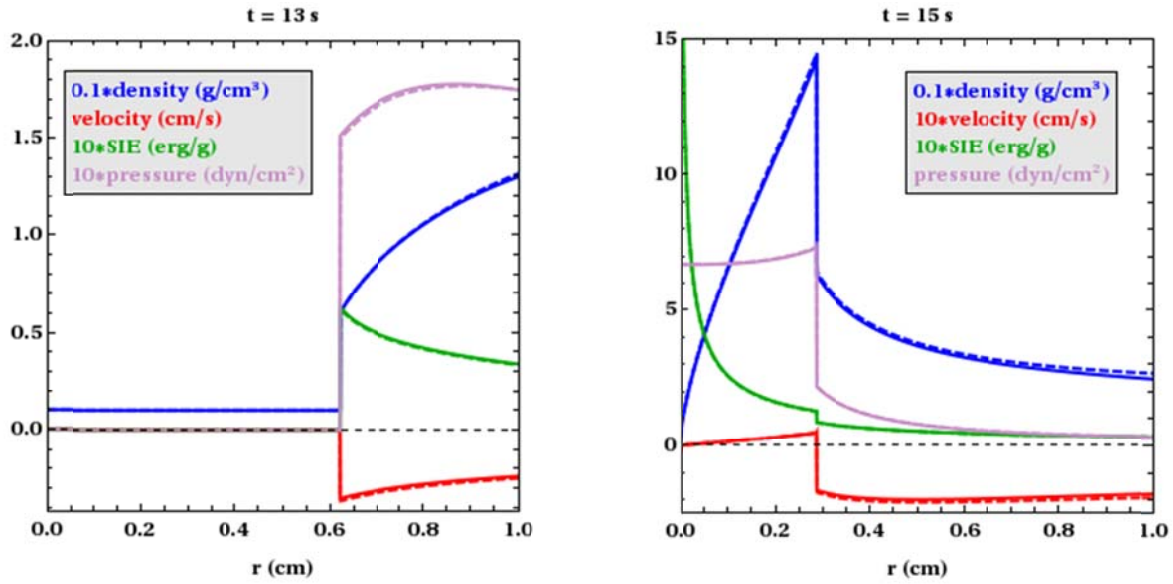

Figure 2: Scaled/translated Guderley (solid)/SGP (dashed) solutions at t = 13 (converging flow) and t = 15 (diverging flow).

In Fig. 2, a truncated 'analysis domain' is being employed. Beyond this radius, the SGP flow begins to couple with additional, non-Guderley (i.e., irrelevant for the purposes of surrogacy) flow features that result from the problem's initialization as a spherical shock tube problem. Figure 2 shows, however, that within the analysis domain (i.e., near $r = 0$, where the SGP solution limits to the Guderley solution) the SGP closely follows a scaled and translated form of the canonical Guderley problem[5], including all major flow features in both the converging and diverging flow regimes.

As the SGP is effectively equivalent to the Guderley problem when the shocks are near $r = 0$, and it is likely easier to initialize in compressible flow codes, it will be used throughout the remainder of this work to provide assessments of the xRAGE compressible flow solver in its simulation of archetypal converging shock wave problems.

III. THE SURROGATE GUDERLEY PROBLEM IN 1D SPHERICAL SYMMETRY

Constructing a 1D spherical SGP setup in xRAGE (v1109.02) represents a mostly trivial exercise (see Appendix E). In all 1D simulations, the following code options were used but are not necessarily unique:

- Code default units (cgs)
- Specific heat c_v = 1.0 erg/(g-eV), so temperature and SIE are equivalent
- Adaptive time step

- Stop time = 20.0 s
- Boundary condition at r = 10 cm: code default (reflective BC[13])
- Initial uniform grid spacing (for calculation verification analysis):
    - dr = 0.02 cm (coarse)
    - dr = 0.01 cm (medium)
    - dr = 0.005 cm (fine)
    - $dr = 0.005/2^9$ cm = 9.765625 x 10^{-6} cm (benchmark)

In each case, the choice of initial grid spacing places the material interface at a zone boundary.

III.A. Uniform Grid

The results of four simulations performed using the above settings (and the four choices of grid spacing dr) are shown in Figs. 3a (an example of convergent flow) and 3b (an example of divergent flow); additional results are provided in Appendix A.

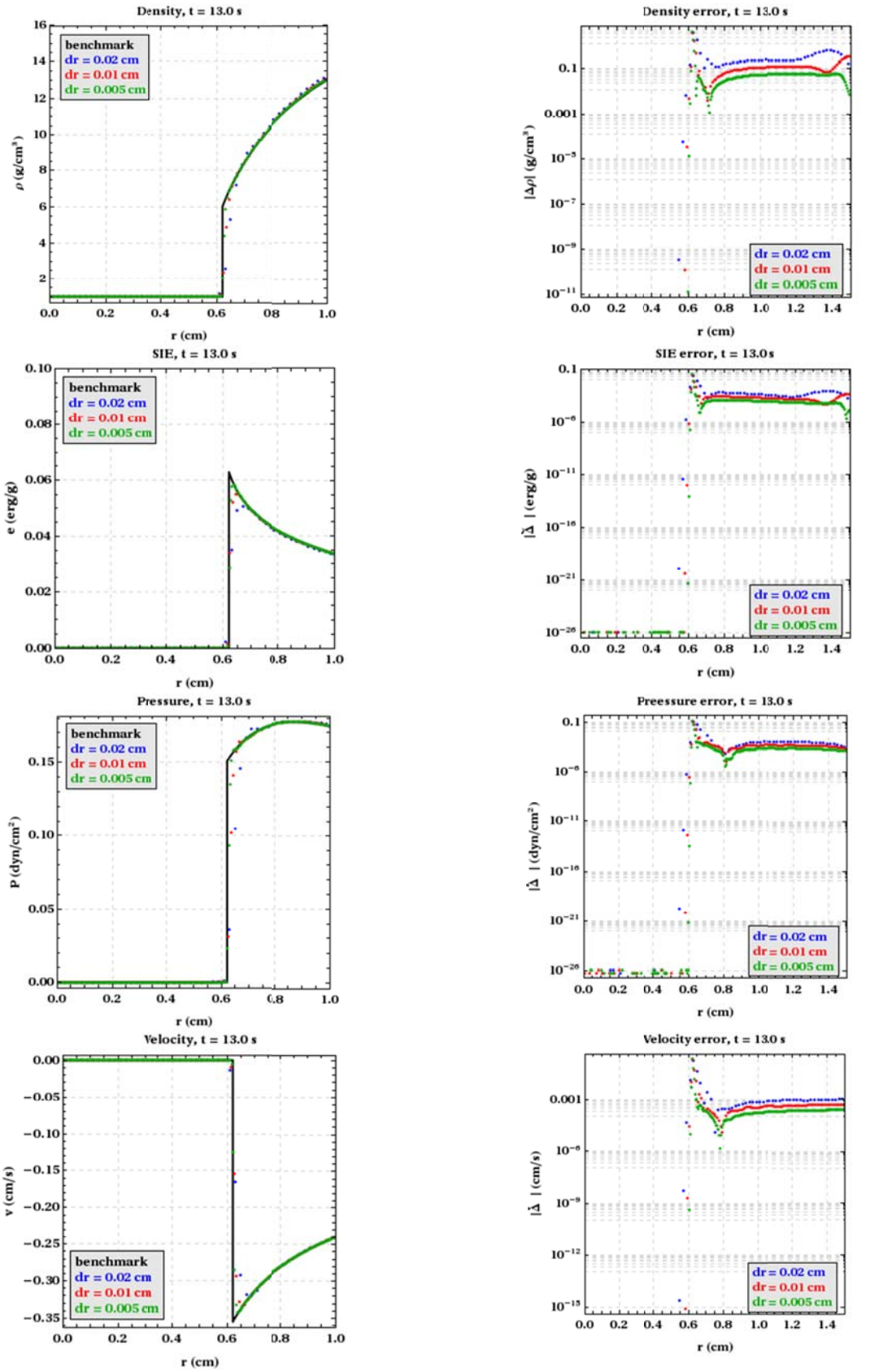

Figure 3a: 1D spherical SGP results at t = 13 s (converging flow).

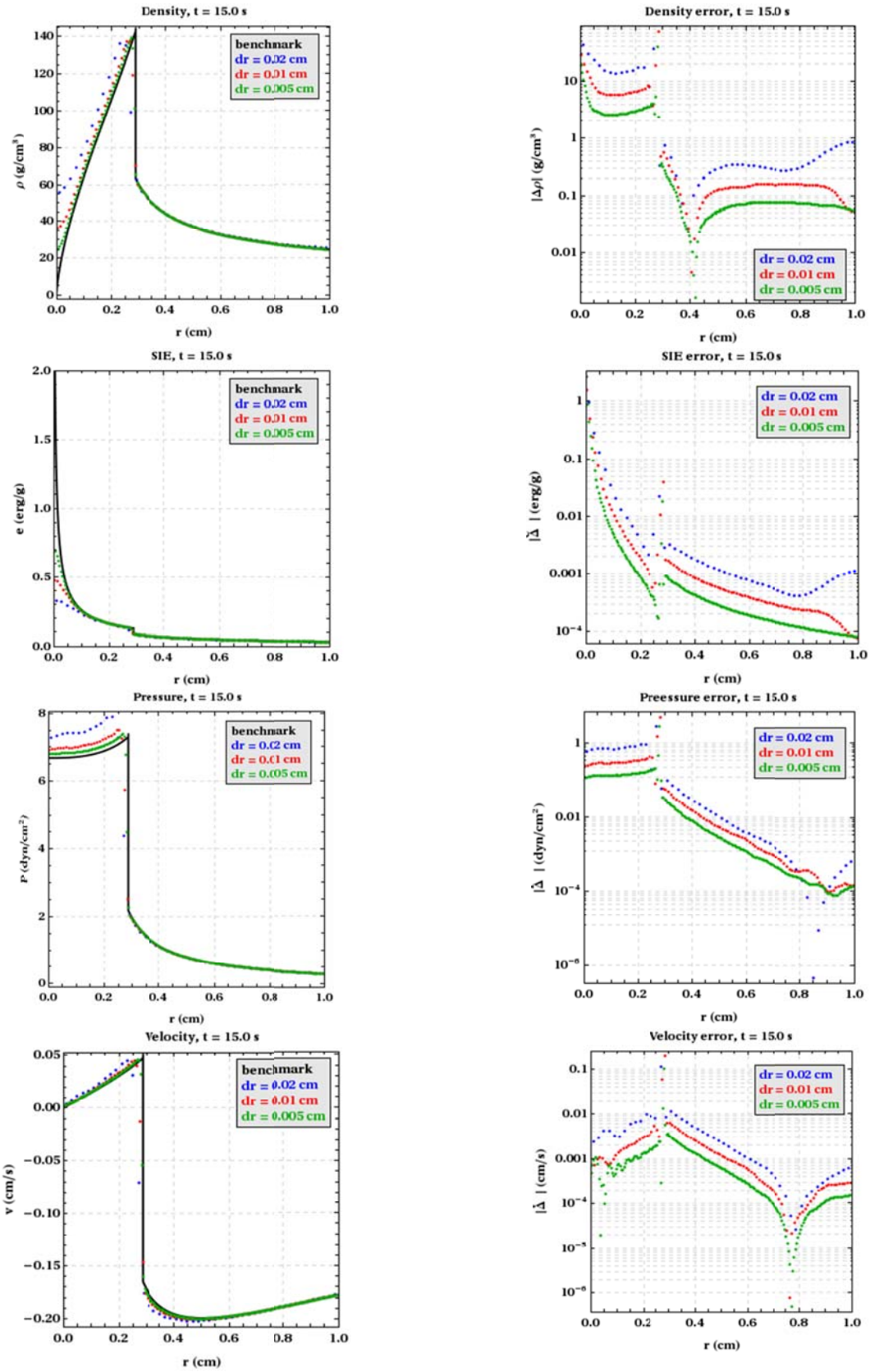

Figure 3b: 1D spherical SGP results at *t* = 15 s (diverging flow).

In Figs. 3a and 3b, the point-wise 'error' for each flow variable is calculated according to

$$\Delta f_{dr}(r,t) = |f_{\mathrm{ref}}(r,t) - f_{dr}(r,t)|\,, \tag{5}$$

where $f(r,t)$ denotes a flow variable (i.e., density, SIE, pressure, or velocity) centered at r and cell-averaged over the corresponding grid element, the 'ref' subscript denotes the reference solution, and the 'dr' subscript denotes the a solution calculated using the grid spacing dr.

Figures 3a and 3b show that all SGP flow variables appear to converge in a global sense to the reference solution as the grid spacing is refined; the quantitative behavior of this convergence will be assessed in Sec. III.C. Furthermore, localized quantities (e.g., shock location, behavior as $r \rightarrow 0$ for diverging flow) also appear to converge to the reference solution.

III.B. Adaptive Mesh Refinement

To enable the xRAGE AMR capability, additional settings beyond those prescribed at the beginning of Sec. III must be employed. In all 1D spherical simulations, the following code options pertaining to AMR were used, but are not necessary unique:

- A maximum of 10 refinement levels are allowed
- `pctdiv` = 0.001: this setting specifies the percentage change in a zone's maximum pressure required to subdivide that zone. If the estimated increase in pressure of a zone is greater than `pctdiv` multiplied by the maximum pressure that has occurred in that zone during the simulation, the zone is marked for refinement.

As was the case in Sec. III.A., the results of three simulations performed using the above settings (and the coarse/medium/fine initial grid spacings) are shown in Figs. 4a and 4b for the same times used in Figs. 3a and 3b; additional results are provided in Appendix A.

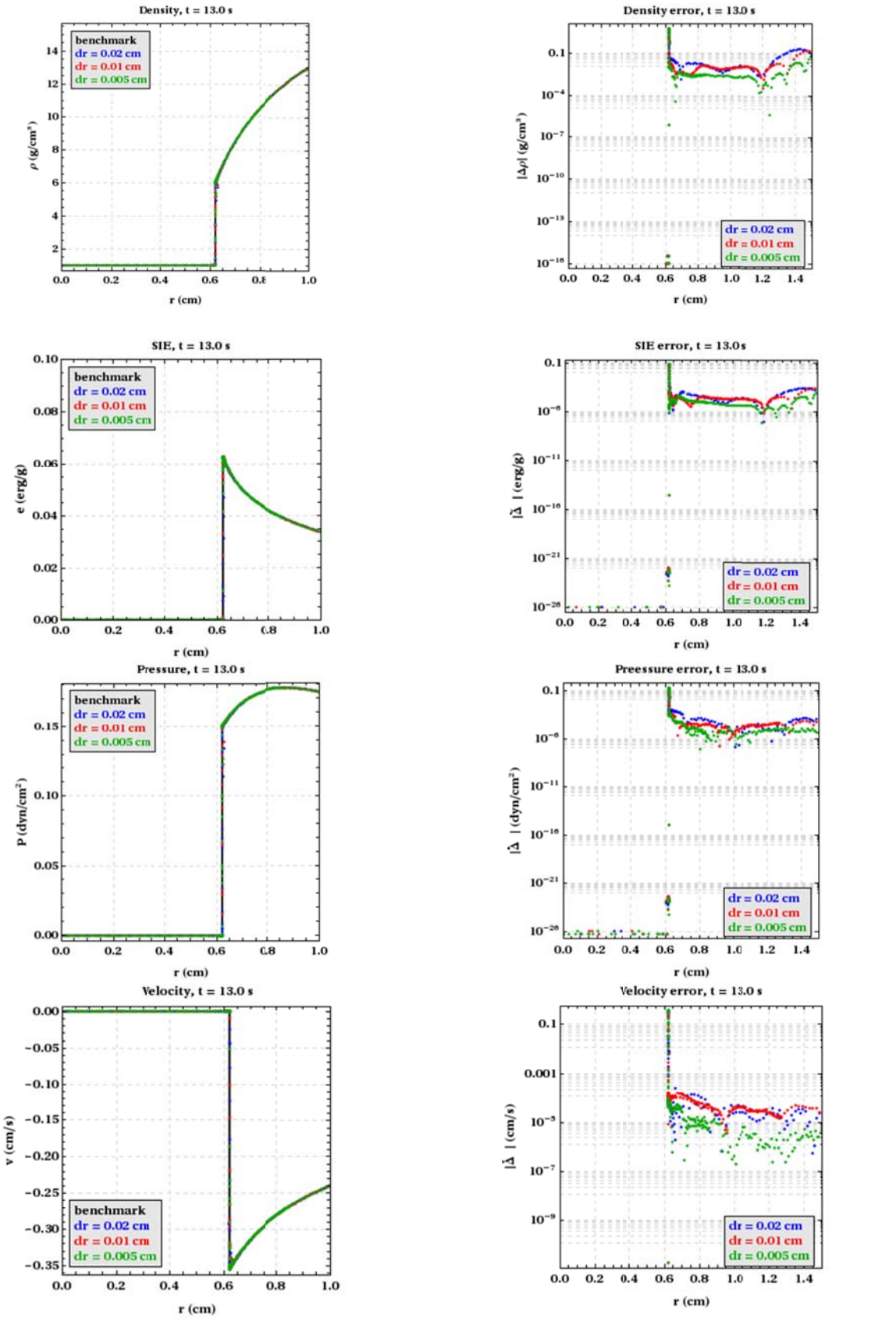

Figure 4a: 1D spherical SGP results at *t* = 13 s (converging flow) with AMR enabled.

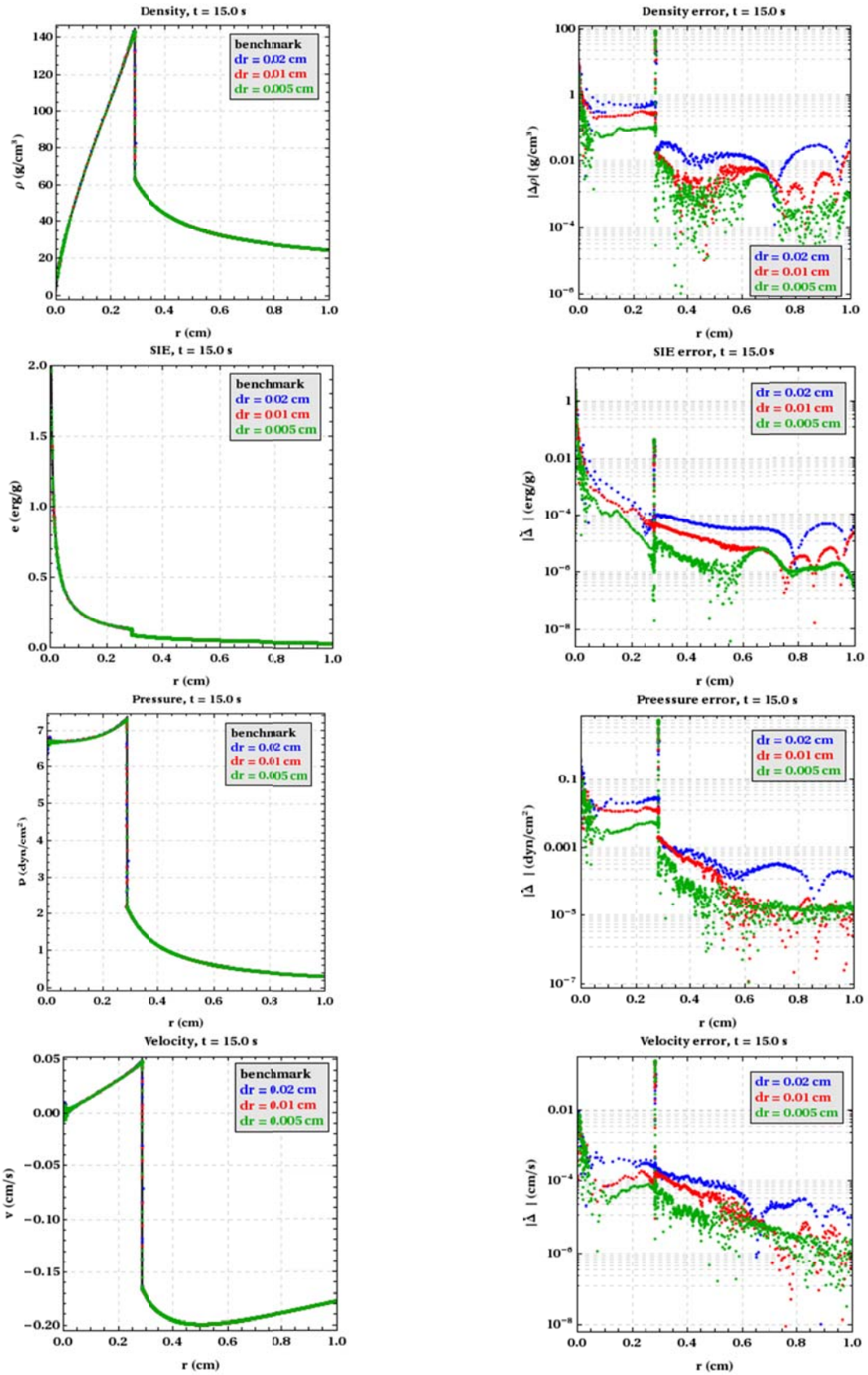

Figure 4b: 1D spherical SGP results at *t* = 15 s (diverging flow) with AMR enabled.

In Figs. 4a and 4b, Eq. (5) is again used to calculate the error for each flow variable; no interpolation of the reference solution is required since it is defined on a grid corresponding to the finest resolution used in 1D spherical AMR simulations.

Figures 4a and 4b show that all SGP flow variables appear to converge in a global sense to the reference solution as the grid spacing is refined, albeit not as cleanly as in the previous case; the quantitative behavior of this convergence will be assessed in Sec. III.C. Furthermore, localized quantities (e.g., shock location, behavior as $r \rightarrow 0$ for diverging flow) also appear to converge in some sense to the reference solution.

Despite evidence of global and local convergence trends, a prominent error is evident in the $t = 15$ flow fields as $r \rightarrow 0$. This error is most prominent in the velocity field, and is perhaps best characterized as an 'oscillation.' This phenomenon does not manifest itself in simulations without AMR, and additional evidence (see Appendices A and B) suggests that it grows as time evolves in the diverging flow regime.

Additional information pertaining to this phenomenon is presented in Appendix B, where it is revealed that the error may be created and influenced by many mechanisms, including (but not limited to) improper energy mapping into subdivided AMR zones, internal code physical unit inconsistencies, and numerical round-off[13]. Regardless of the source, this error warrants additional, dedicated investigation in a future study.

In addition to flow variable information, plots of the AMR level vs. position for two different times are provided in Fig. 5. These results (and additional results appearing in Appendix A) show that a region of mesh refinement surrounds both the converging and diverging shock waves, and that the computational grid begins to de-refine near the origin, behind the reflected shock wave.

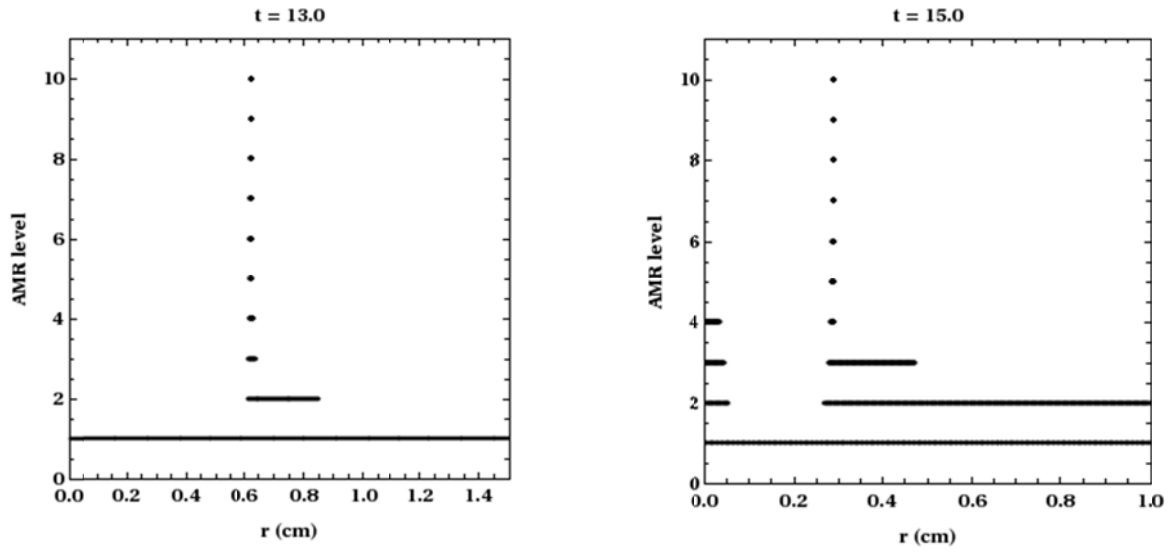

Figure 5: 1D spherical SGP AMR level results at t = 13 s (converging flow) and 15 s (diverging flow).

III.C. Simulation Comparison Metrics

Several quantities are available for the quantitative assessment of SGP calculations with respect to the benchmark solution. One such metric is the time-behavior of the global L_1 error norm for each flow variable f, given approximately by

$$L_1(f_{dr}) \approx \frac{\sum_i |f_{\mathrm{ref}}(r_i,t) - f_{dr}(r_i,t)|}{\sum_i i}\,, \tag{6}$$

and calculated for simulations performed with and without AMR enabled. In Eq. (6), the i-indices correspond to cell-averaged quantities over individual computational zones centered at a sequence of r_i values (i.e., $f_{dr}(r_i,t)$ is the average value of f_{dr} over the zone with width dr, centered at r_i). The summations therefore approximate $L_1(f_{dr})$ as the unweighted average of the zone-by-zone L_1 error within the analysis domain, with respect to the benchmark solution. Various evaluations of Eq. (6) are provided in Table II.

With approximate L_1 error norm data available, it is straightforward to construct an estimate of the L_1 norm spatial convergence rate with respect to the benchmark solution, for each time and simulation archetype (i.e., with and without AMR enabled). Using the standard error ansatz,

$$\ln[L_1(f)] = A + B\,\ln(dr)\,, \tag{7}$$

the convergence premultiplier $\exp(A)$ and convergence rate B can be calculated for each variable, time, and simulation archetype by fitting Eq. (7) to the data appearing in Table II. Example calculations of this type are shown in Fig. 6, and various convergence rates are provided in Table III.

time	**Without AMR**				**With AMR**			
	Density	SIE	Pressure	Velocity	Density	SIE	Pressure	Velocity
Initial dr = 0.02 cm								
t = 12	**1.4e-1**	**4.3e-4**	**1.6e-3**	**2.5e-3**	3.8e-1	2.4e-3	7.8e-3	1.8e-2
t = 13	**2.4e-1**	**7.5e-4**	**3.0e-3**	**3.8e-3**	5.0e-1	5.3e-3	1.5e-2	3.1e-2
t = 14	1.4e0	**1.9e-2**	1.1e-1	**5.3e-2**	**5.9e-1**	2.6e-2	**8.2e-2**	6.2e-2
t = 15	5.9e0	**3.2e-2**	2.5e-1	**5.0e-3**	**3.7e0**	5.6e-2	**2.3e-1**	9.1e-3
t = 16	5.0e0	3.2e-2	**1.2e-1**	**3.2e-3**	**3.3e0**	**1.8e-2**	1.4e-1	7.6e-3
t = 17	4.9e0	3.3e-2	**8.5e-2**	**3.2e-3**	**3.5e0**	**2.0e-2**	1.1e-1	7.1e-3
Initial dr = 0.01 cm								
t = 12	**5.3e-2**	**1.6e-4**	**6.1e-4**	**1.0e-3**	3.1e-1	2.0e-3	6.5e-3	1.5e-2
t = 13	**1.0e-1**	**3.7e-4**	**1.5e-3**	**2.0e-3**	4.0e-1	4.3e-3	1.2e-2	2.5e-2
t = 14	8.1e-2	**9.0e-3**	6.4e-2	**2.9e-2**	**4.0e-1**	2.0e-2	**6.0e-2**	5.0e-2
t = 15	3.3e0	**2.8e-2**	**1.5e-1**	**4.0e-3**	**2.8e0**	4.1e-2	1.8e-1	7.0e-3
t = 16	**2.3e0**	2.8e-2	**5.7e-2**	**1.5e-3**	2.5e0	**2.3e-2**	1.0e-1	5.6e-3
t = 17	**2.0e0**	**2.8e-2**	**3.2e-2**	**1.2e-3**	2.9e0	2.9e-2	9.5e-2	6.2e-3
Initial dr = 0.005 cm								
t = 12	**2.8e-2**	**1.0e-4**	**3.2e-4**	**6.1e-4**	2.0e-1	1.4e-3	4.1e-3	1.0e-2
t = 13	**4.8e-2**	**2.0e-4**	**8.3e-4**	**1.2e-3**	3.0e-1	3.2e-3	9.2e-3	1.9e-2
t = 14	4.4e-1	**5.0e-3**	**3.6e-2**	**1.7e-2**	**2.3e-1**	1.2e-2	3.7e-2	3.0e-2
t = 15	**1.3e0**	**2.4e-2**	**5.9e-2**	**1.0e-3**	1.6e0	4.6e-2	1.0e-1	4.3e-3
t = 16	**1.1e0**	**2.4e-2**	**2.8e-2**	**7.2e-4**	1.6e0	3.2e-2	6.7e-2	3.8e-3
t = 17	**1.0e0**	**2.4e-2**	**1.9e-2**	**7.5e-4**	1.6e0	7.5e-2	4.9e-2	3.3e-3

Table II: Global L_1 error norms for various 1D spherical SGP calculations. A bold number indicates a smaller L_1 error norm estimate in comparison to the counterpart value.

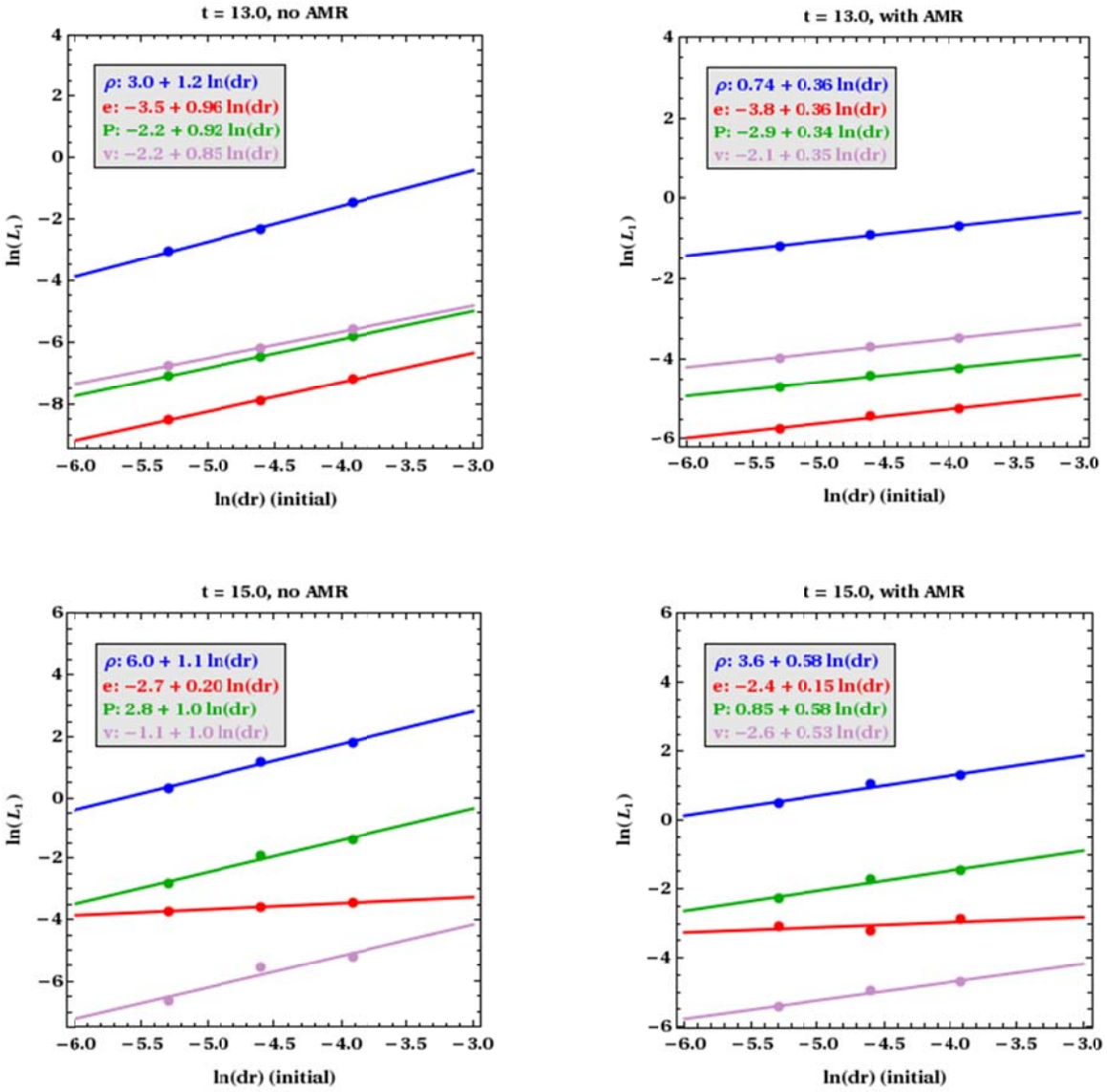

Figure 6: L_1 norm spatial convergence curves for 1D spherical SGP, at t = 13 s (converging flow) and 15 s (diverging flow).

time	Without AMR				With AMR			
	Density	SIE	Pressure	Velocity	Density	SIE	Pressure	Velocity
$t = 12$	1.15	1.03	1.13	1.01	0.47	0.39	0.46	0.41
$t = 13$	1.15	0.96	0.92	0.85	0.36	0.36	0.34	0.35
$t = 14$	0.87	0.90	0.80	0.82	0.68	0.53	0.58	0.51
$t = 15$	1.07	0.20	1.04	1.03	0.58	0.15	0.58	0.53
$t = 16$	1.12	0.21	1.08	1.08	0.52	-0.43	0.55	0.50
$t = 17$	1.12	0.22	1.07	1.04	0.56	-0.95	0.59	0.56

Table III: L_1 norm spatial convergence rates for 1D spherical SGP calculations.

Tables II and III and Fig. 6 show that for simulations without AMR options enabled, the spatial L_1 error norm converges at or near first order for all variables in the converging flow regime. A small convergence rate degradation is evident at $t = 14$ s; this phenomenon is due to the close proximity of the converging shock to the origin at that time (and associated rapid growth of the various flow variables). The near-linear convergence rate trend is restored after shock reflection for all variables except the SIE, which exhibits a markedly sub-linear convergence rate in the diverging flow regime. Figure 3b reveals no immediately obvious explanation for this behavior, but it is possible that a wall-heating effect or default code option (see Appendix B) is contributing to the degraded convergence rate.

For calculations with AMR options (as outlined at the beginning of Sec. III.B) enabled, Tables II and III and Fig. 6 show universally degraded convergence rates in comparison with the uniform-grid simulations. Otherwise, the AMR simulation convergence rates follow similar trends as previously discussed; however, in this case, negative convergence rates are observed in the SIE field in the divergent flow regime. It is possible that the choice of AMR parameters may exacerbate the trends already observed for the uniform-grid simulations.

Furthermore, Table II shows that in most cases (but not all), enabling AMR options degrades the spatial L_1 norm that would otherwise be obtained in the absence of those options. In addition to the convergence rate data, this phenomenon suggests that a different set of AMR options should be investigated, or, since the initial grid spacing is evidently refined enough for convergence to be observed, a coarser set of initial spacings should be employed when AMR settings are to be activated.

IV. THE SURROGATE GUDERLEY PROBLEM IN 2D AXI-SYMMETRY

Constructing a 2D axi-symmetric SGP setup in xRAGE (v1109.02) is only slightly more complicated than the 1D spherical case (see Appendix E). In all 2D simulations, the following code options were used but are not necessarily unique:

- Code default units (cgs)
- Specific heat $c_v = 1.0$ erg/(g-eV), so temperature and SIE are equivalent
- Adaptive time step
- Stop time = 20.0 s

- Boundary condition at $r = 0$ cm: code default (symmetric/reflective BC)
- Boundary condition at $r = 10$ cm: code default (reflective BC[13])
- Boundary condition at $z = 0$ cm: code default (rigid wall BC)
- Boundary condition at $z = 10$ cm: code default (reflective BC)
- Initial uniform grid spacing (for calculation verification analysis):
    - $dr = dz = 0.04$ cm (coarse)
    - $dr = dz = 0.02$ cm (medium)
    - $dr = dz = 0.01$ cm (fine)

The initialization provided above does not guarantee that the contact surface between the dense and rarefied gases coincides with zone boundaries; in general this will not be the case for a circular contact surface on a square grid. In many instances the contact surface may pass through initial computational zone boundaries and vertices, or within corresponding zones themselves.

In xRAGE, 'mixed zone' initialization is addressed through the use of the `numfine` parameter. For example, if a computational zone contains a contact surface separating two sub-zone regions with uniform densities ρ_1 and ρ_2, allocated according to initially unknown volume fractions f_1 and f_2 (see Fig. 7), then the zone-averaged density is given by

$$\bar{\rho}_z = \rho_1 f_1 + \rho_2 f_2 \,. \tag{8}$$

Various settings of the `numfine` parameter control how the volume fractions are determined, and thus how Eq. (8) is approximated. If `numfine` = 1, the density ρ_s is sampled at a single location within a zone (the center). If $\rho_s = \rho_1$, then $f_1 = 1$ and $f_2 = 0$. If $\rho_s = \rho_2$, then $f_1 = 0$ and $f_2 = 1$. Choices of `numfine` > 1 correspond to increasingly rigorous sampling of mixed zones, increasingly accurate estimates of f_1 and f_2, and the generation of less 'jagged' initial data (see Appendix B).

IV.A. Uniform Grid

The results of one simulation performed using the above settings and $dr = dz = 0.01$ cm are shown as contour plots in Figs. 8a (an example of convergent flow) and 8b (an example of divergent flow) and 'line-out plots' in conjunction with the 1D spherical benchmark solution in Figs. 8c and 8d; additional results are provided in Appendix A.

The line-out plots (of which the error plots appearing in Figs. 9a and 9b, and Figs. 8c and 8d are also examples) are constructed using Eq. (2): every flow data value parameterized by an (r,z) zone center or vertex can be equivalently parameterized according to the corresponding 'spherical radius' R. Furthermore, angle-parameterized data can be constructed for each (r,z) zone center or vertex with the transformation

$$\theta = \arctan\left(\frac{z}{r}\right), \tag{9}$$

so that, for example, the $\theta = 45$-degree line corresponds to the collection of zones with $r = z$ center or vertex coordinates. Additional θ-lines can also be defined: the $\theta = 0$-degree line

corresponds to the collection of zones along the *r*-axis, while the $\theta = 90$-degree line corresponds to the collection of zones along the *z*-axis (see Figs. 8c and 8d). This nomenclature will be used in numerous figures throughout the remainder of this report.

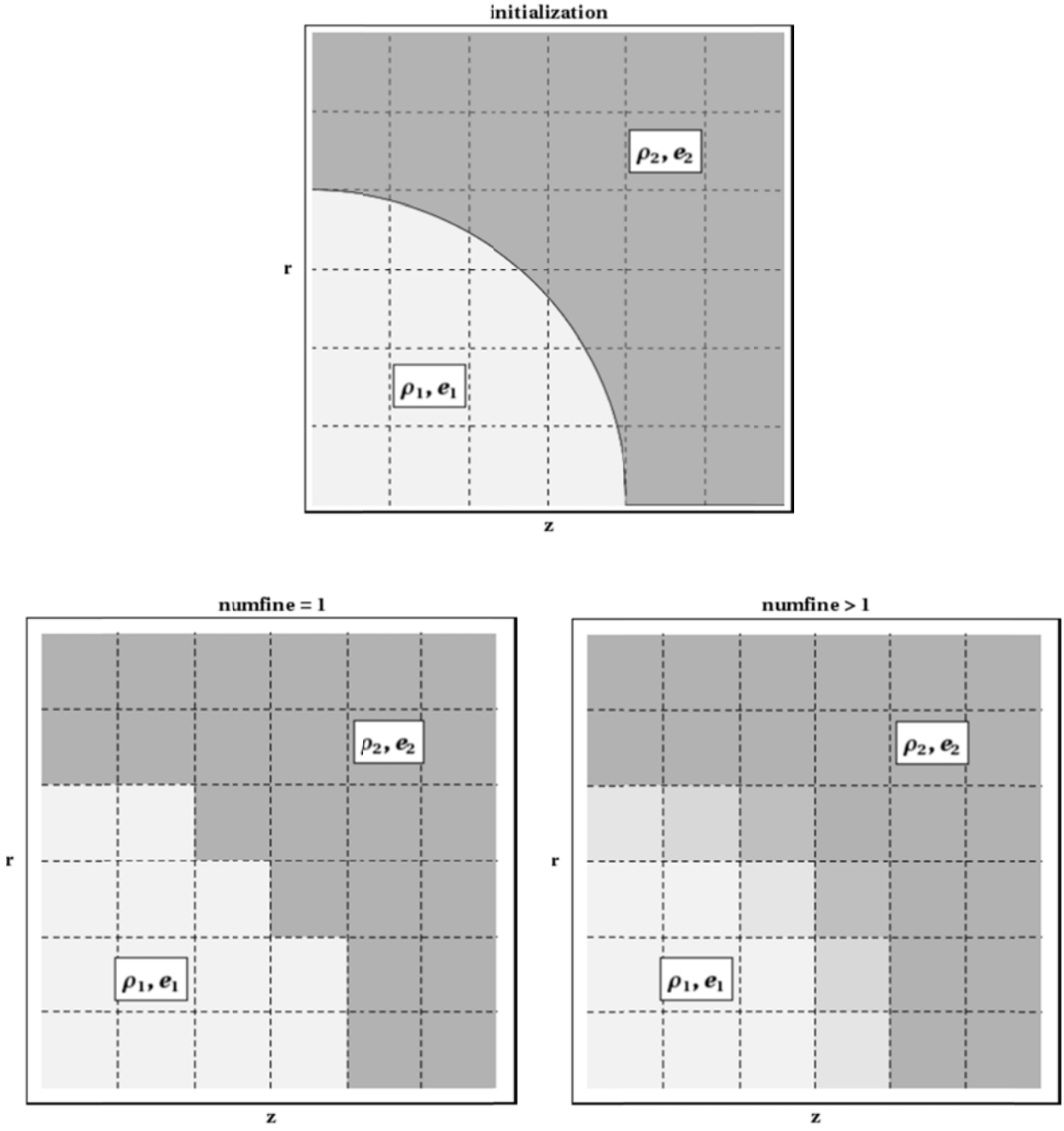

Figure 7: Notional SGP initialization on a square axi-symmetric grid, and effect of archetypal `numfine` parameter settings. Note that for `numfine` > 1, the initial data is 'smeared out' over a number of zones.

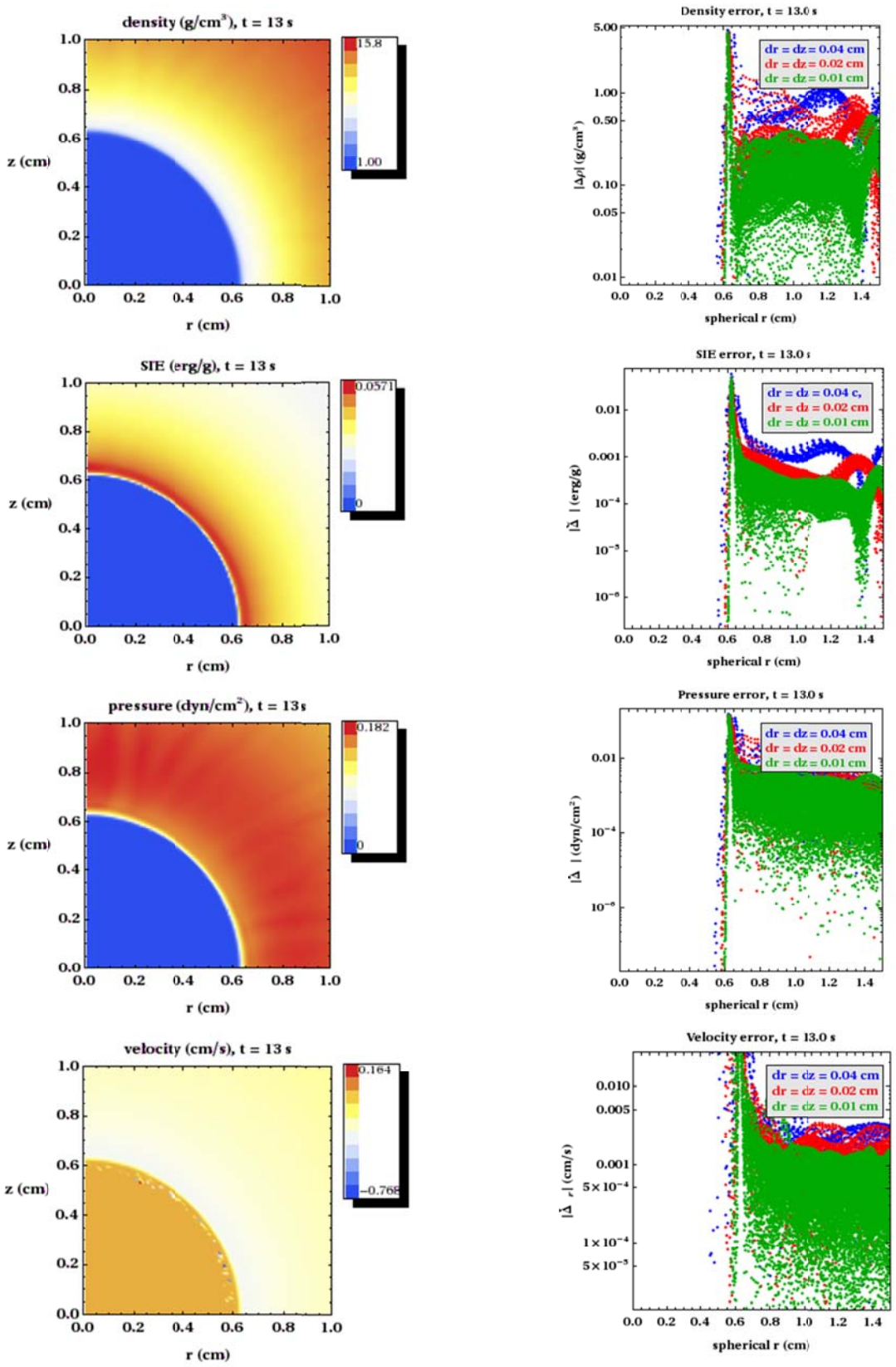

Figure 8a: Left – 2D axi-symmetric SGP results for *dr* = *dz* = 0.01 cm at *t* = 13 s (converging flow). Right – solution error on three different grids, calculated using Eq. (5).

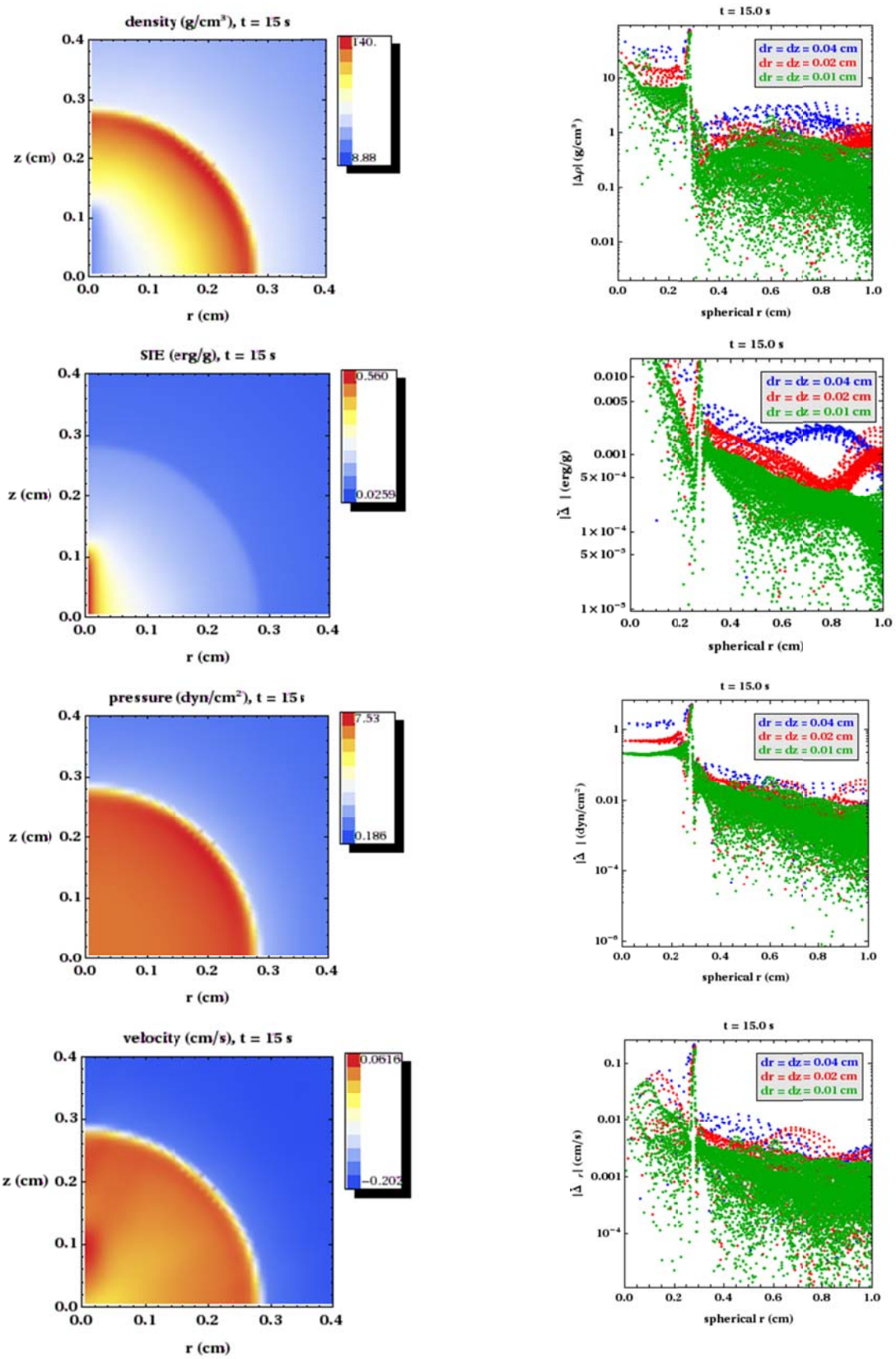

Figure 8b: Left – 2D axi-symmetric SGP results for *dr* = *dz* = 0.01 cm at *t* = 15 s (diverging flow). Right – solution error on three different grids, calculated using Eq. (5).

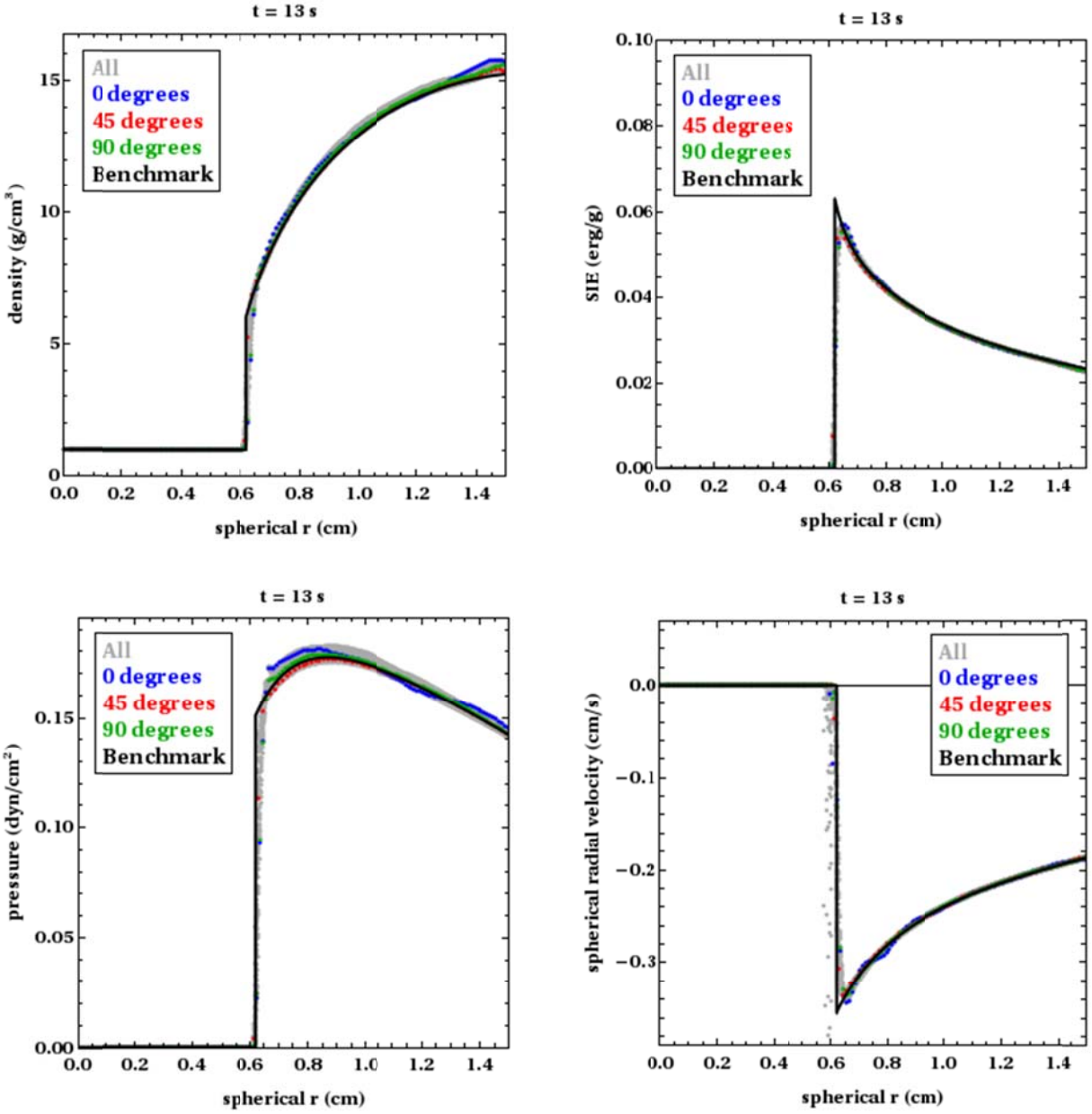

Figure 8c: 2D axi-symmetric SGP line-out results for *dr* = *dz* = 0.01 cm at *t* = 13 s (converging flow).

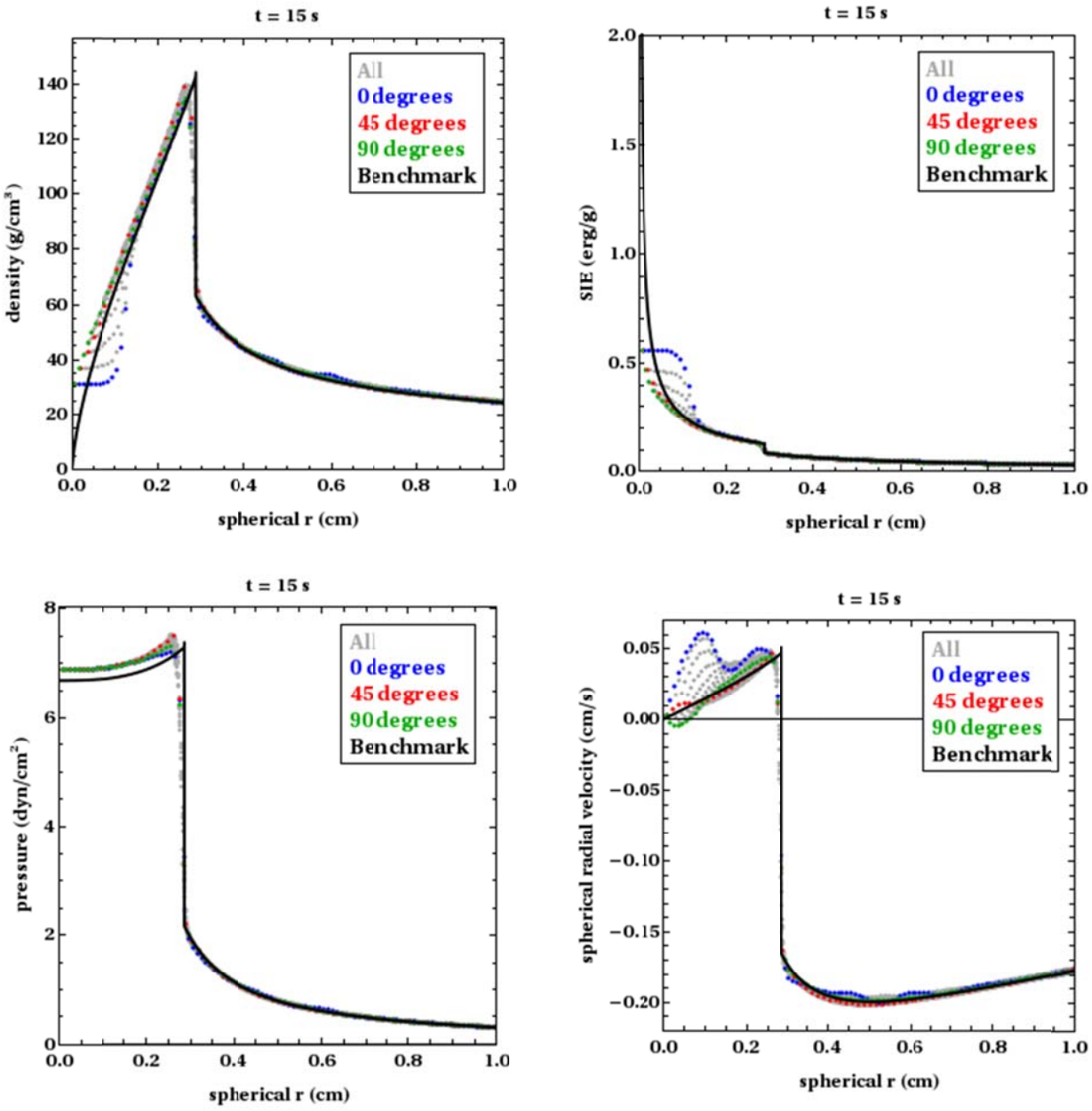

Figure 8d: 2D axi-symmetric (fine grid) SGP line-out results for *dr* = *dz* = 0.01 cm at *t* = 15 s (diverging flow).

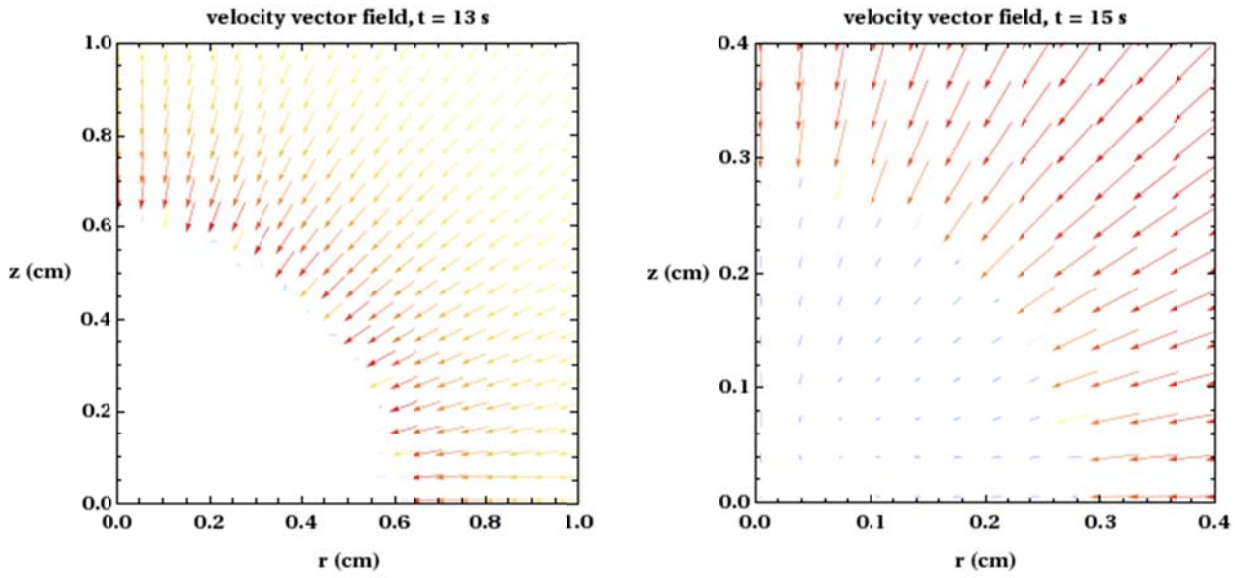

Figure 8e: 2D axi-symmetric (fine grid) SGP velocity vector results for *dr* = *dz* = 0.01 cm at *t* = 13 s (left, converging flow) and 15 s (right, diverging flow).

Figures 8a, 8c, and the first member of Fig. 8e show that SGP solution stays maintains a high degree of symmetry during the convergent flow phase, with some small on-axis perturbations evident. Figures 8b, 8d, and the second member of Fig. 8e show that more marked flow asymmetries develop in the diverging flow regime, particularly in the density, SIE, and velocity fields along the boundaries. Most notably, an asymmetric wall-heating effect localized along the *z*-axis is seen to develop while the flow is diverging, but beyond the reflected shock the flow fields appear to maintain their pre-focus symmetry.

There is evidence that the asymmetric wall heating effect is not unique to xRAGE, and it has reportedly been observed in other compressible flow solvers[14]. The canonical explanation for this effect is given in terms of the difference between the *r* and *z* coordinates in 2D axi-symmetry: *z* is a linear coordinate, while *r* is a curvilinear coordinate. Thus, even though the 2D axi-symmetric grid may appear to be square, there are fundamental geometric differences between grid structures in the two ordinate directions. This difference leads to a more prominent wall heating error in the 'more curvilinear' direction (as opposed to the strictly linear direction), as often observed in Noh problem simulations[15], and discussed further in Appendix D.

IV.B. Adaptive Mesh Refinement

To enable the xRAGE AMR capability, additional settings beyond those prescribed at the beginning of Sec. IV must again be employed. In all 2D axi-symmetric simulations, the following code options pertaining to AMR were used, but are not necessary unique:

- A maximum of 5 refinement levels are allowed
- `pctdiv` = 0.001

Although it was not observed in the 1D spherical simulations (because at initialization, the interface corresponded to a computational zone boundary), the xRAGE AMR algorithms allow for mesh refinement at initialization, before any hydrodynamic computations occur. This functionality is separate from the `numfine` interface reconstruction capability discussed in Sec. IV.A, and at initialization allows for an ostensibly more accurate depiction of a circular interface imprinted upon a square grid. For the problem under consideration, an example of such an initial refinement appears in Fig. 9.

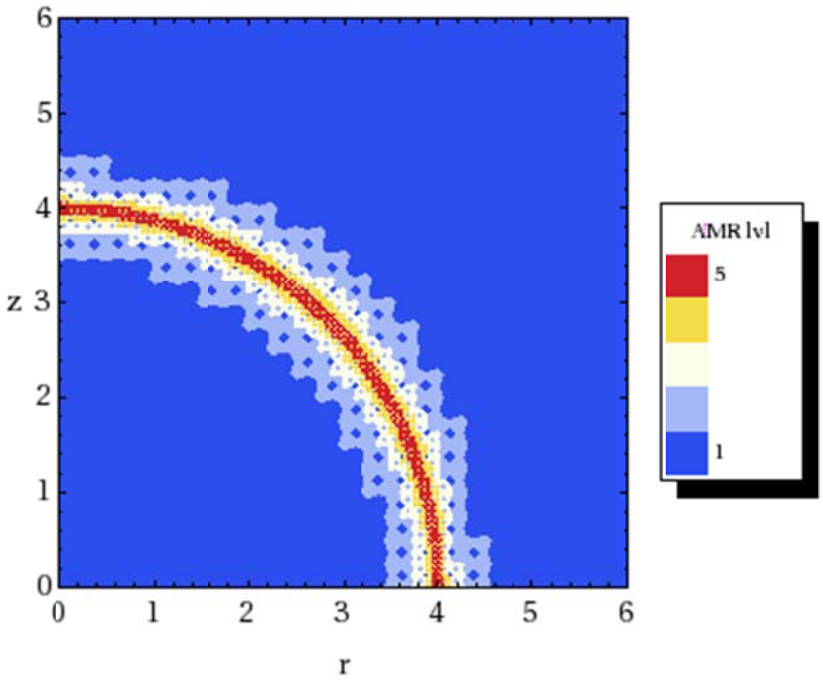

Figure 9: Initial AMR refinement of SGP initialization on a *dr* = *dz* = 0.01 cm 2D axi-symmetric grid.

Figure 9 shows that at initialization, the highest level of refinement exists around the contact surface, while lower levels are spread around the finest-level structure. A semi-regular pattern appears to be contained within the initial grid; this effect will likely be influenced by the choice of AMR parameters and its impact on the remainder of the simulation has yet to be assessed.

As was the case in Sec. IV.A., the results of an initial $dr = dz = 0.01$ cm simulation performed using the above settings are shown in Figs. 10a-d for the same times used in Figs. 10a-d; additional results appear in Appendix A.

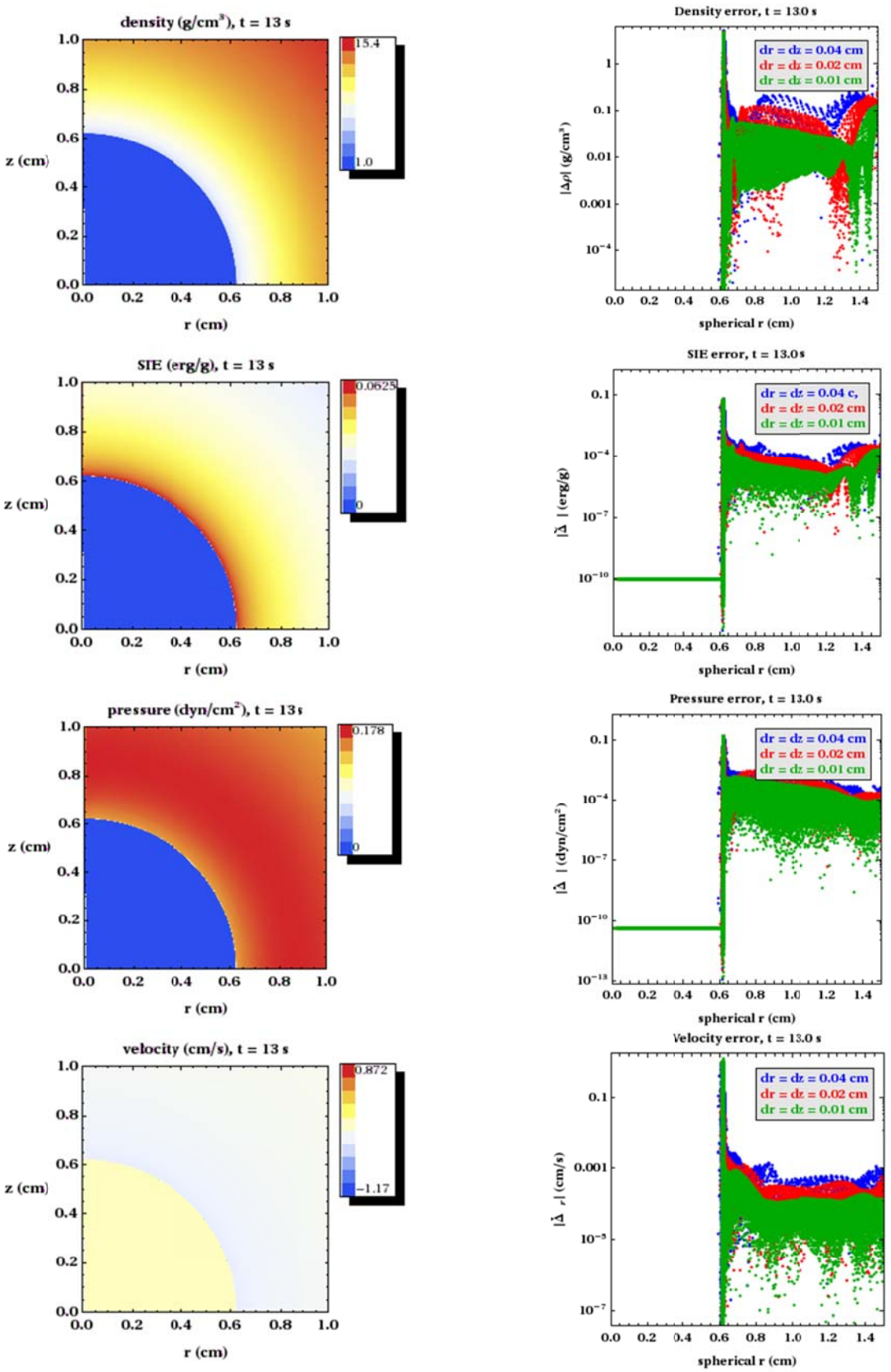

Figure 10a: Left – 2D axi-symmetric SGP results for initial *dr* = *dz* = 0.01 cm at *t* = 13 s (converging flow) with AMR enabled. Right – solution error on three different grids, calculated using Eq. (5).

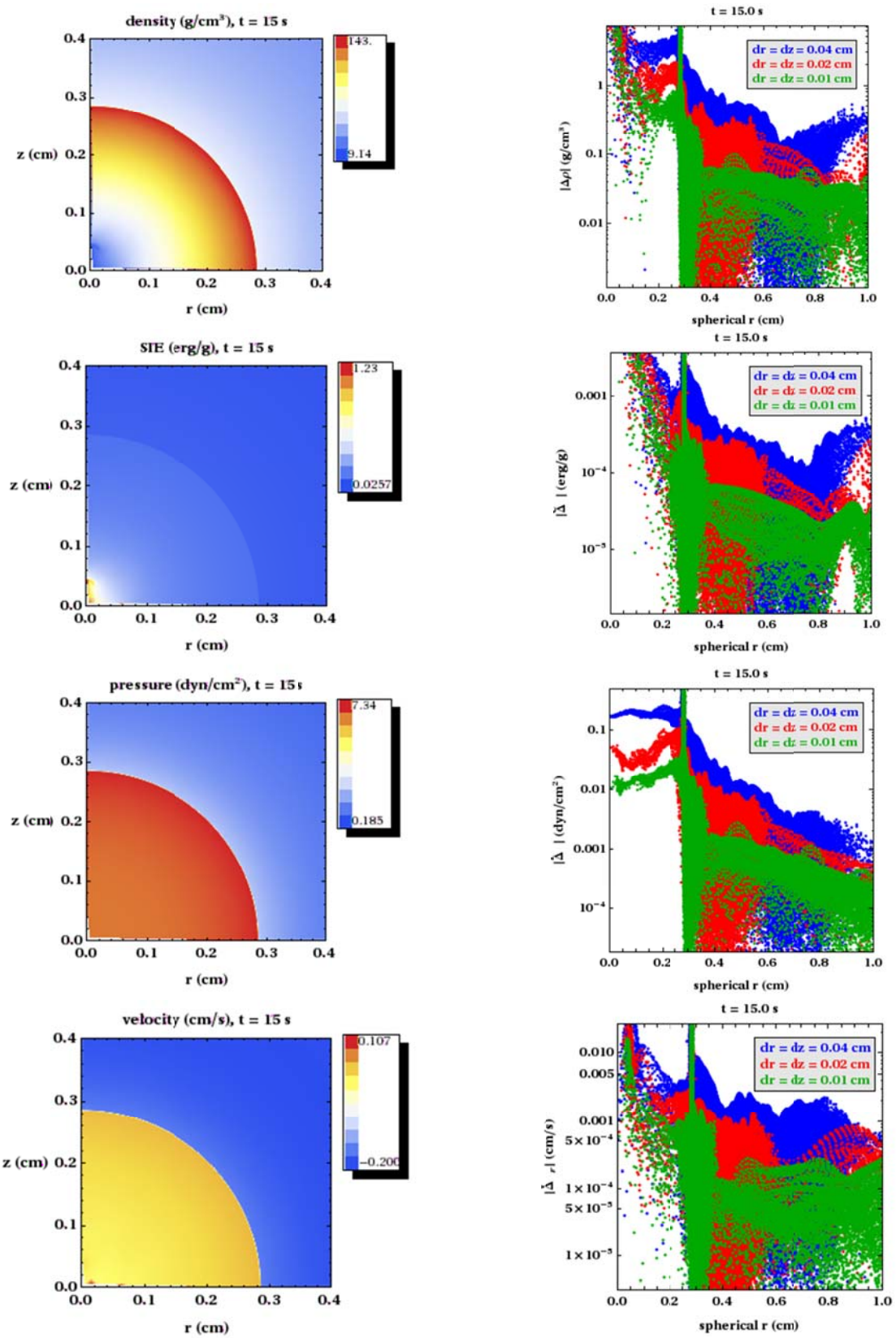

Figure 10b: Left – 2D axi-symmetric SGP results for initial *dr* = *dz* = 0.01 cm at *t* = 15 s (diverging flow) with AMR enabled. Right – solution error on three different grids, calculated using Eq. (5).

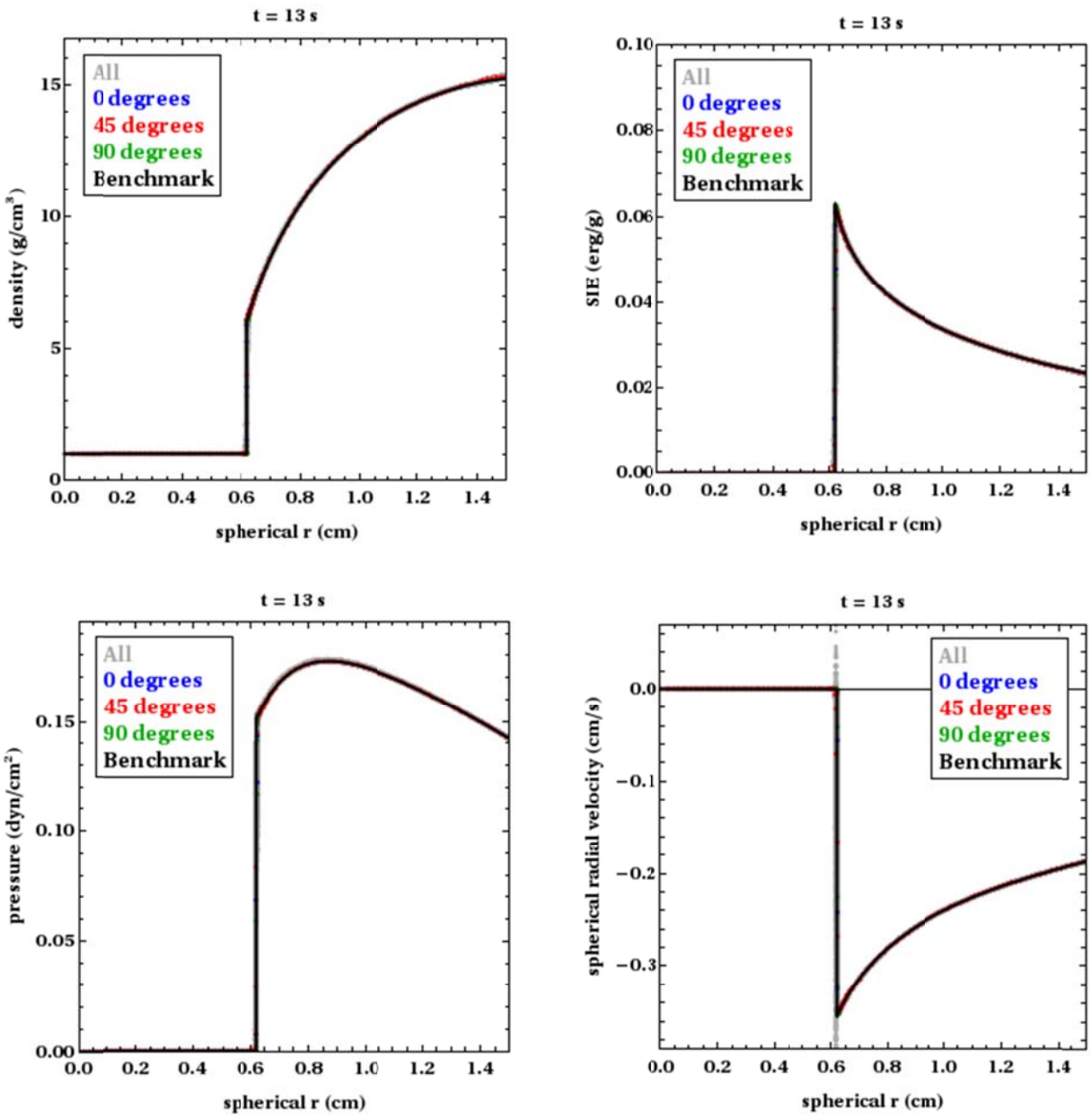

Figure 10c: 2D axi-symmetric SGP line-out results for initial *dr* = *dz* = 0.01 cm at *t* = 13 s (converging flow) with AMR enabled.

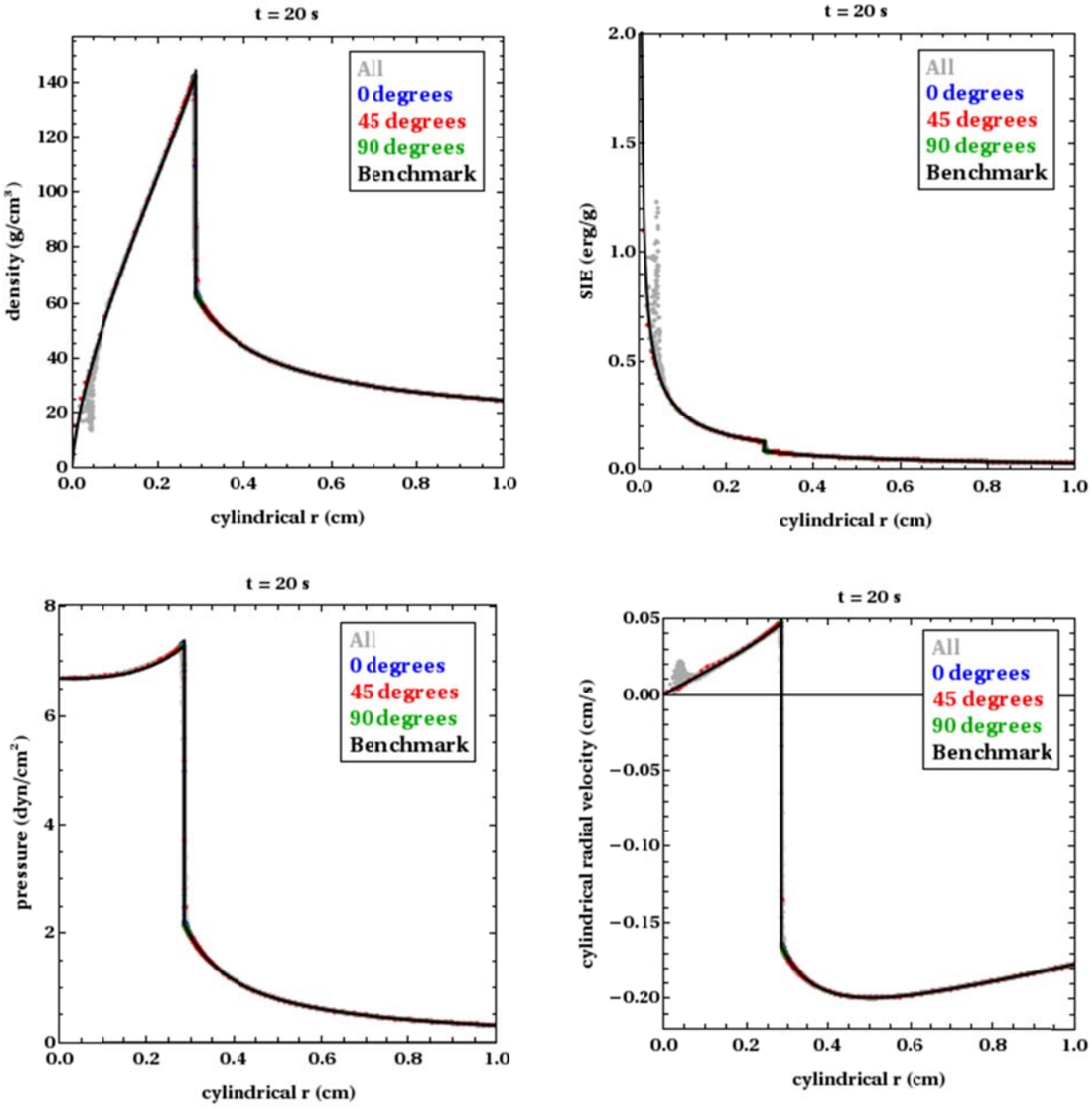

Figure 10d: 2D axi-symmetric SGP line-out results for initial *dr* = *dz* = 0.01 cm at *t* = 15 s (diverging flow) with AMR enabled.

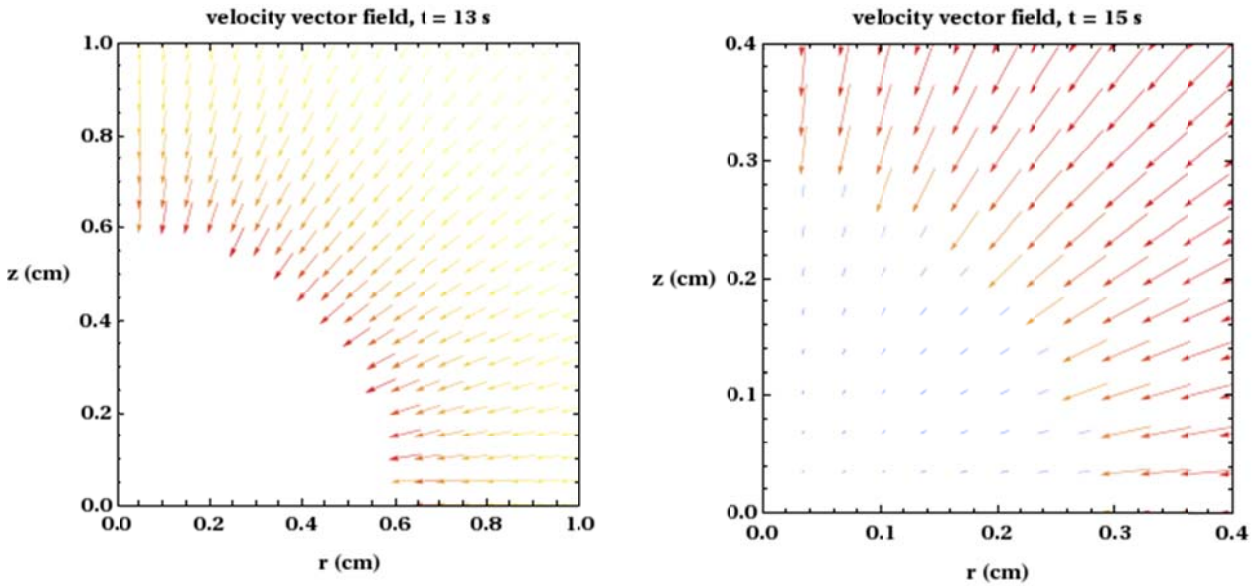

Figure 10e: 2D axi-symmetric SGP velocity vector results for initial *dr* = *dz* = 0.01 cm at *t* = 13 s (left, converging flow) and 15 s (right, diverging flow) with AMR enabled.

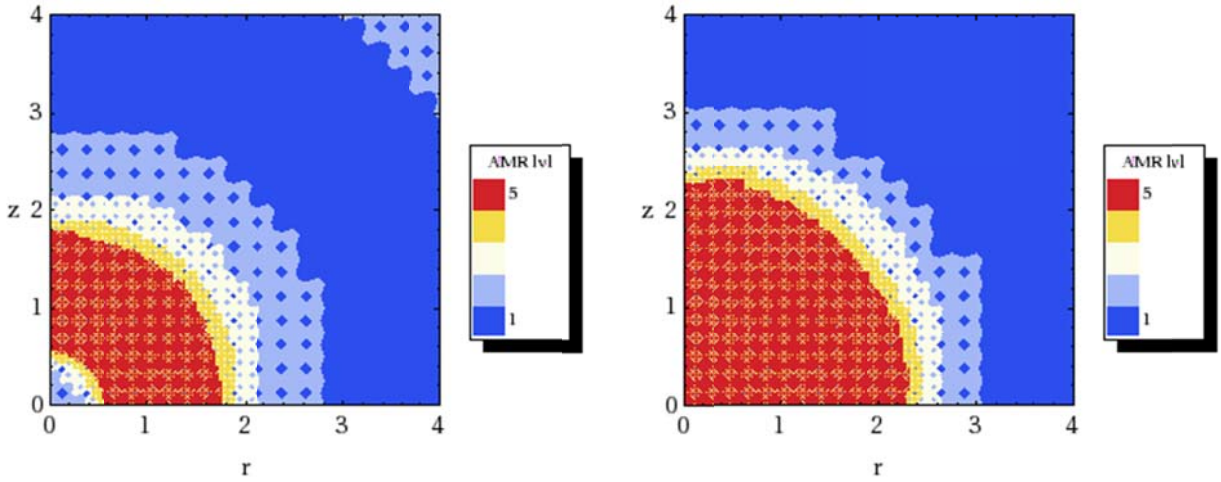

Figure 10f: 2D axi-symmetric SGP AMR level results for initial *dr* = *dz* = 0.01 cm at *t* = 13 s (left, converging flow) and 15 s (right, diverging flow).

Figures 8 and 10 show that the use of AMR leads to a noticeable sharpening of the shock structure in both the converging and diverging flow regimes. As was seen in the uniform-grid simulations, the AMR simulations maintain a high degree of symmetry during the converging flow phase, though some near-origin asymmetry is still evident (but reduced) in the diverging regime. It appears from Fig. 10b that the wall heating error is significantly reduced through the use of AMR, although it is still present and still asymmetric. Aside from these general trends, a noticeable feature appearing in Fig. 12c is a compact SIE/velocity 'spike' (and corresponding density 'anti-spike') located near $r = 0.05$ cm at $t = 15$ s. This flow feature does not appear to be tied to either of the problem boundaries, and is likely a manifestation of the oscillation phenomenon discussed in Sec. III.B (and Appendix B).

Furthermore, Fig. 10f provides an example of how the AMR grid refines and relaxes as the simulation proceeds. Starting at initialization (see Fig. 9), the converging shock is enveloped by a refinement 'ring' that is preceded and followed by additional layers of lower refinement. In the divergent flow regime, the AMR grid shows extensive, persistent, maximum-level refinement that begins to relax near the origin only for very late times; this phenomenon is likely due to the presence of a steep density gradient behind the reflected shock.

Figure 10f also shows the presence of a semi-regular pattern much like that observed in Fig. 9; the effect of this pattern (and the AMR settings that produced it) will be examined further in a future study, as additional supporting calculations with different AMR settings will be needed to fully assess the effect.

IV.C. Simulation Comparison Metrics

The quantitative analysis metrics used in Sec. III.C for 1D spherical simulations are also applicable for 2D axi-symmetric simulations. In L_1 error norm calculations, however, 2D axi-symmetric data must be compared to 1D spherical benchmark data. Thus, every (r,z) zone center or vertex to which 2D cell-averaged data is referenced must be 'collapsed' to a 1D spherical radial position R using Eq. (2). The result of this operation is a set of 1D spherical data with ordinates not necessarily identical to or otherwise explicitly contained within the set of reference solution ordinates. Therefore, an interpolation strategy must be used in the evaluation of Eqs. (5) and (6).

In this study, the Mathematica[16] `interpolation` function (instantiated as 3rd order polynomial interpolation between collections of successive data points) is used to construct quasi-continuous data from the 1D spherical benchmark SGP solution; the resulting function can then be evaluated at any R-ordinate selected by the collapsed 2D axi-symmetric solution, as can Eqs. (5) and (6). The results of this process appear in Table IV.

From the data appearing in Table IV, L_1 norm spatial convergence rates can be constructed in the same manner as done in Sec. III.C; the results of these calculations are provided in Fig. 11 and Table V.

Tables IV and V and Fig. 11 show that for simulations without AMR options enabled, the spatial L_1 error norm converges at or near first order for all variables in the converging flow regime. A small convergence rate degradation is evident at t = 14 s; this phenomenon is due to the close proximity of the converging shock to the origin at that time (and associated rapid growth of the various flow variables). The near-linear convergence rate trend is restored after shock reflection for all variables except the SIE, which exhibits a markedly sub-linear convergence rate in the diverging flow regime.

For calculations with AMR options (as outlined at the beginning of Sec. III.B) enabled, Tables IV and V and Fig. 11 show universally degraded and sometimes negative convergence rates in comparison with the uniform-grid simulations.

Furthermore, Table IV shows that in some cases (but not all), enabling AMR options degrades the spatial L_1 norm that would otherwise be obtained in the absence of those options. In addition to the convergence rate data, this phenomenon suggests that a different set of AMR options should be investigated, or, since the initial grid spacing is evidently refined enough for convergence to be observed, a coarser set of initial spacings should be employed when AMR settings are to be activated.

time	**Without AMR**				**With AMR**			
	Density	SIE	Pressure	Velocity	Density	SIE	Pressure	Velocity
Initial $dr = dz = 0.04$ cm								
$t = 12$	4.4e-1	1.4e-3	3.5e-2	**1.1e-2**	**2.2e-1**	**1.3e-3**	**4.7e-3**	1.7e-2
$t = 13$	6.0e-1	**1.7e-3**	**5.5e-3**	**1.0e-2**	**3.6e-1**	2.6e-3	1.1e-2	2.4e-2
$t = 14$	**5.8e-1**	**4.9e-3**	**4.2e-2**	**1.5e-2**	7.5e-1	6.1e-3	5.6e-2	2.0e-2
$t = 15$	3.6e0	4.3e-3	1.6e-1	6.9e-3	**5.8e-1**	**7.7e-4**	**3.1e-2**	**1.5e-3**
$t = 16$	4.5e0	5.0e-3	1.3e-1	7.0e-3	**6.7e-1**	**7.4e-4**	**2.0e-2**	**1.3e-3**
$t = 17$	7.0e0	7.0e-3	1.2e-1	8.6e-3	**1.1e0**	**1.0e-3**	**1.8e-2**	**1.8e-3**
Initial $dr = dz = 0.02$ cm								
$t = 12$	**2.1e-1**	**6.6e-4**	**1.9e-2**	**4.9e-3**	3.9e0	3.6e-2	9.6e-2	2.2e-1
$t = 13$	3.0e-1	**7.7e-4**	**3.0e-3**	**4.9e-3**	**2.5e-1**	1.9e-3	7.8e-3	1.9e-2
$t = 14$	**3.0e-1**	**4.0e-3**	**2.7e-2**	**1.1e-2**	7.3e-1	9.4e-3	6.6e-2	2.8e-2
$t = 15$	1.7e0	2.6e-3	7.8e-2	3.8e-3	**5.7e-1**	**6.8e-4**	**3.2e-2**	**1.3e-3**
$t = 16$	2.3e0	3.4e-3	6.3e-2	3.8e-3	**6.1e-1**	**4.8e-4**	**2.4e-2**	**1.2e-3**
$t = 17$	3.2e0	4.6e-3	5.4e-2	4.6e-3	**1.0e0**	**5.1e-4**	**3.2e-2**	**2.1e-3**
Initial $dr = dz = 0.01$ cm								
$t = 12$	**9.0e-2**	**3.1e-4**	1.0e-2	**2.9e-3**	1.5e-1	1.1e-3	**3.0e-3**	1.3e-2
$t = 13$	**1.3e-1**	**3.6e-4**	**1.5e-3**	**2.4e-3**	1.8e-1	1.4e-3	5.6e-3	1.5e-2
$t = 14$	**2.3e-1**	**6.9e-3**	**2.3e-2**	**1.9e-2**	6.4e-1	1.5e-2	7.3e-2	3.9e-2
$t = 15$	**8.5e-1**	1.7e-3	**4.0e-2**	**2.0e-3**	1.2e0	**1.0e-3**	7.4e-2	2.8e-3
$t = 16$	**1.1e0**	2.4e-3	**3.1e-2**	**2.1e-3**	2.1e0	**8.5e-4**	9.2e-2	4.3e-3
$t = 17$	**1.5e0**	3.1e-3	**2.5e-2**	**2.4e-3**	1.9e0	**6.9e-4**	6.2e-2	3.8e-3

Table IV: Global L_1 error norms for various 2D axi-symmetric SGP calculations. A bold number indicates a smaller L_1 error norm estimate in comparison to the counterpart value.

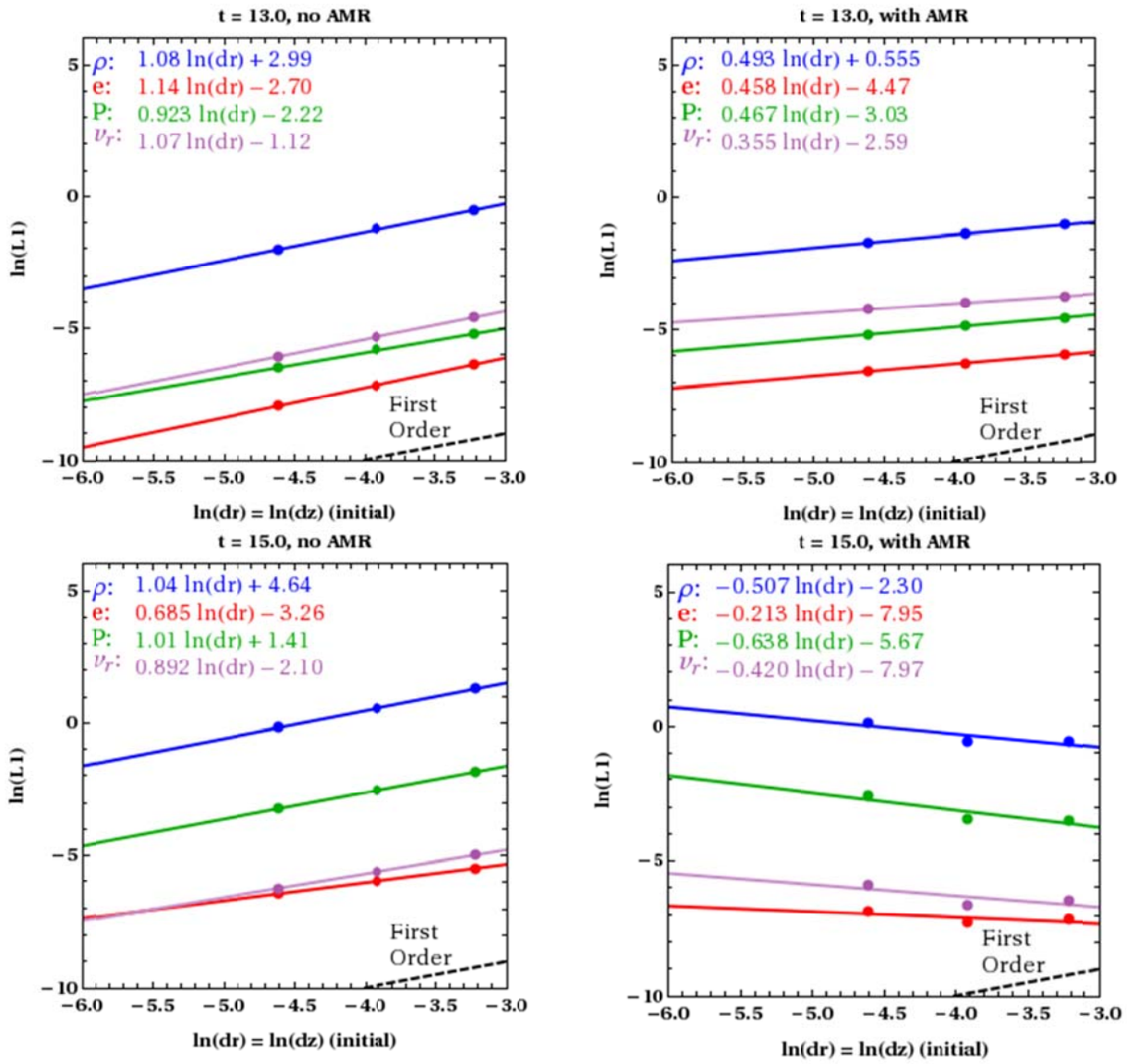

Figure 11: L_1 norm spatial convergence curves for 2D axi-symmetric SGP simulations with and without AMR, at t = 13 s (converging flow) and 15 s (diverging flow).

time	Without AMR				With AMR			
	Density	SIE	Pressure	Velocity	Density	SIE	Pressure	Velocity
t = 12	1.14	1.10	0.89	0.97	0.29	0.17	0.32	0.18
t = 13	1.08	1.14	0.92	1.07	0.49	0.46	0.47	0.36
t = 14	1.09	0.83	0.86	0.61	0.12	-0.65	-0.19	-0.48
t = 15	1.04	0.69	1.01	0.89	-0.51	-0.21	-0.64	-0.42
t = 16	1.00	0.54	1.01	0.88	-0.83	-0.10	-1.10	-0.87
t = 17	1.13	0.60	1.15	0.92	-0.35	0.28	-0.89	-0.54

Table V: L_1 norm spatial convergence rates for various 2D axi-symmetric SGP calculations.

IV.D. Calculation Efficiency

An additional metric considered for 2D axi-symmetric calculations involves the 'wall clock time' (WCT) elapsed during the completion of a simulation. For this metric, a uniform grid spacing setup is constructed so that the simulation wall clock time approximately coincides with that elapsed during an AMR simulation. A variety of standard metrics can then be compared between the two simulations (see Tables VI and VII).

Metrics		*dr* = 0.04 cm (with AMR)	*dr* = 0.0063 cm (uniform)
$t = 12$	WCT (hr)	0.3599	0.3386
	# cells	19672	50193
	$L_1(\rho)$	4.4e-1	4.8e-2
	$L_1(e)$	1.4e-3	1.7e-4
	$L_1(P)$	3.5e-2	5.0e-4
	$L_1(v_s)$	1.1e-2	1.8e-3
$t = 13$	WCT (hr)	0.4003	0.3808
	# cells	12921	44122
	$L_1(\rho)$	6.0e-1	6.5e-2
	$L_1(e)$	1.7e-3	1.9e-4
	$L_1(P)$	5.5e-3	8.4e-4
	$L_1(v_s)$	1.0e-2	1.5e-3
$t = 14$	WCT (hr)	0.4518	0.4349
	# cells	18270	19164
	$L_1(\rho)$	5.8e-1	2.0e-1
	$L_1(e)$	4.9e-3	9.6e-4
	$L_1(P)$	4.2e-2	9.0e-3
	$L_1(v_s)$	1.5e-2	2.8e-3
$t = 15$	WCT (hr)	0.4940	0.4786
	# cells	95198	19164
	$L_1(\rho)$	3.6e0	4.8e-1
	$L_1(e)$	4.3e-3	1.2e-3
	$L_1(P)$	1.6e-1	2.1e-2
	$L_1(v_s)$	6.9e-3	1.2e-3
$t = 16$	WCT (hr)	0.5197	0.5040
	# cells	92213	19164
	$L_1(\rho)$	4.5e0	6.3e-1
	$L_1(e)$	5.0e-3	1.7e-3
	$L_1(P)$	1.3e-1	1.6e-2
	$L_1(v_s)$	7.0e-3	1.3e-3
$t = 17$	WCT (hr)	0.5381	0.5228
	# cells	82765	15885
	$L_1(\rho)$	7.0e0	8.0e-1
	$L_1(e)$	7.0e-3	2.3e-3
	$L_1(P)$	1.2e-1	1.3e-2
	$L_1(v_s)$	8.6e-3	1.4e-3

Table VI: Uniform grid and AMR simulations as benchmarked by equal wall clock times (on the LANL 'yellowrail' HPC cluster, 256 PEs/simulation).

Metrics		*dr* = 0.02 cm (with AMR)	*dr* = 0.0046 cm (uniform)
$t = 12$	WCT (hr)	0.8988	0.8845
	# cells	41415	93810
	$L_1(\rho)$	2.1e-1	3.4e-2
	$L_1(e)$	6.6e-4	1.1e-4
	$L_1(P)$	1.9e-2	3.8e-4
	$L_1(v_s)$	4.9e-3	1.2e-3
$t = 13$	WCT (hr)	1.0035	1.0076
	# cells	27127	44122
	$L_1(\rho)$	3.0e-1	4.6e-2
	$L_1(e)$	7.7e-4	1.3e-4
	$L_1(P)$	3.0e-3	6.5e-4
	$L_1(v_s)$	4.9e-3	1.1e-3
$t = 14$	WCT (hr)	1.1451	1.1572
	# cells	23065	36651
	$L_1(\rho)$	3.0e-1	1.4e-1
	$L_1(e)$	4.0e-3	6.6e-4
	$L_1(P)$	2.7e-2	6.4e-3
	$L_1(v_s)$	1.1e-2	2.1e-3
$t = 15$	WCT (hr)	1.2422	1.2663
	# cells	122837	36651
	$L_1(\rho)$	1.7e0	3.4e-1
	$L_1(e)$	2.6e-3	9.5e-4
	$L_1(P)$	7.8e-2	1.4e-2
	$L_1(v_s)$	3.8e-3	8.6e-4
$t = 16$	WCT (hr)	1.2979	1.3330
	# cells	49101	36651
	$L_1(\rho)$	2.3e0	4.4e-1
	$L_1(e)$	3.4e-3	1.3e-3
	$L_1(P)$	6.3e-2	1.1e-2
	$L_1(v_s)$	3.8e-3	9.2e-4
$t = 17$	WCT (hr)	1.33995	1.3840
	# cells	60161	36651
	$L_1(\rho)$	3.2e0	5.5e-1
	$L_1(e)$	4.6e-3	1.7e-3
	$L_1(P)$	5.4e-2	8.7e-3
	$L_1(v_s)$	4.6e-3	1.1e-3

Table VII: Uniform grid and AMR simulations as benchmarked by equal wall clock times (on the LANL 'yellowrail' HPC cluster, 256 PEs/simulation).

Tables VI and VII show that for equal wall clock time, both uniform-grid simulations result in fewer computational zones and universally-better L_1 error norms for all variables, at all simulation times of interest. This result, in conjunction with those already presented, suggest that the AMR settings used for the 2D axi-symmetric studies should be adjusted and assessed for utility in the context of the SGP and related test problems.

V. SUMMARY AND RECOMMENDATIONS FOR FUTURE STUDY

This report has provided details and explanation surrounding the simulation of two converging shock wave test problems in the LANL ASC code xRAGE: the Guderley problem, and a newly developed surrogate Guderley problem (SGP). Simulations of one of these problems were conducted in 1D spherical symmetry and on square grids in 2D axi-symmetry, with and without select adaptive mesh refinement (AMR) options enabled. A variety of qualitative and quantitative comparison metrics were determined for most of the problems simulated.

A principal conclusion of this work is that AMR options can be applied to converging shock problems in both 1D and 2D, and that associated qualitative metrics seem promising. From the quantitative standpoint, however, it appears that further investigation into additional xRAGE AMR settings is warranted. According to the xRAGE code manual and online documentation, there are at least two additional AMR options that can be used, and numerous variations and parameter settings within each broader class. It remains to be seen what effect, if any, these additional options will have on the oscillation and other phenomena seen in both 1D and 2D result sets.

In addition, this report has made use of only a few quantitative comparison metrics, most prominently the spatial L_1 error norm and its convergence characteristics using a specific set of initial grid resolutions. Other metrics that should be considered in future studies include (but are not limited) shock positions, the central post-shock pressure at a given time, and temporal convergence characteristics. Additional spatial convergence characteristics (e.g., the efficiency metric as used in Sec. IV.C) might also be considered or devised for AMR calculations. Inter-code comparisons may also prove useful from both the qualitative and quantitative standpoints.

In any event, this work represents only the initial effort of the large body of work that will need to be completed for a thorough and accurate assessment of the relevant xRAGE code capabilities.

REFERENCES

1. J. KAMM, J. BROCK, S. BRANDON, D. COTRELL, B. JOHNSON, P. KNUPP, W. RIDER, T. TRUCANO, V. WEIRS, "Enhanced Verification Test Suite for Physics Simulation Codes," LA-14379, Los Alamos National Laboratory (2008).

2. S. RAMSEY and G. HRBEK, "Semi-Analytical Investigation of Strong Converging Shock Waves (U)", LA-UR-06-6739, Los Alamos National Laboratory (2006).

3. S. RAMSEY, "A Rigorous Investigation of the Self-Similar Converging-Reflected Shock Wave Standard Solution Mode," LA-UR-07-5261, Los Alamos National Laboratory (2007).

4. S. RAMSEY, "Evaluation of the Guderley Converging Shock Wave Standard Solution Mode," LA-UR-08-05442, Los Alamos National Laboratory (2008).

5. S. RAMSEY, "Guderley Test Problem Definition," LA-UR-11-02765, Los Alamos National Laboratory (2011).

6. S. RAMSEY, J. KAMM, and J. BOLSTAD, "The Guderley Problem Revisited," *Int. J. Comput. Fluid Dyn.* **26**, 79-99 (2012).

7. S. RAMSEY, "Preliminary Results for Converging Shock Wave Problems," unclassified report, Los Alamos National Laboratory (2012).

8. G. GUDERLEY, "Starke kugelige und zylinderische Verdichtungsstöße in der Nähe des Kugelmittelpunktes bzw. der Zylinderasche," *Luftfahrtforschung* **19**, 302-312 (1942).

9. K. STANYUKOVICH, *Unsteady Motion of Continuous Media*, Pergammon Press, New York (1970).

10. R. LAZARUS, "Self-Similar Solutions for Converging Shocks and Collapsing Cavities," *SIAM J. Numer. Anal.* **18**, 316-371 (1981).

11. E. CARAMANA and P. WHALEN, "Numerical Properties of Symmetry Properties of Continuum Problems," *J. Comp. Phys.* **141**, 174 (1998).

12. P. WHALEN, personal communication, August 2011-April 2012.

13. T. MASSER, personal communication, August 2011-April 2012.

14. J. QUIRK, personal communication, August 2011-April 2012.

15. W. NOH, "Errors for Calculations of Strong Shocks Using an Artificial Viscosity and an Artificial Heat Flux," *J. Comp. Phys.* **72**, 78 (1978).

16. Wolfram Research, Inc., Mathematica, Version 7.0, Champaign, IL (2008).

17. M. MCKAY, xRAGE version 1109.00 release notes, Los Alamos National Laboratory (2011).

GUIDE TO APPENEDICES

APPENDIX A: ADDITIONAL SIMULATION RESULTS

A.1: 1D Spherical Symmetry, Uniform Grid

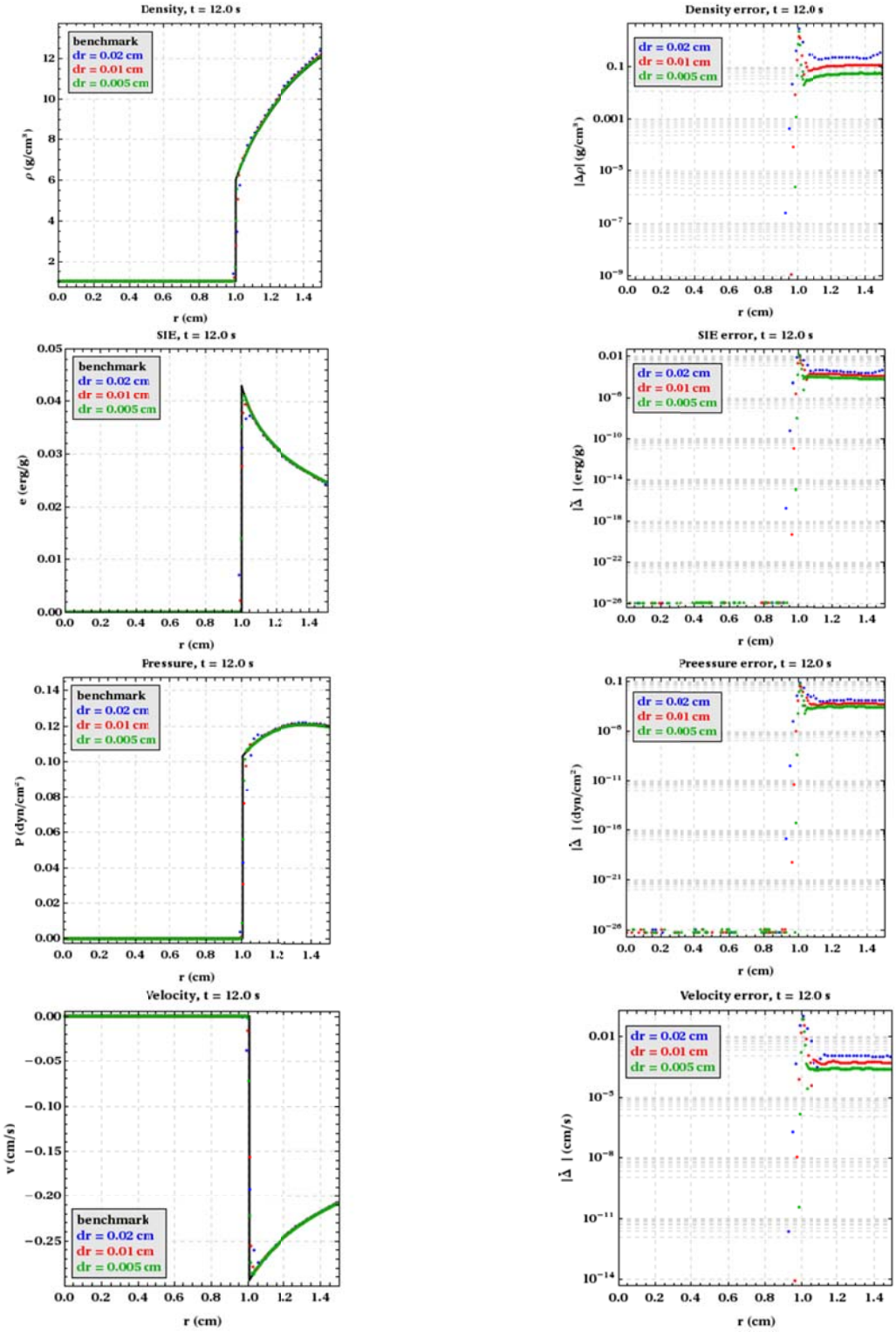

Figure A.1: 1D spherical SGP results at *t* = 12 s.

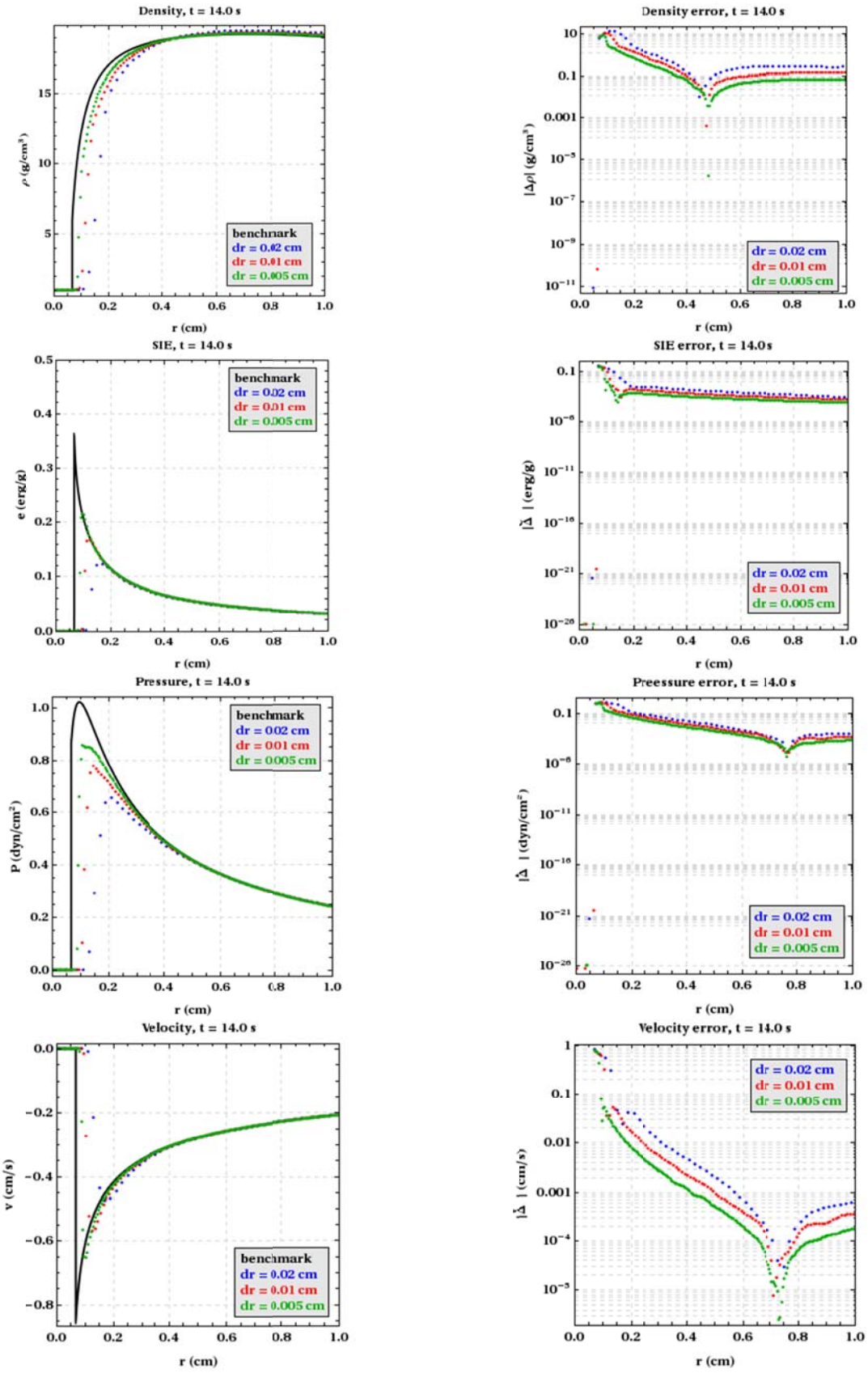

Figure A.2: 1D spherical SGP results at t = 14 s.

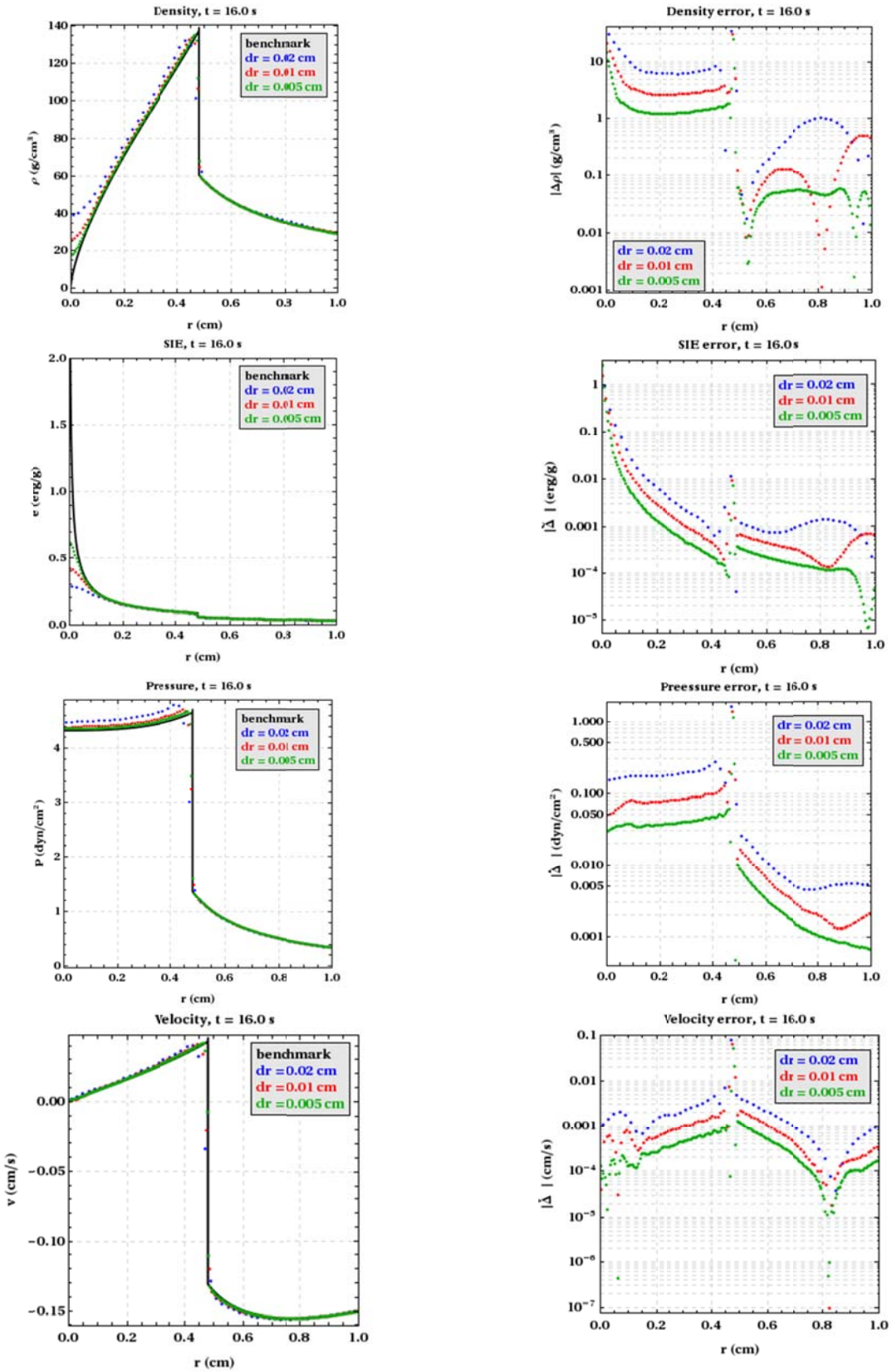

Figure A.3: 1D spherical SGP results at t = 16 s.

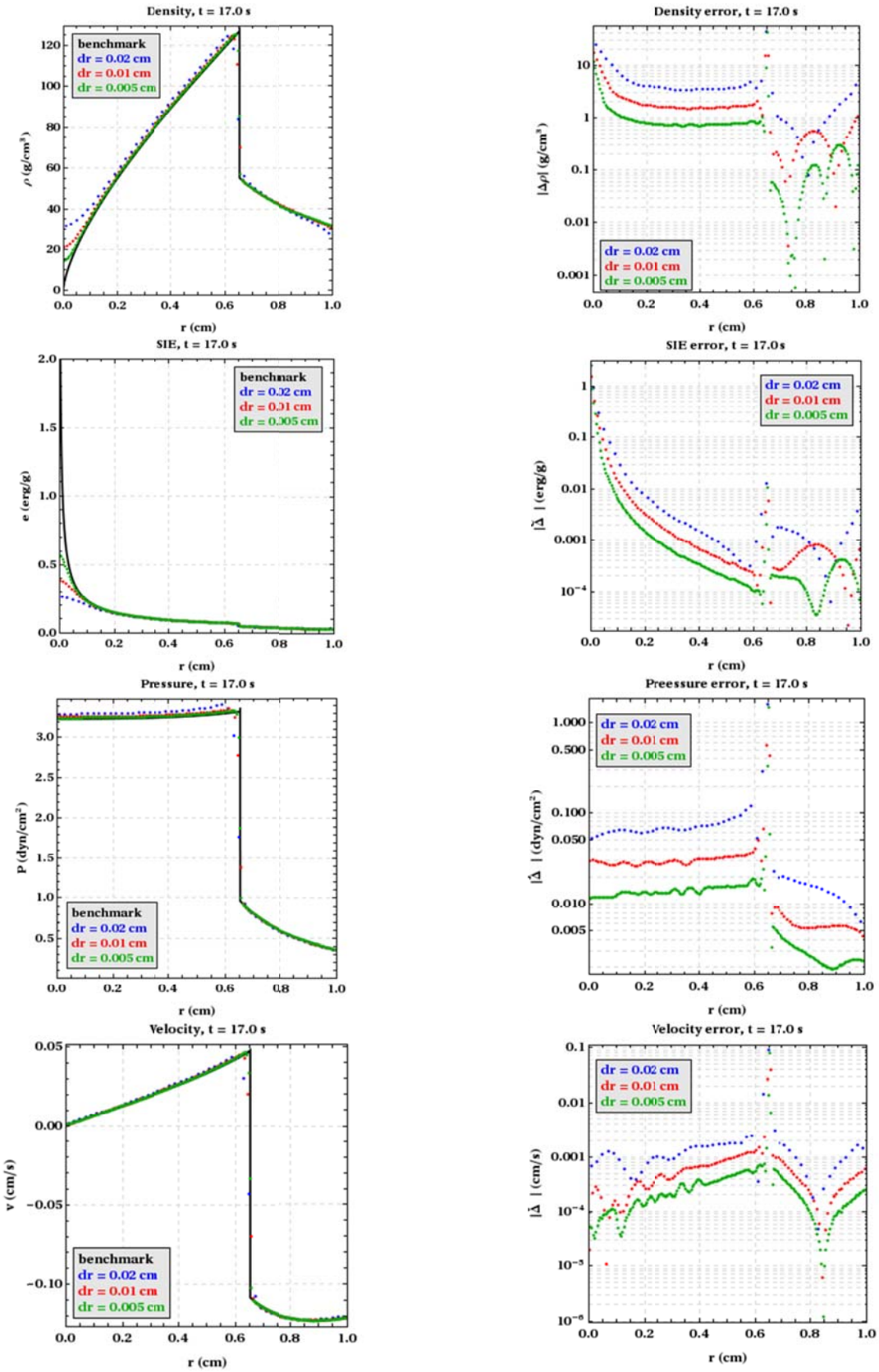

Figure A.4: 1D spherical SGP results at t = 17 s.

A.2: 1D Spherical Symmetry, Adaptive Mesh Refinement

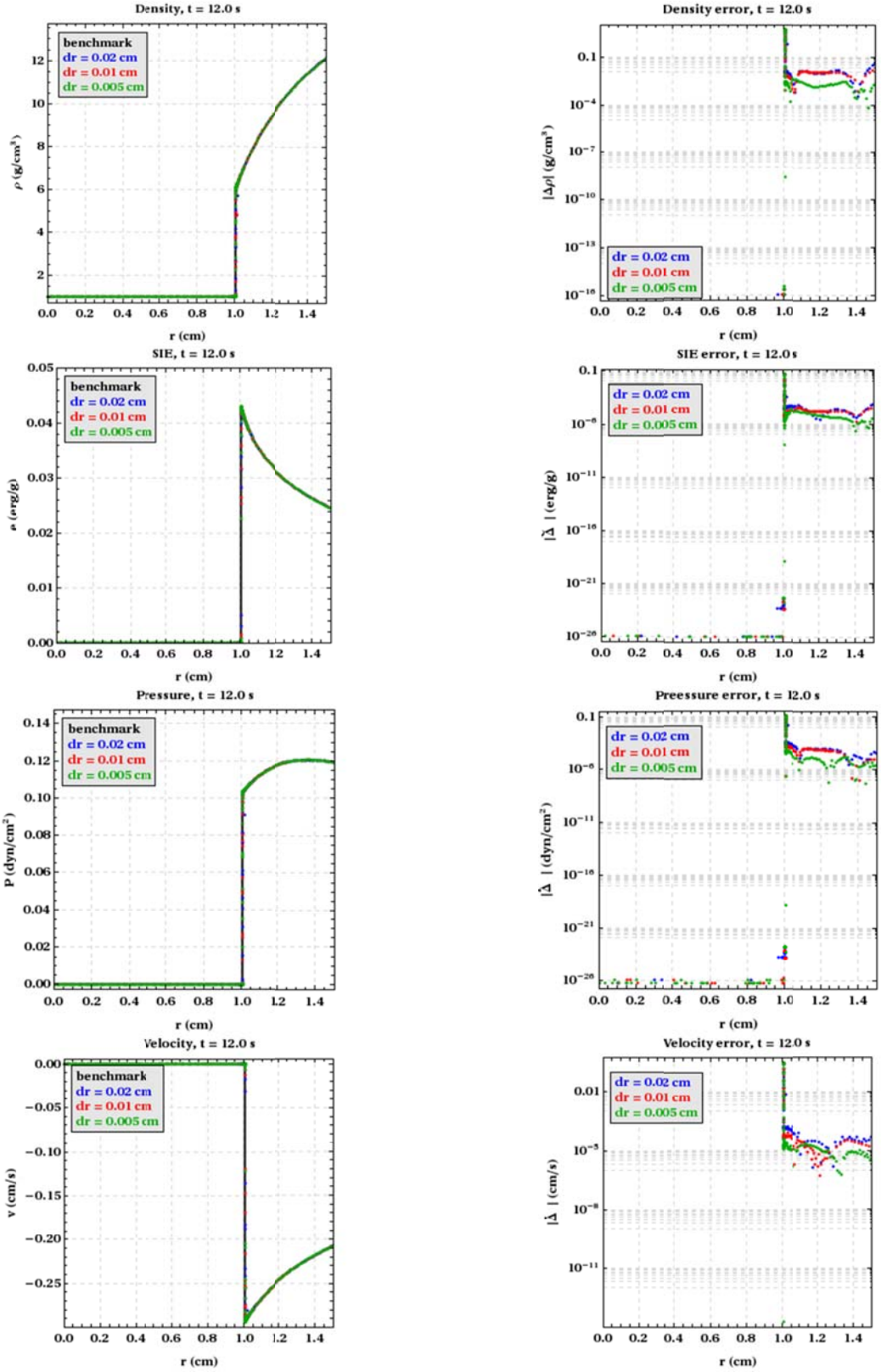

Figure A.5: 1D spherical SGP results at *t* = 12 s with AMR enabled.

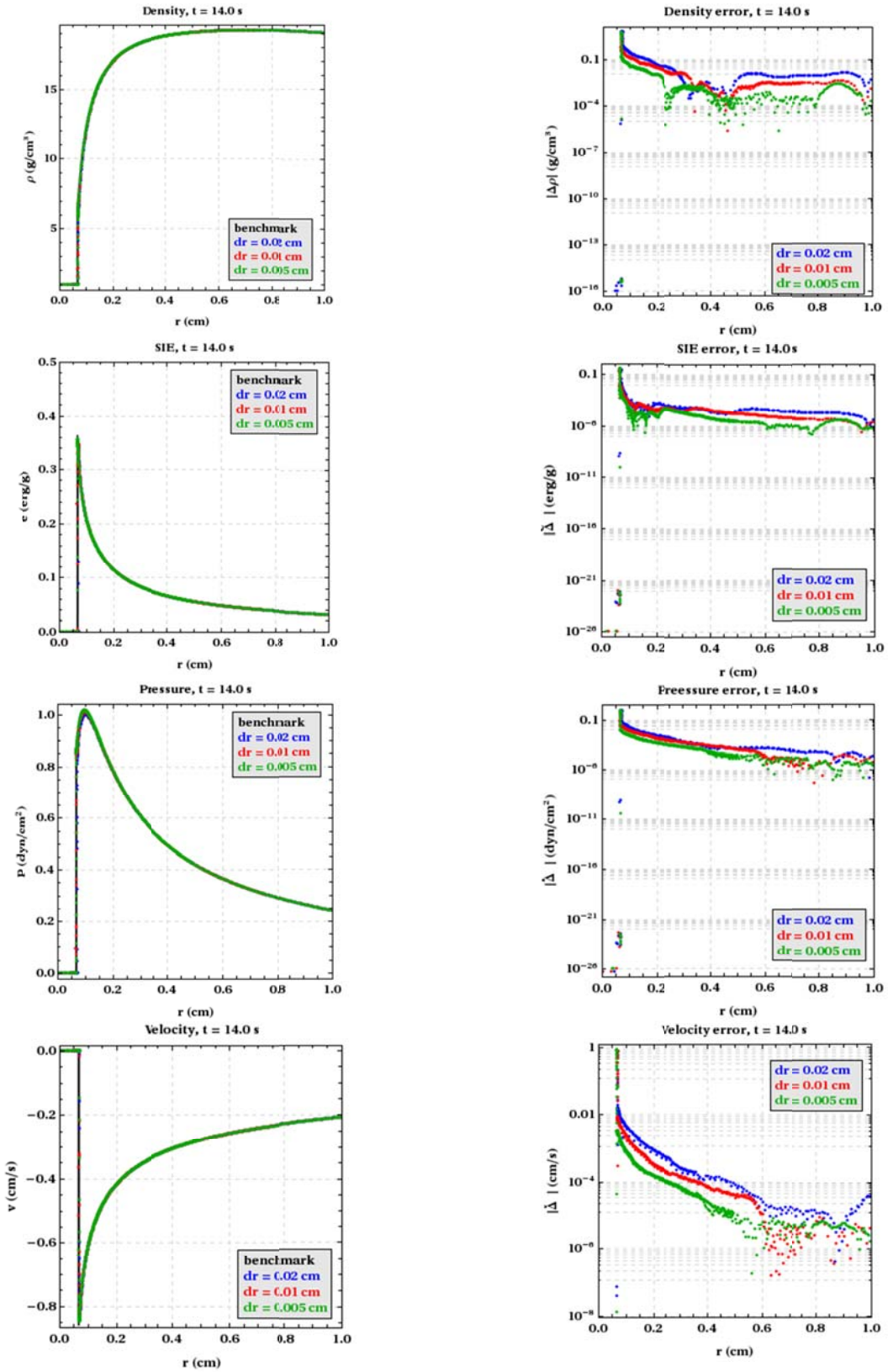

Figure A.6: 1D spherical SGP results at t = 14 s with AMR enabled.

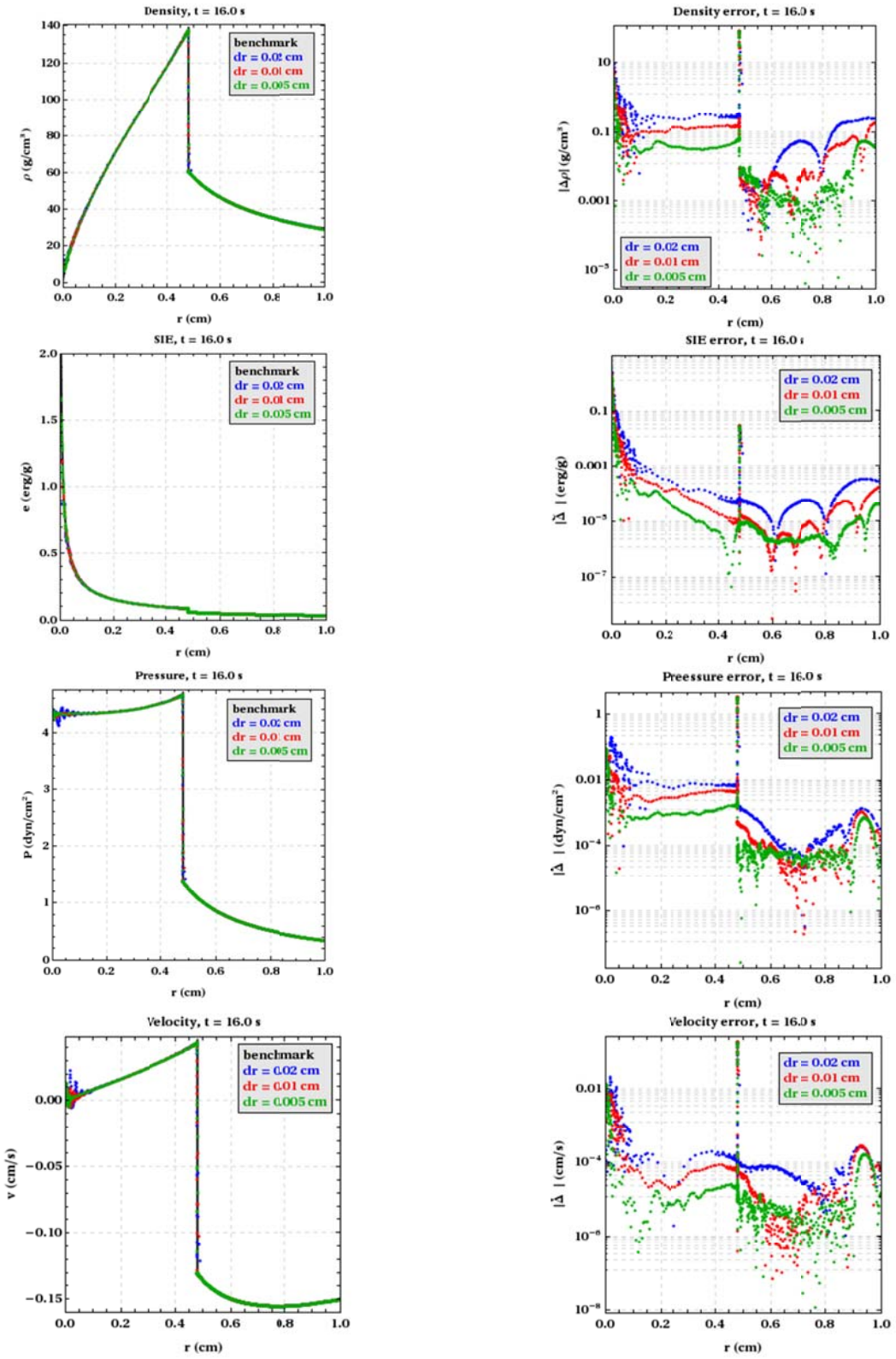

Figure A.7: 1D spherical SGP results at *t* = 16 s with AMR enabled.

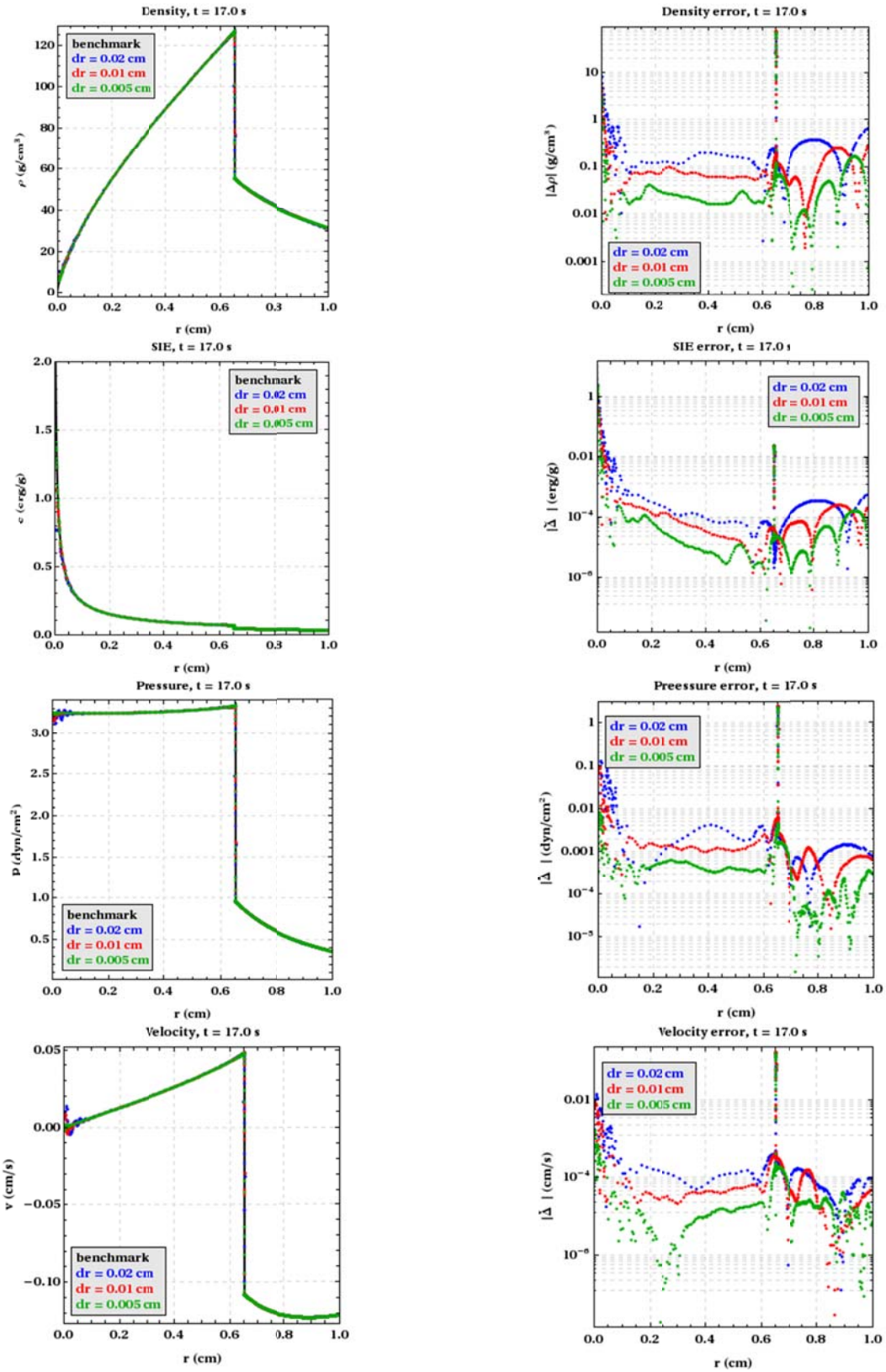

Figure A.8: 1D spherical SGP results at *t* = 17 s with AMR enabled.

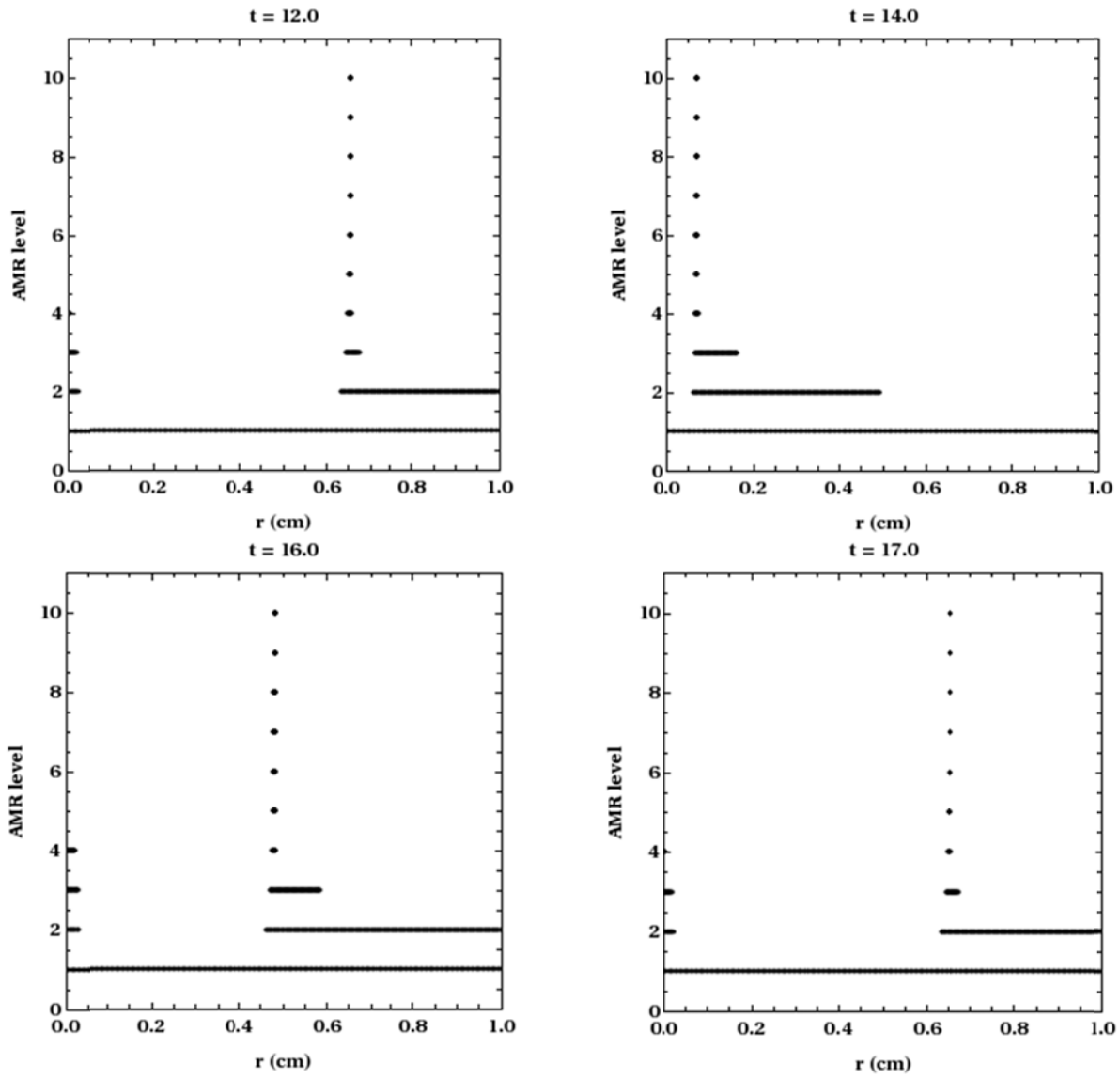

Figure A.9: Clockwise from top left - 1D spherical SGP AMR level results at *t* = 12, 14, 16, and 17 s.

A.3: 1D Spherical Symmetry, Simulation Comparison Metrics

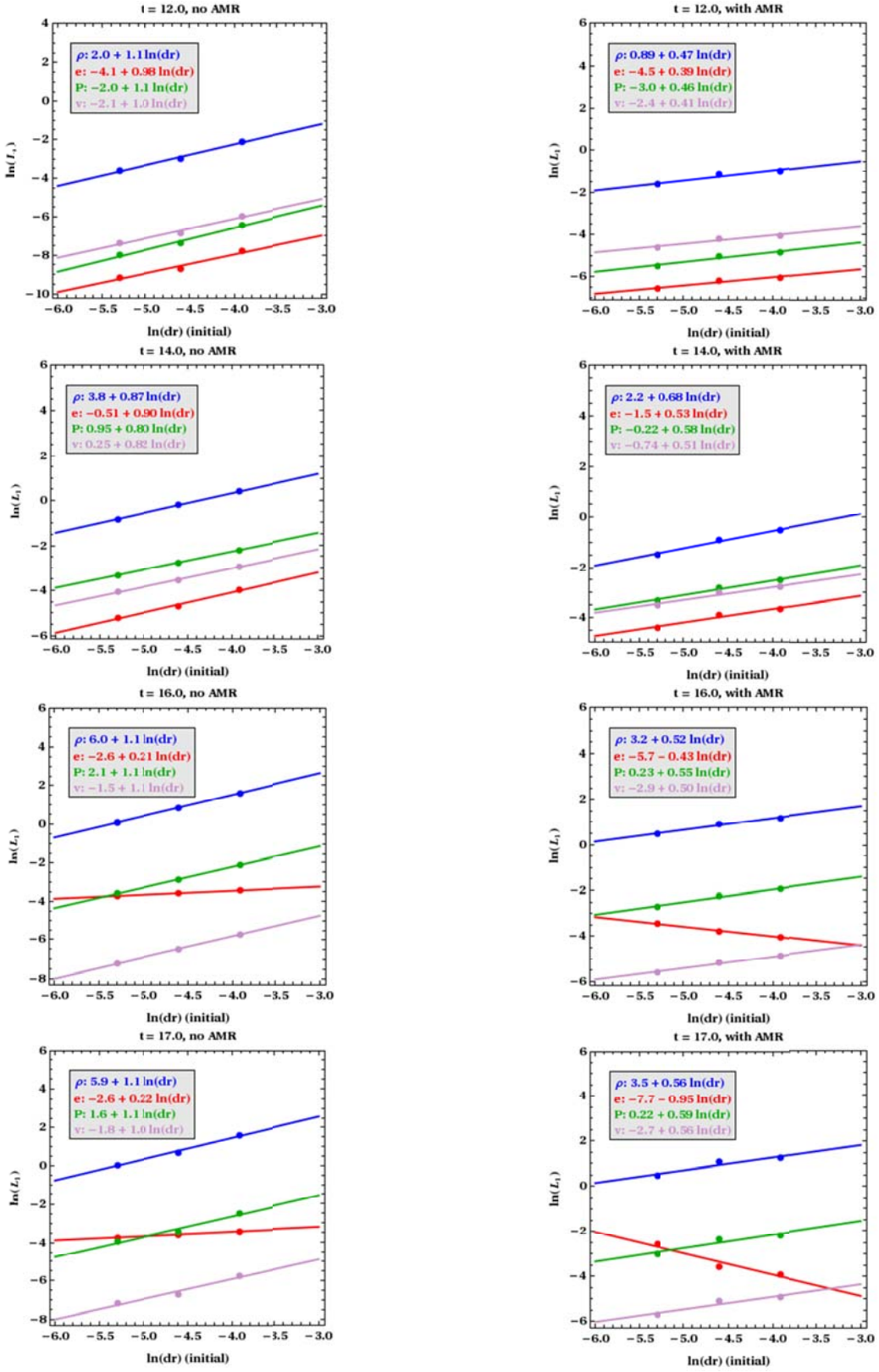

Figure A.10: L_1 norm spatial convergence curves for 1D spherical SGP at t = 12, 14, 16, and 17 s.

A.4: 2D Axi-Symmetry, Uniform Grid

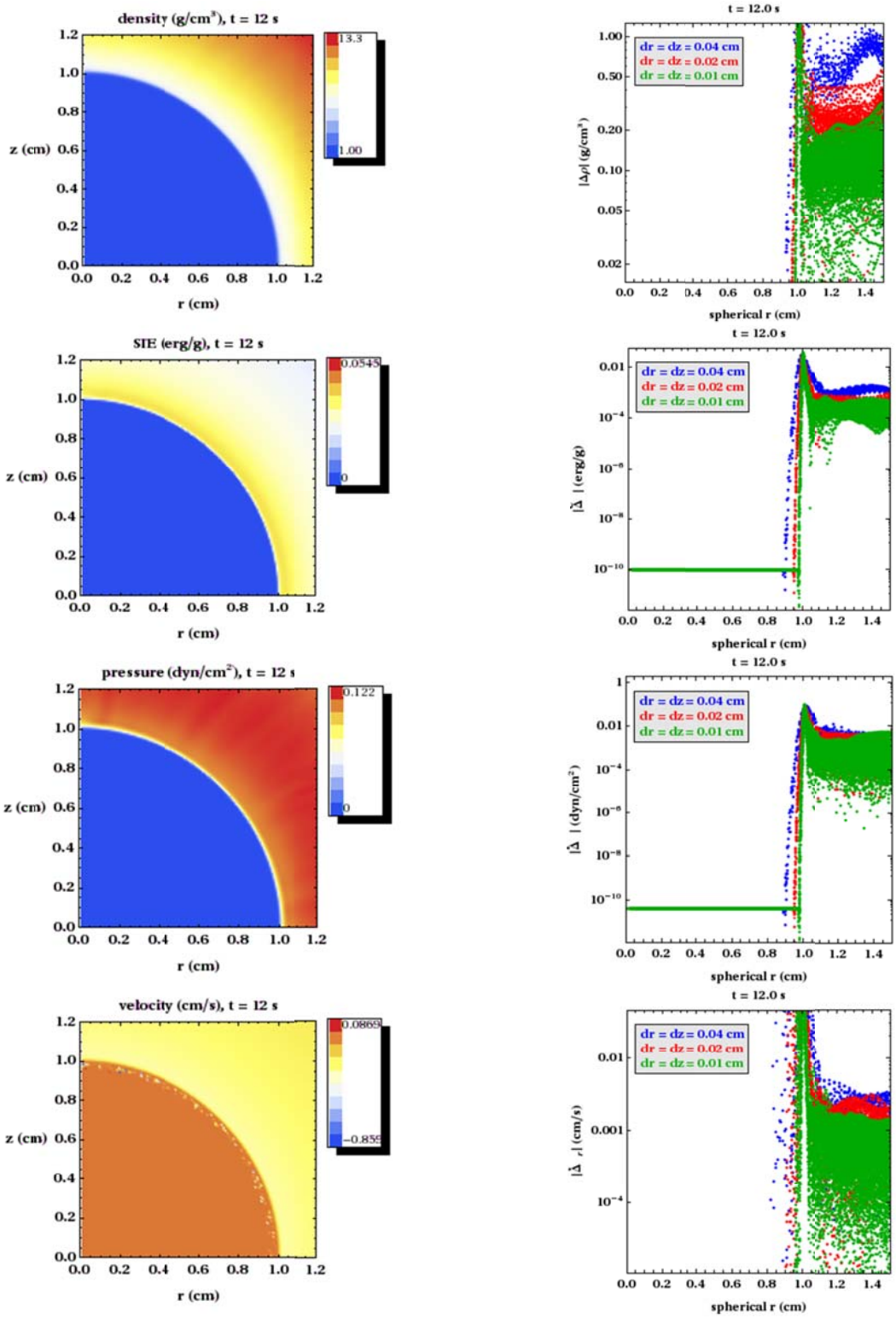

Figure A.11: Left – 2D axi-symmetric SGP results for *dr* = *dz* = 0.01 cm at *t* = 12 s. Right – solution error on three different grids, calculated using Eq. (5).

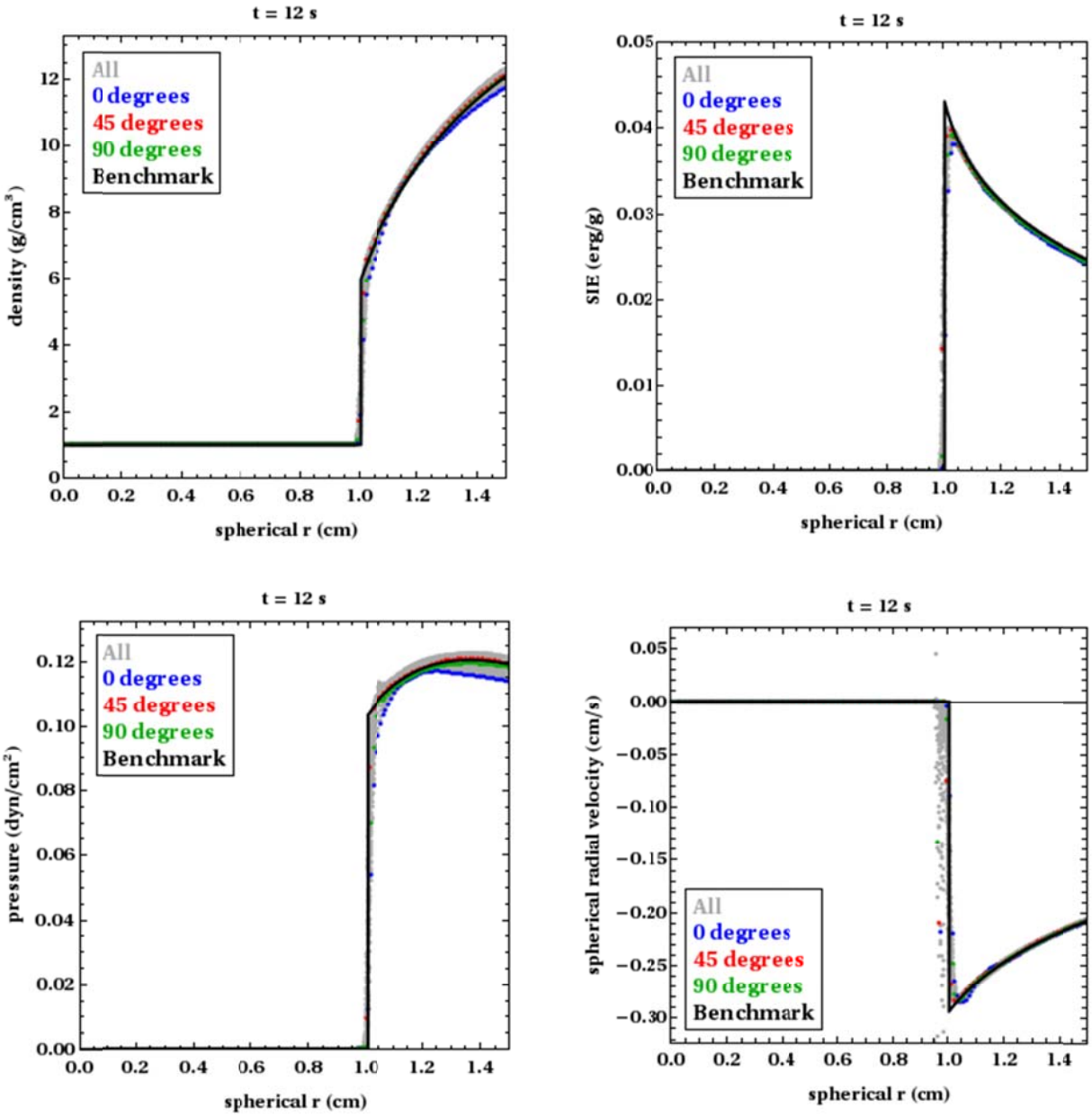

Figure A.12: 2D axi-symmetric SGP line-out results for *dr* = *dz* = 0.01 cm at *t* = 12 s.

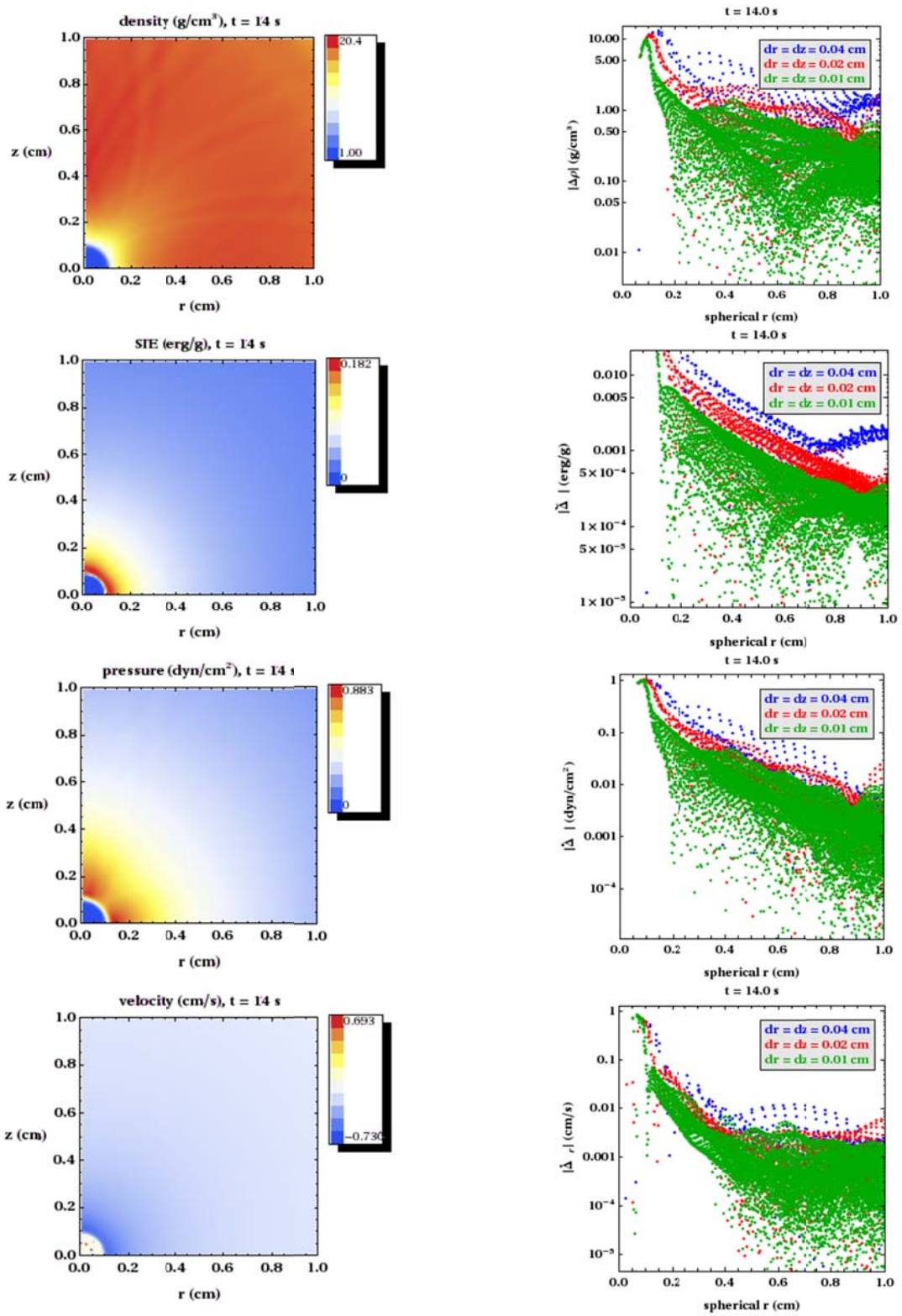

Figure A.13: Left – 2D axi-symmetric SGP results for *dr* = *dz* = 0.01 cm at *t* = 14 s. Right – solution error on three different grids, calculated using Eq. (5).

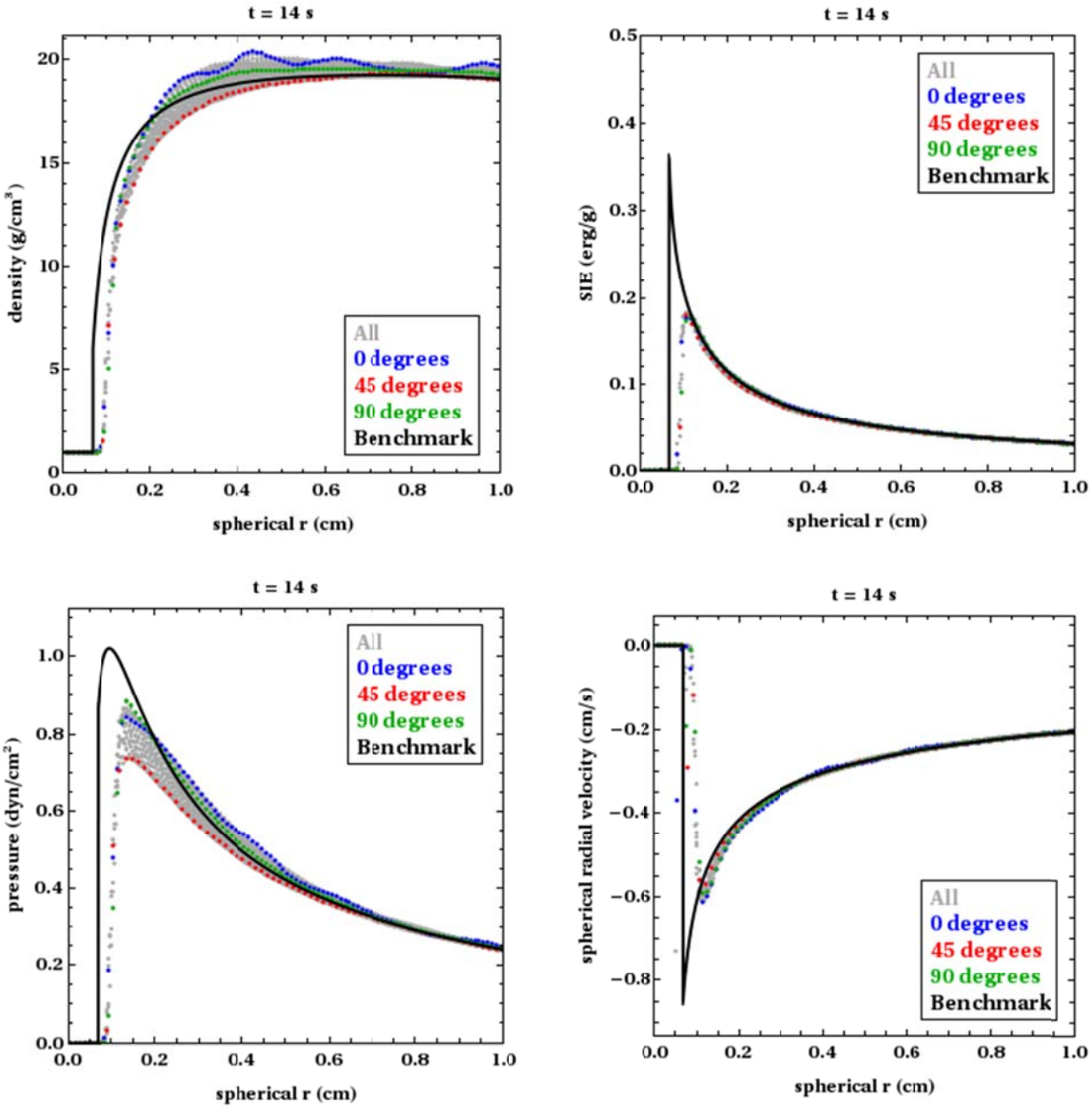

Figure A.14: 2D axi-symmetric SGP line-out results for *dr* = *dz* = 0.01 cm at *t* = 14 s.

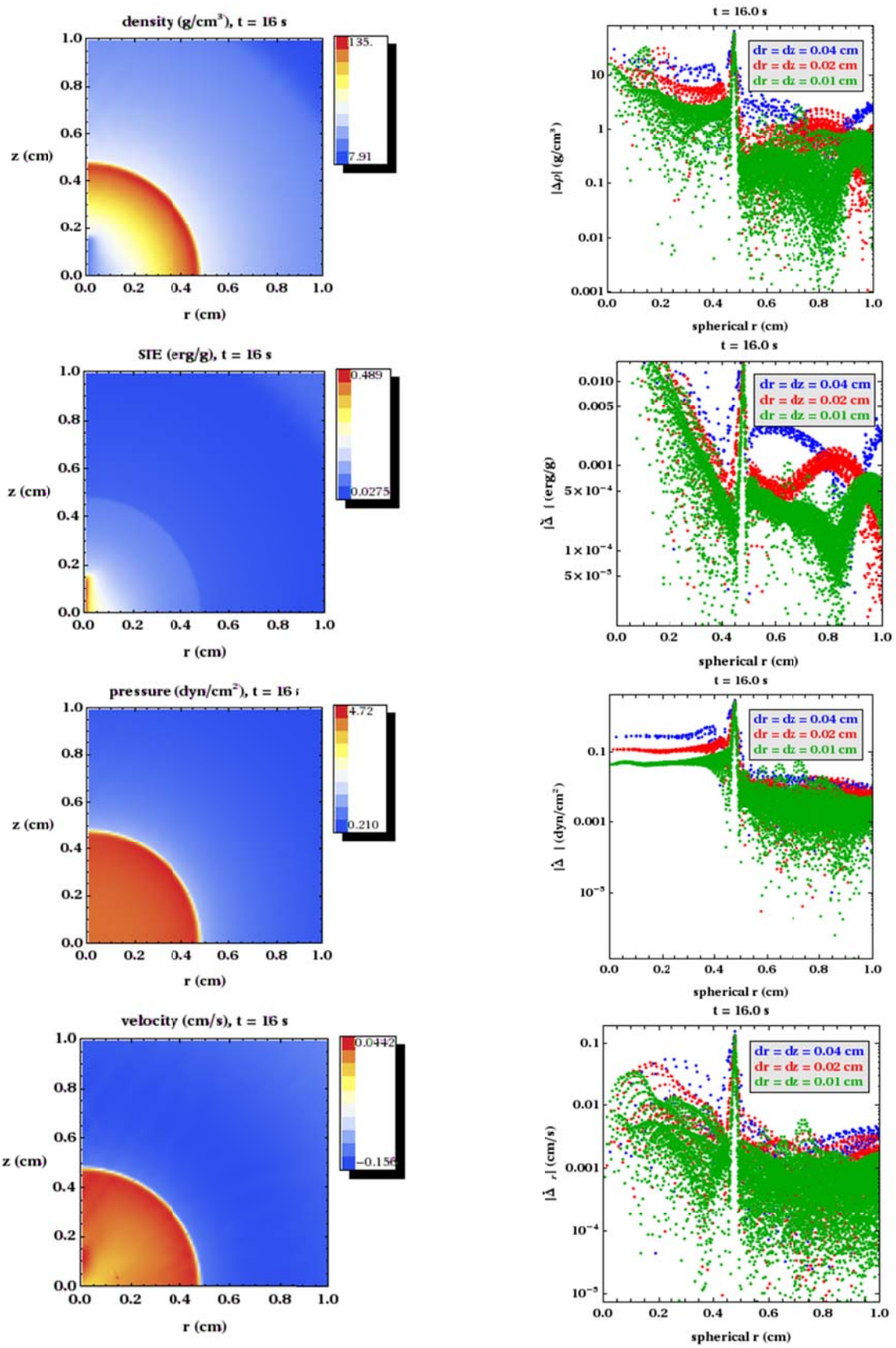

Figure A.15: Left – 2D axi-symmetric SGP results for *dr* = *dz* = 0.01 cm at *t* = 16 s. Right – solution error on three different grids, calculated using Eq. (5).

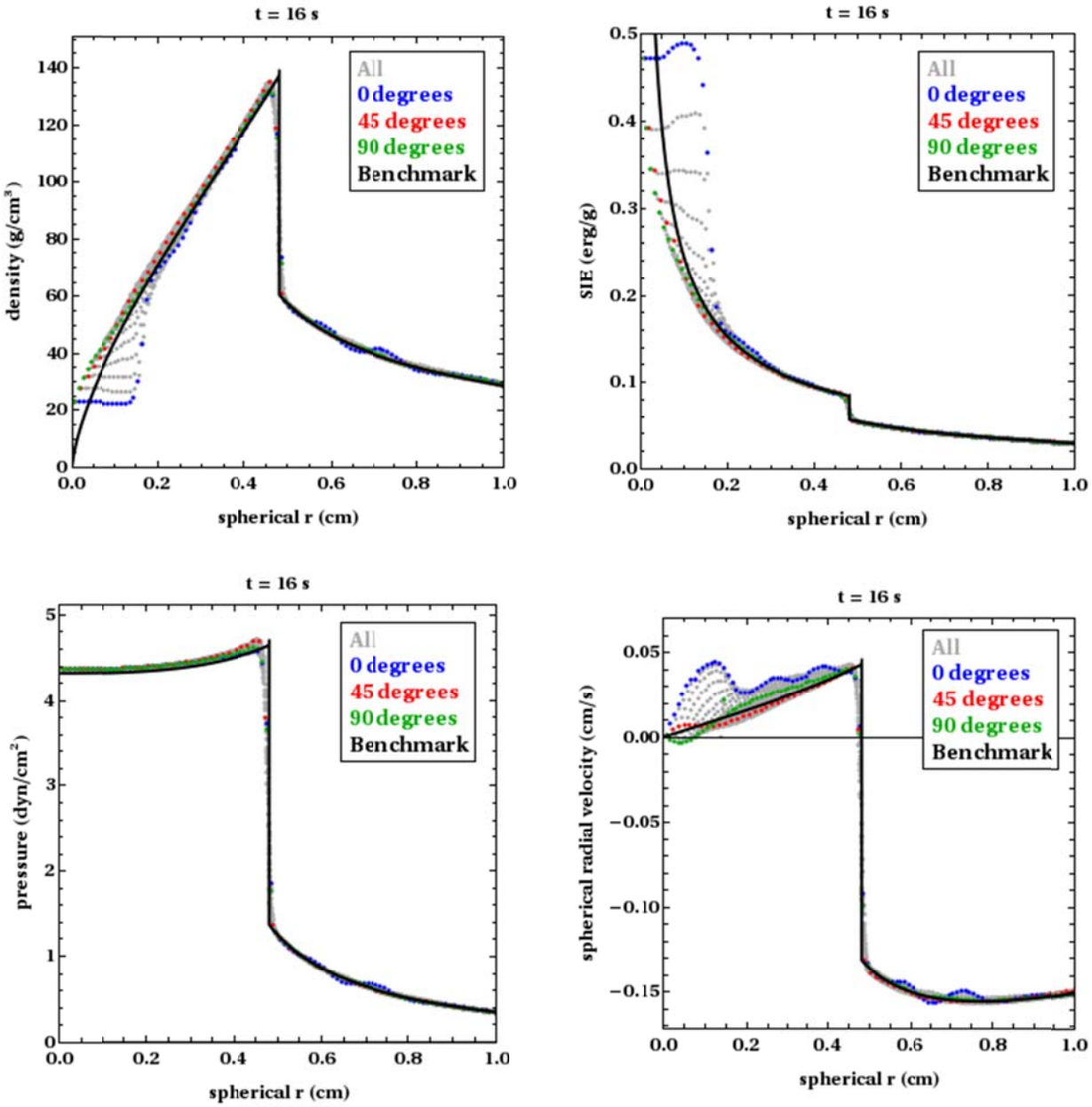

Figure A.16: 2D axi-symmetric SGP line-out results for *dr* = *dz* = 0.01 cm at *t* = 16 s.

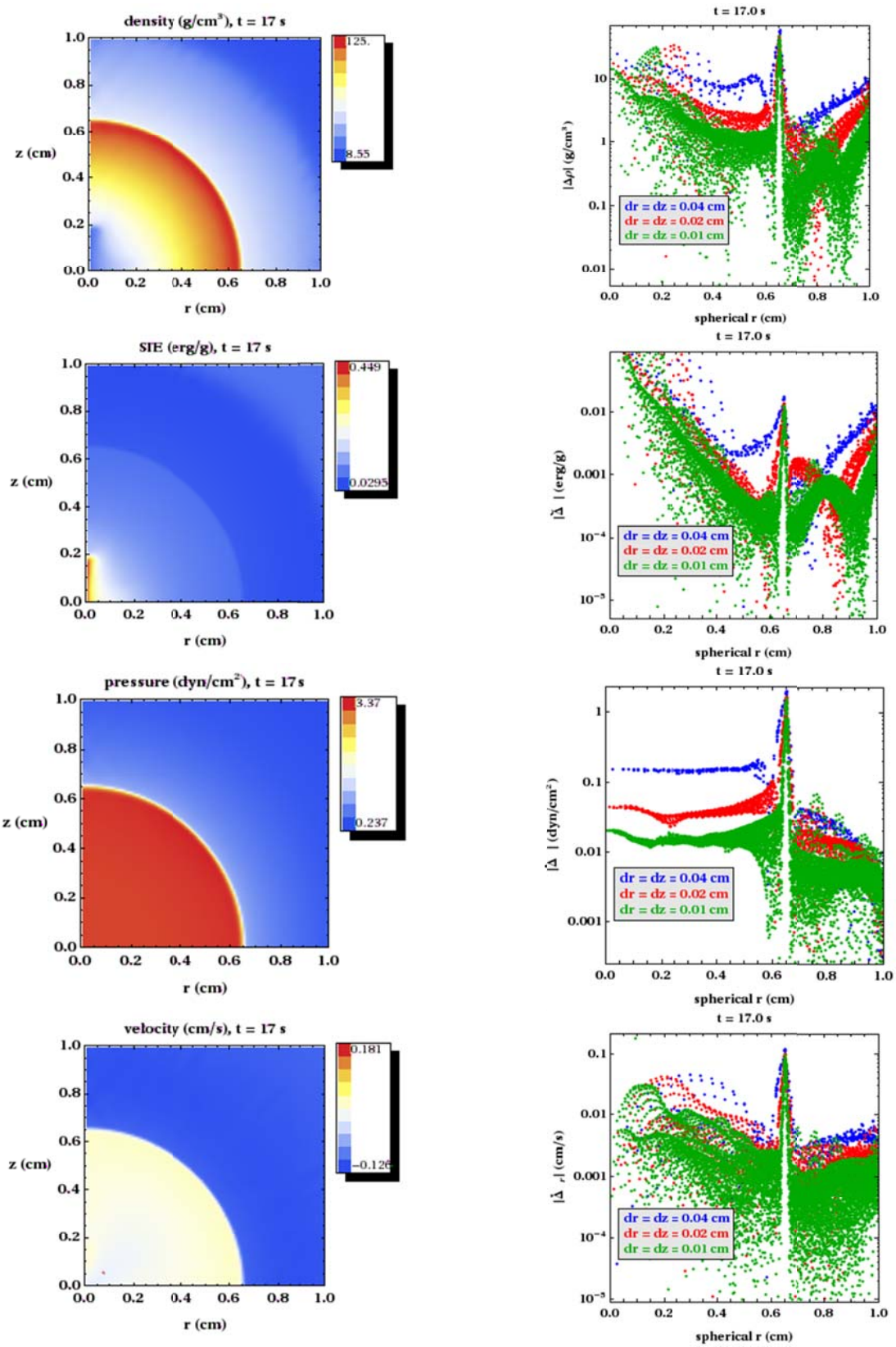

Figure A.17: Left – 2D axi-symmetric SGP results for *dr* = *dz* = 0.01 cm at *t* = 17 s. Right – solution error on three different grids, calculated using Eq. (5).

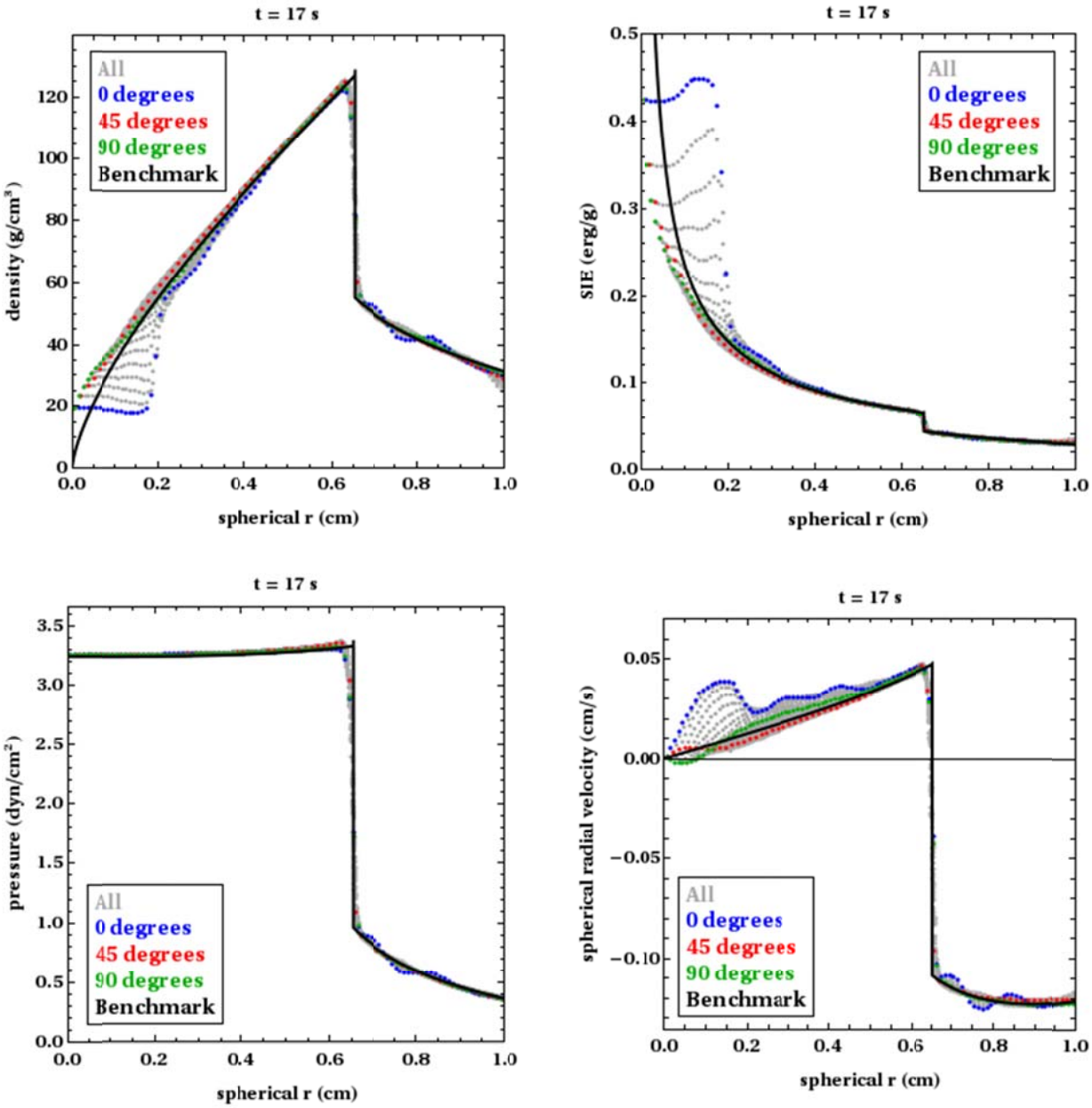

Figure A.18: 2D axi-symmetric SGP line-out results for *dr* = *dz* = 0.01 cm at *t* = 17 s.

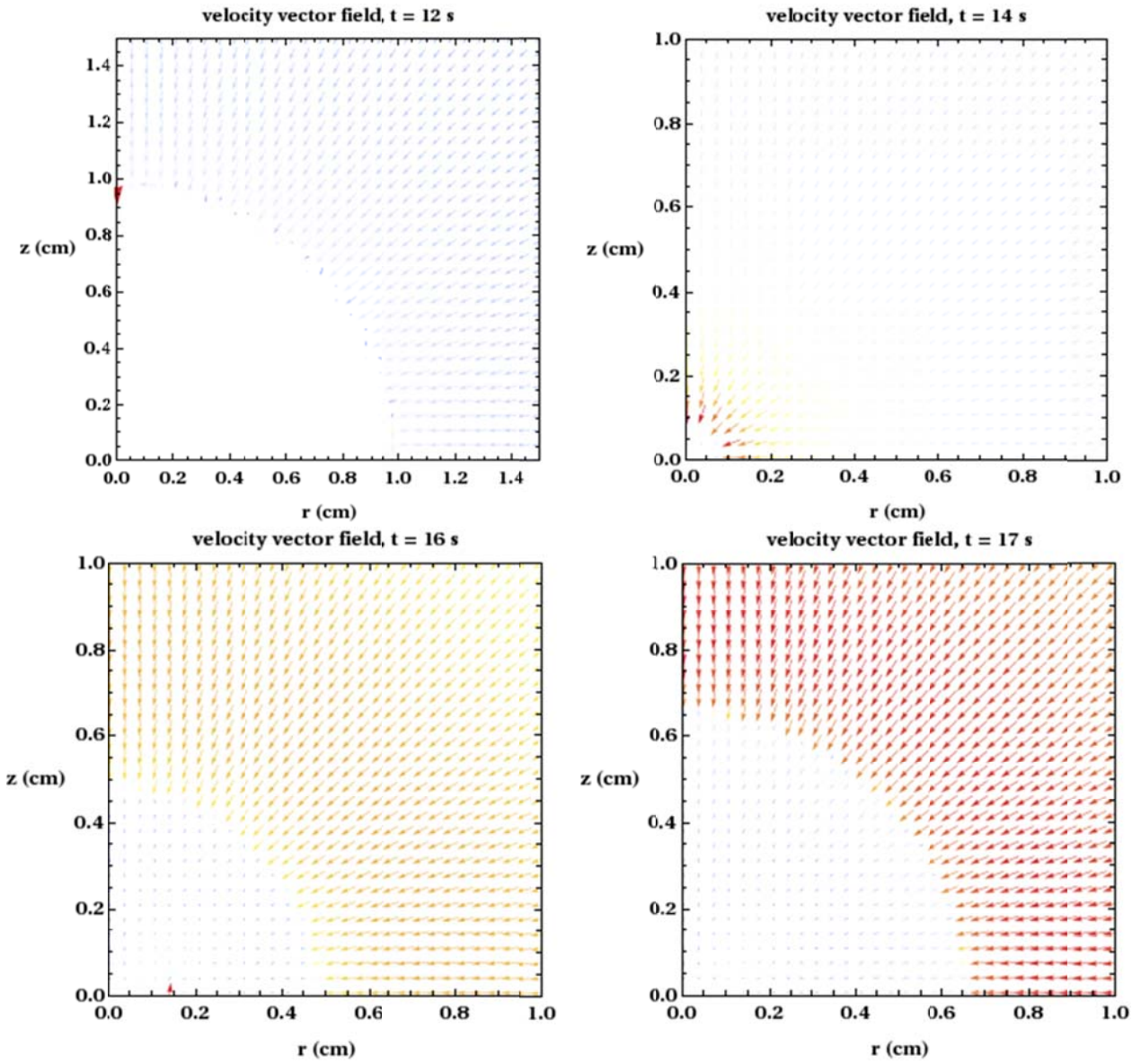

Figure A.19: Clockwise from top left – 2D axi-symmetric SGP velocity vector results for *dr* = *dz* = 0.01 cm at *t* = 12, 14, 16, and 17 s.

A.5. 2D Axi-Symmetry, Adaptive Mesh Refinement

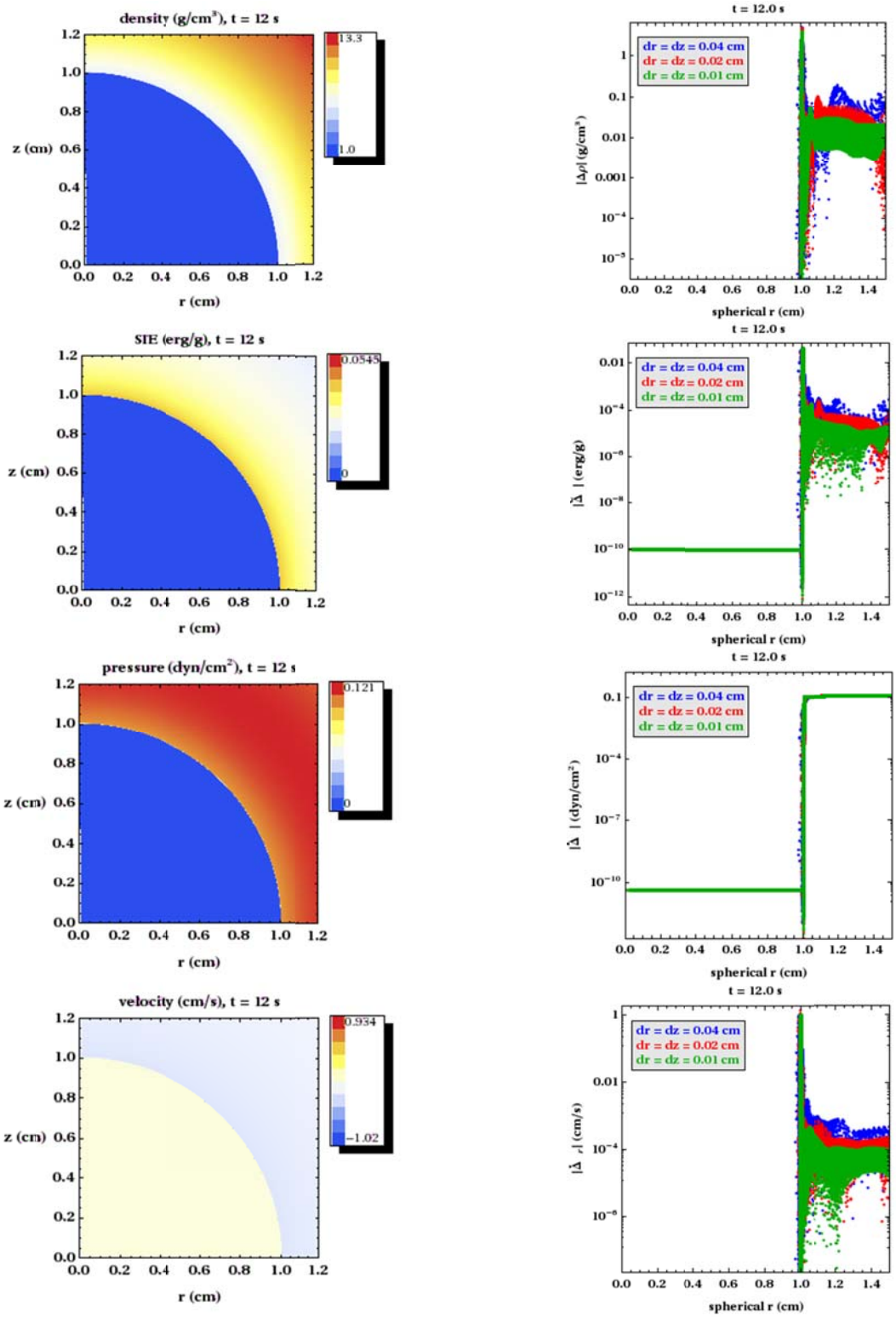

Figure A.20: Left – 2D axi-symmetric SGP results for initial *dr* = *dz* = 0.01 cm at *t* = 12 s with AMR enabled. Right – solution error on three different initial grids, calculated using Eq. (5).

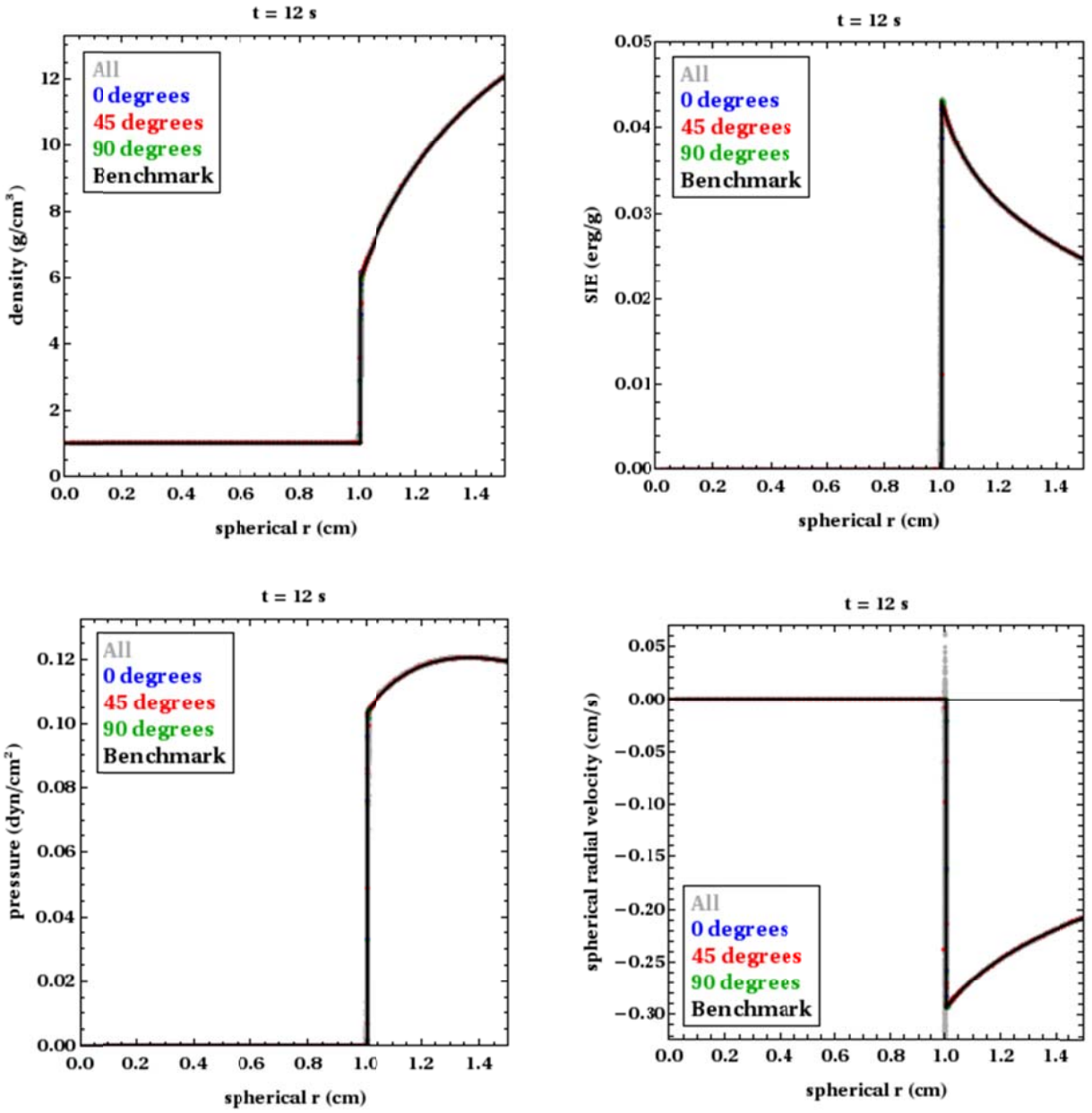

Figure A.21: 2D axi-symmetric SGP line-out results for initial *dr* = *dz* = 0.01 cm at *t* = 12 s with AMR enabled.

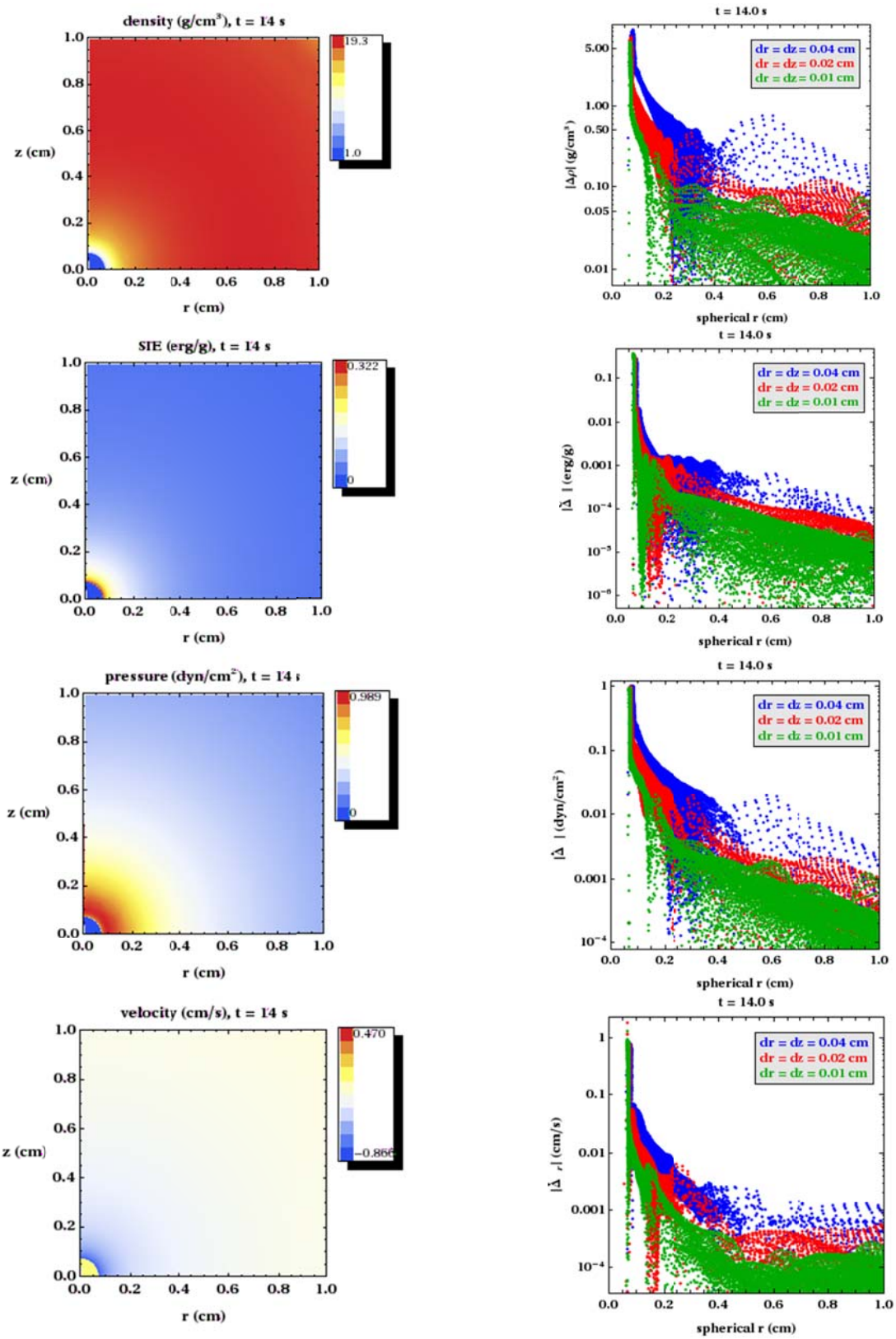

Figure A.22: Left – 2D axi-symmetric SGP results for initial *dr* = *dz* = 0.01 cm at *t* = 14 s with AMR enabled. Right – solution error on three different initial grids, calculated using Eq. (5).

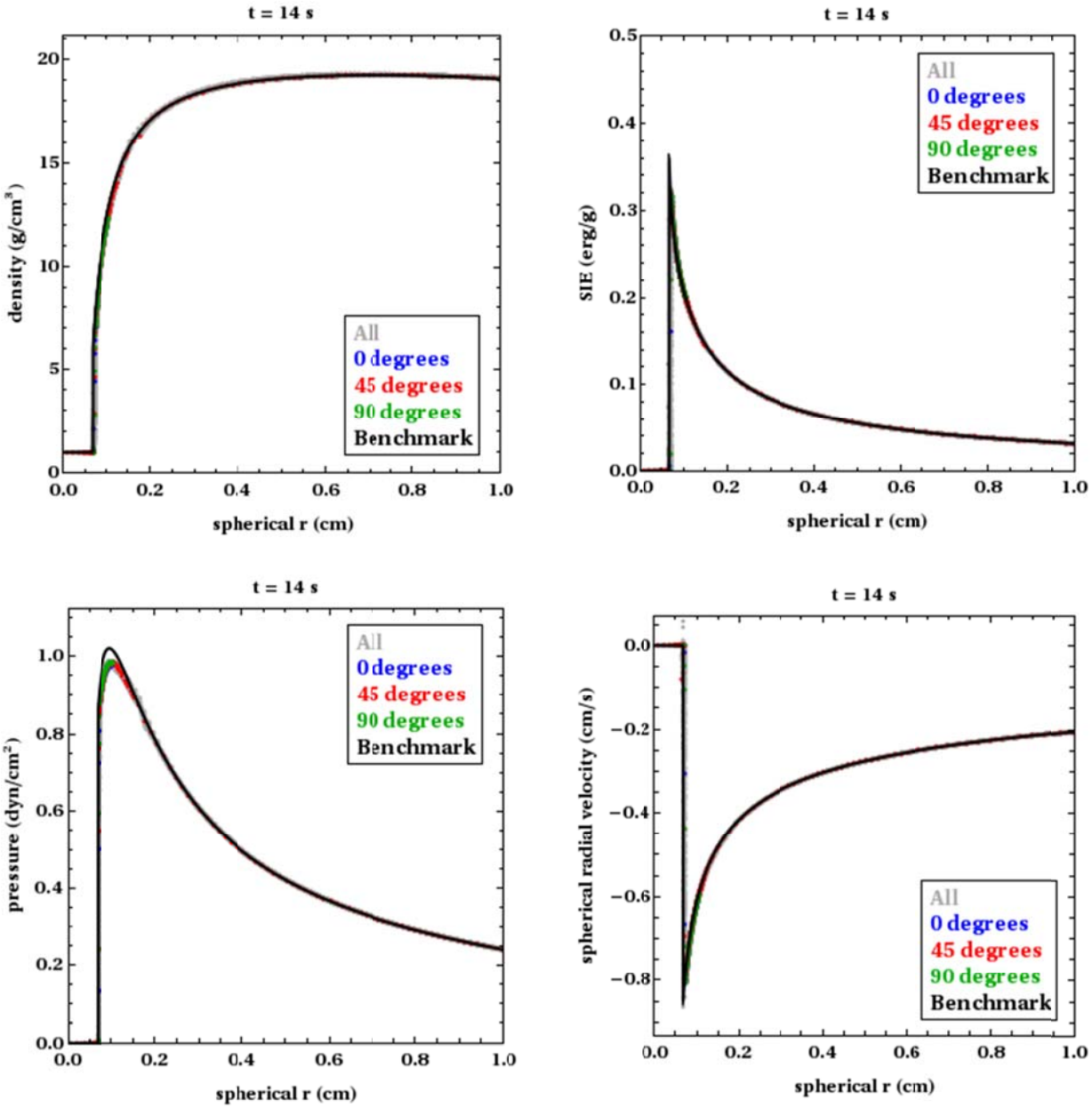

Figure A.23: 2D axi-symmetric SGP line-out results for initial *dr* = *dz* = 0.01 cm at *t* = 14 s with AMR enabled.

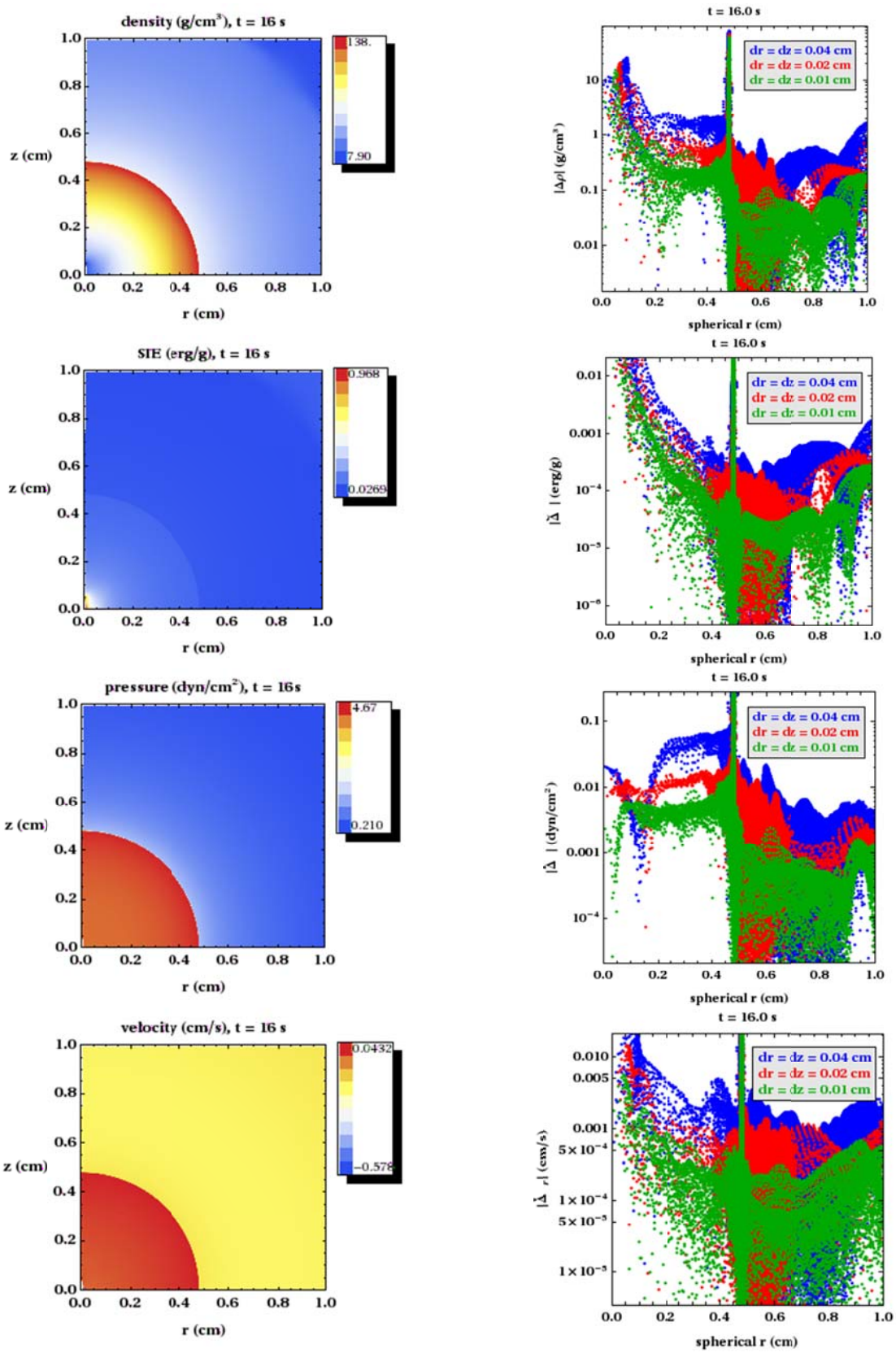

Figure A.24: Left – 2D axi-symmetric SGP results for initial *dr* = *dz* = 0.01 cm at *t* = 16 s with AMR enabled. Right – solution error on three different initial grids, calculated using Eq. (5).

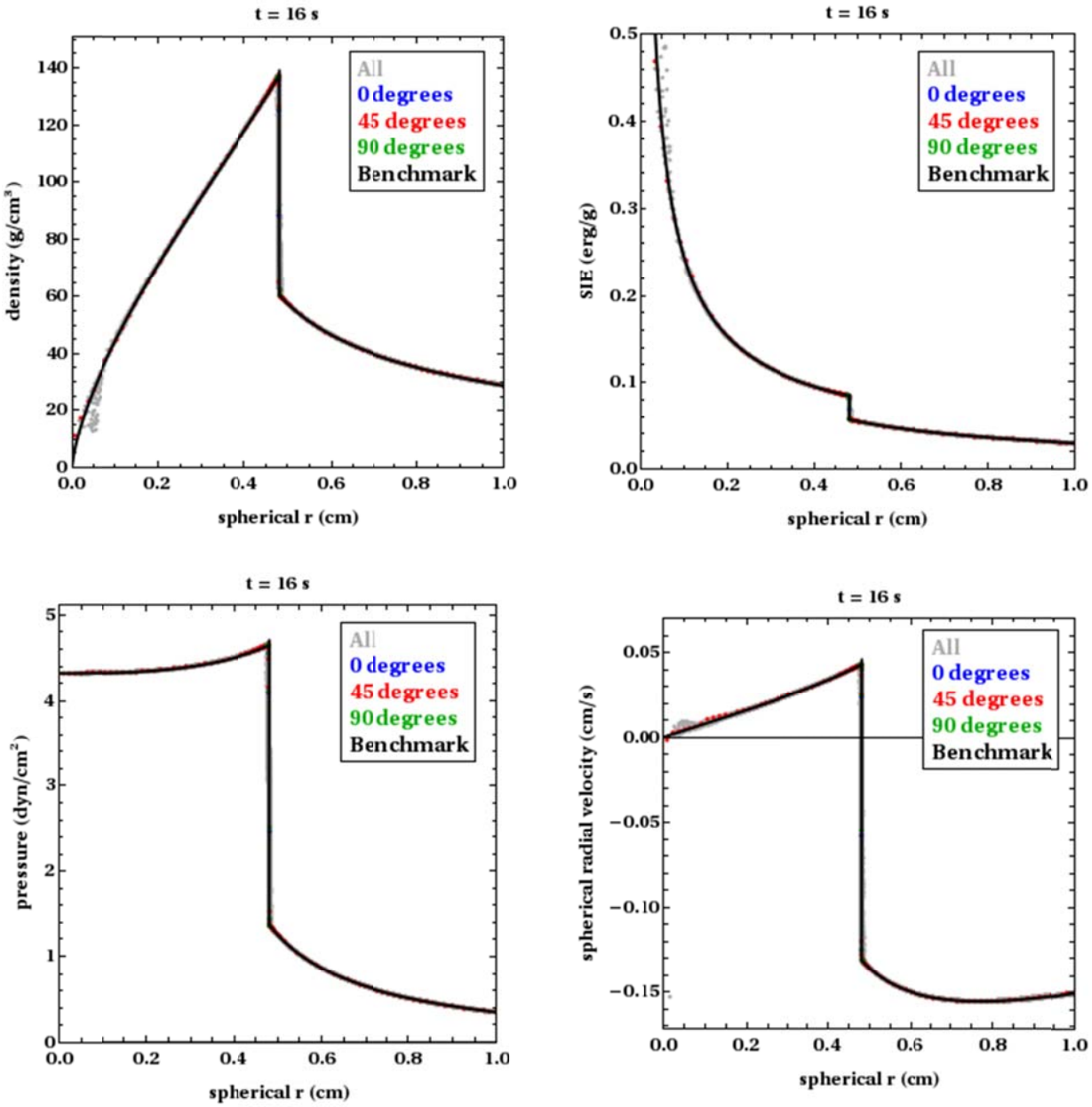

Figure A.25: 2D axi-symmetric SGP line-out results for initial *dr* = *dz* = 0.01 cm at *t* = 16 s with AMR enabled.

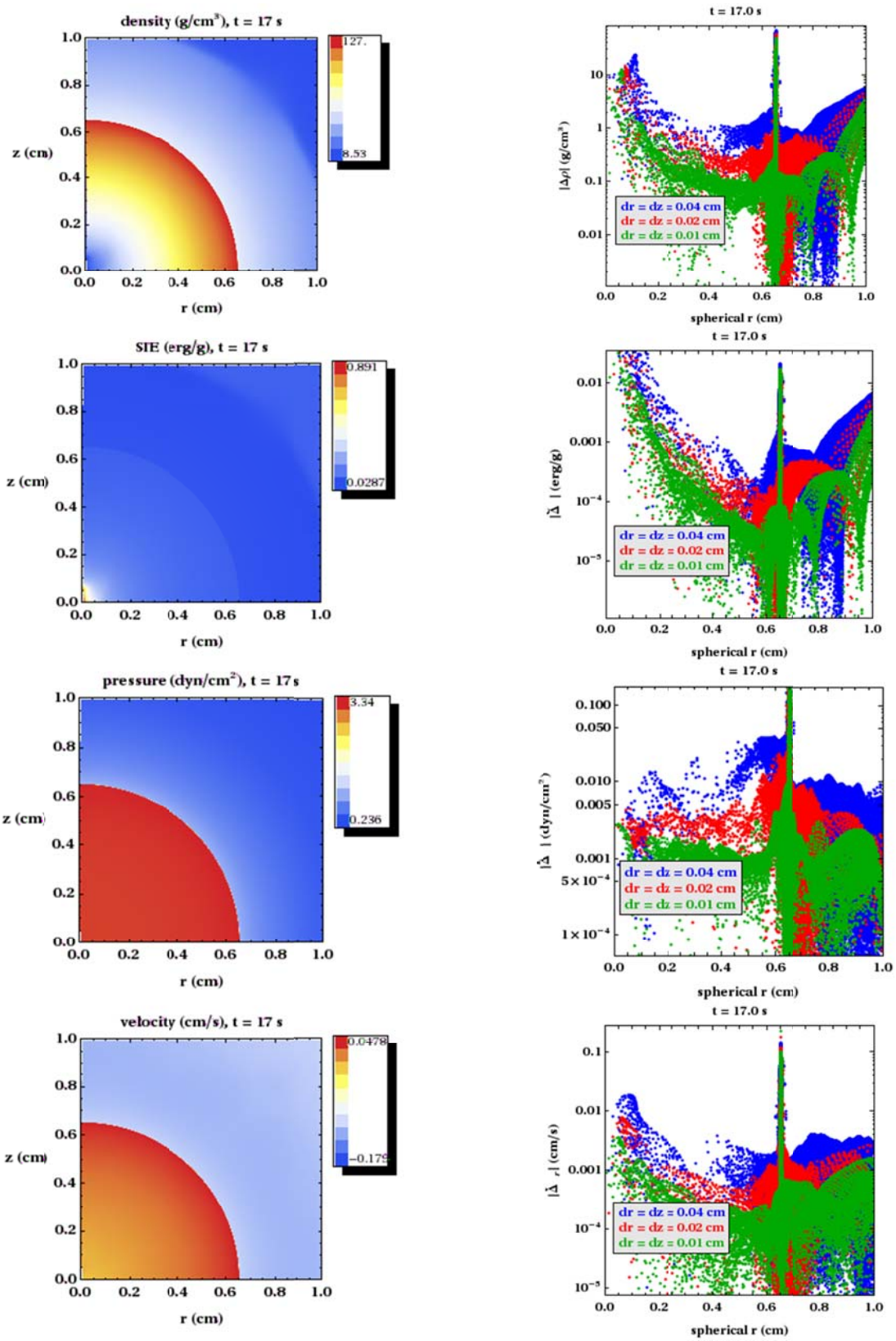

Figure A.26: Left – 2D axi-symmetric SGP results for initial *dr* = *dz* = 0.01 cm at *t* = 17 s with AMR enabled. Right – solution error on three initial different grids, calculated using Eq. (5).

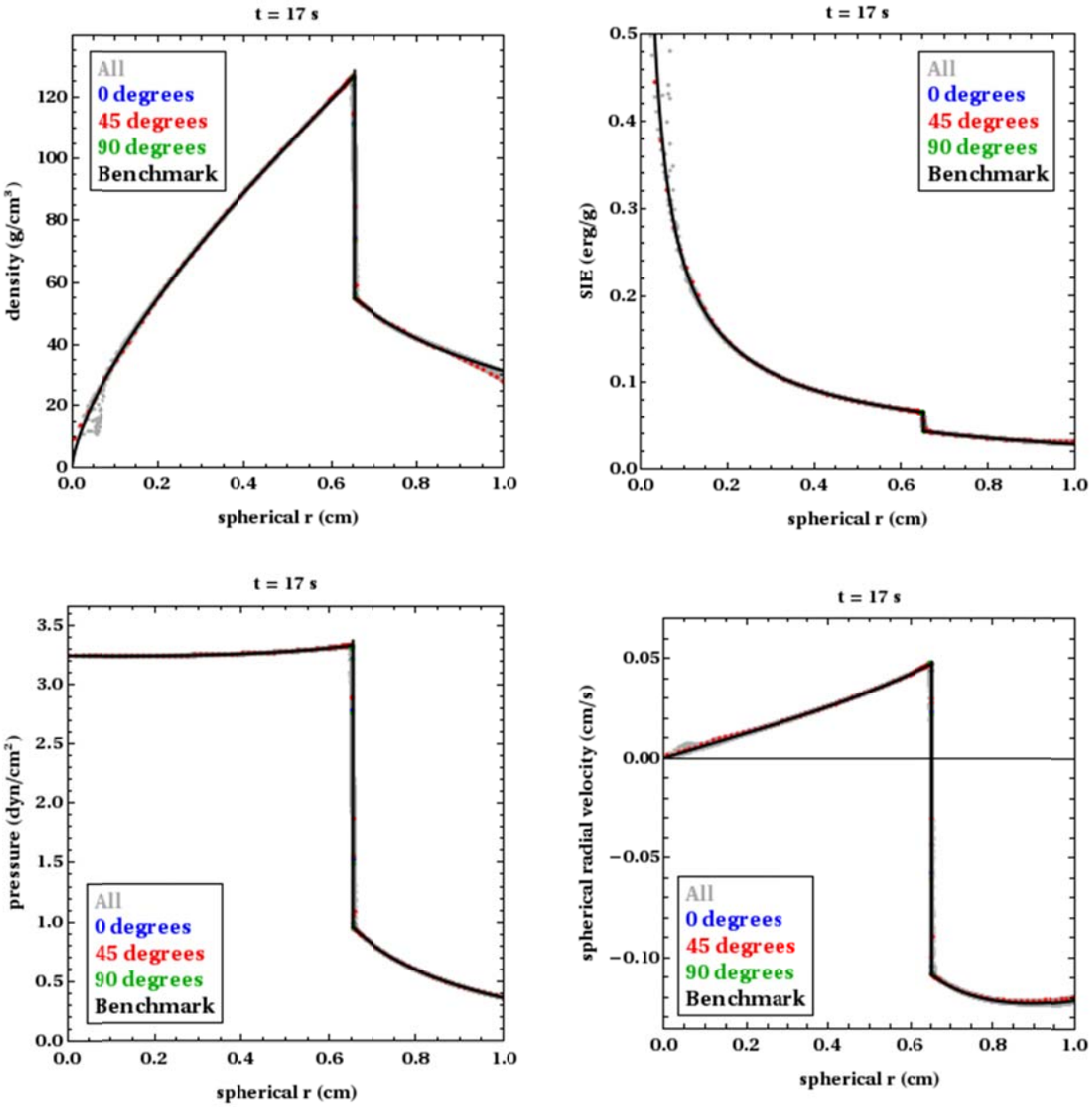

Figure A.27: 2D axi-symmetric SGP line-out results for initial *dr* = *dz* = 0.01 cm at *t* = 17 s with AMR enabled.

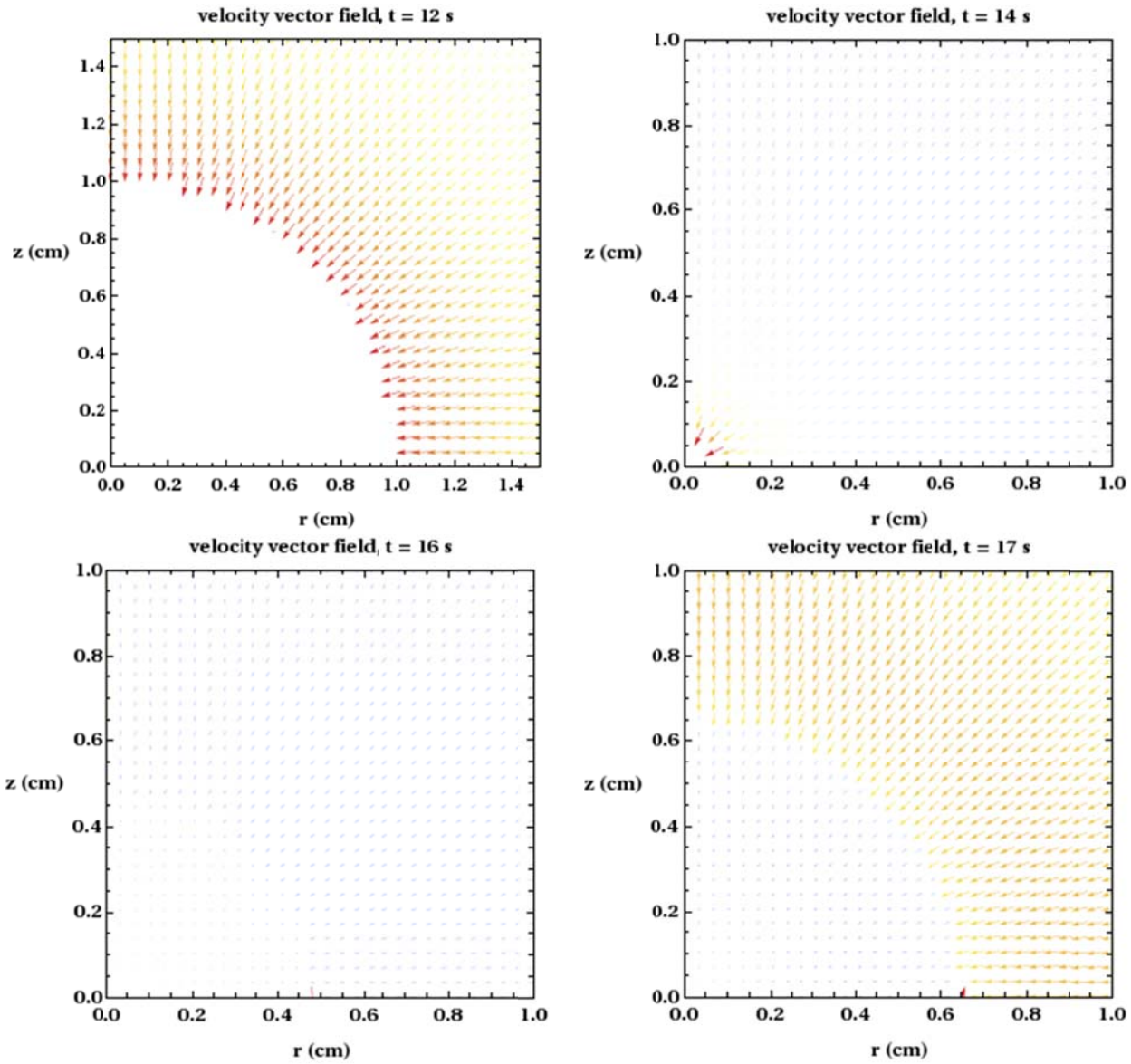

Figure A.28: Clockwise from top left – 2D axi-symmetric SGP velocity vector results for initial *dr* = *dz* = 0.01 cm at *t* = 12, 14, 16, and 17 s with AMR enabled.

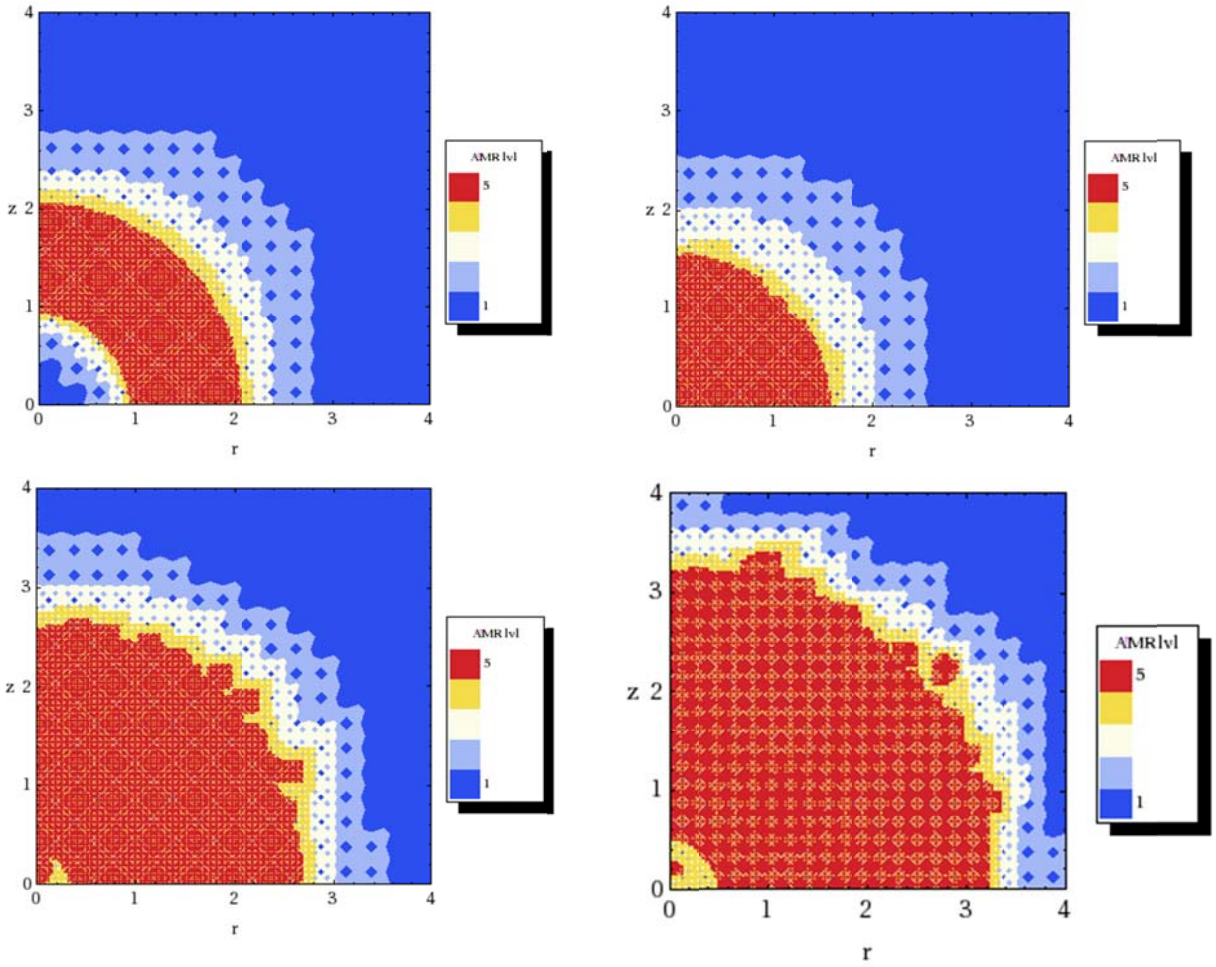

Figure A.29: Clockwise from top left – 2D axi-symmetric SGP AMR level results for initial *dr* = *dz* = 0.01 cm at *t* = 12, 14, 16, and 17 s.

A.6. 2D Axi-Symmetry, Simulation Comparison Metrics

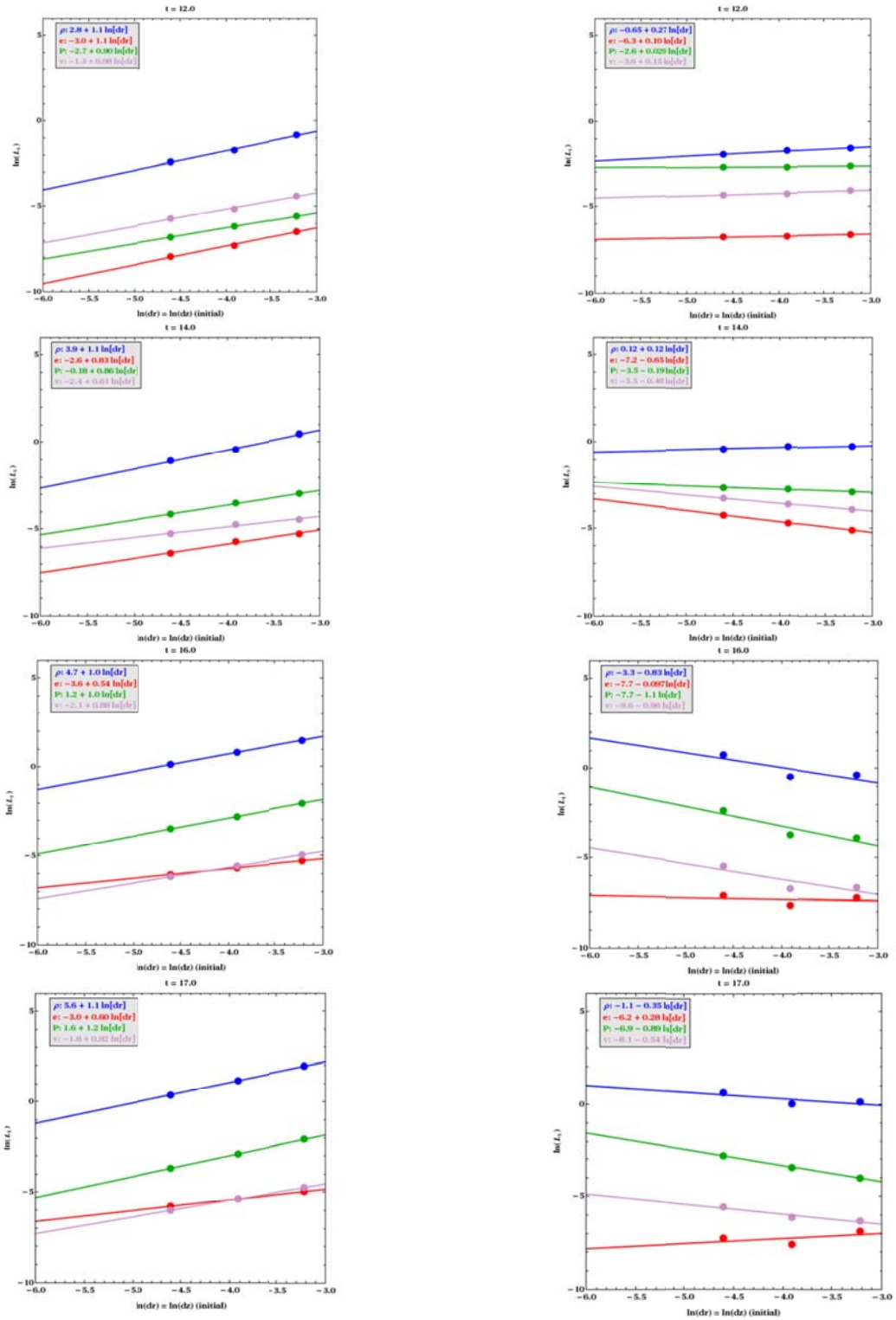

Figure A.30: Top to bottom – L_1 norm spatial convergence curves for 2D axi-symmetric SGP at t = 12, 14, 16, and 17 s. Left: without AMR. Right: with AMR enabled.

APPENDIX B: EVALUATION OF VARIOUS xRAGE CODE SETTINGS

Two versions of the xRAGE code (v1009 and v1109) and a variety of code settings were used to generate the 1D spherical AMR results that appear in Sec. III.B.

B.1: The 'numfine' Option

Results similar to those presented in Sec. IV.A are provided in Figs. B.1-B.8 for two choices of the numfine parameter: `numfine` = 1 and `numfine` = 5. The `numfine` = 5 results correspond to a 'smoother' contact profile at initialization (see Fig. 7) than otherwise used throughout the entirety of this report.

Figures B.1-B.4 exemplify the effect of the two different `numfine` settings on the structure of the converging shock wave. The density, SIE, and pressure results appear largely invariant with respect to the selected settings. Some differences are evident in the velocity results, however: Figs. B.1 and B.4 most readily show that the `numfine` = 5 case exhibits both fewer and less pronounced irregularities in the converging shock structure.

Figures B.5-B.8 exemplify the effect of the two different `numfine` settings on the structure of the reflected shock wave. The density, SIE, and pressure results again appear to be largely invariant with respect to the selected settings. Differences are again evident in the velocity results: Figs. B.5 and B.8 show that the `numfine` = 5 results are again subject to less irregularity in the vicinity of the reflected shock wave, but in this case a localized 'hot spot' of increased velocity is evident within the solution field.

A full assessment of the `numfine` parameter's influence on the SGP solution and its convergence properties at additional times will be reserved for a future study.

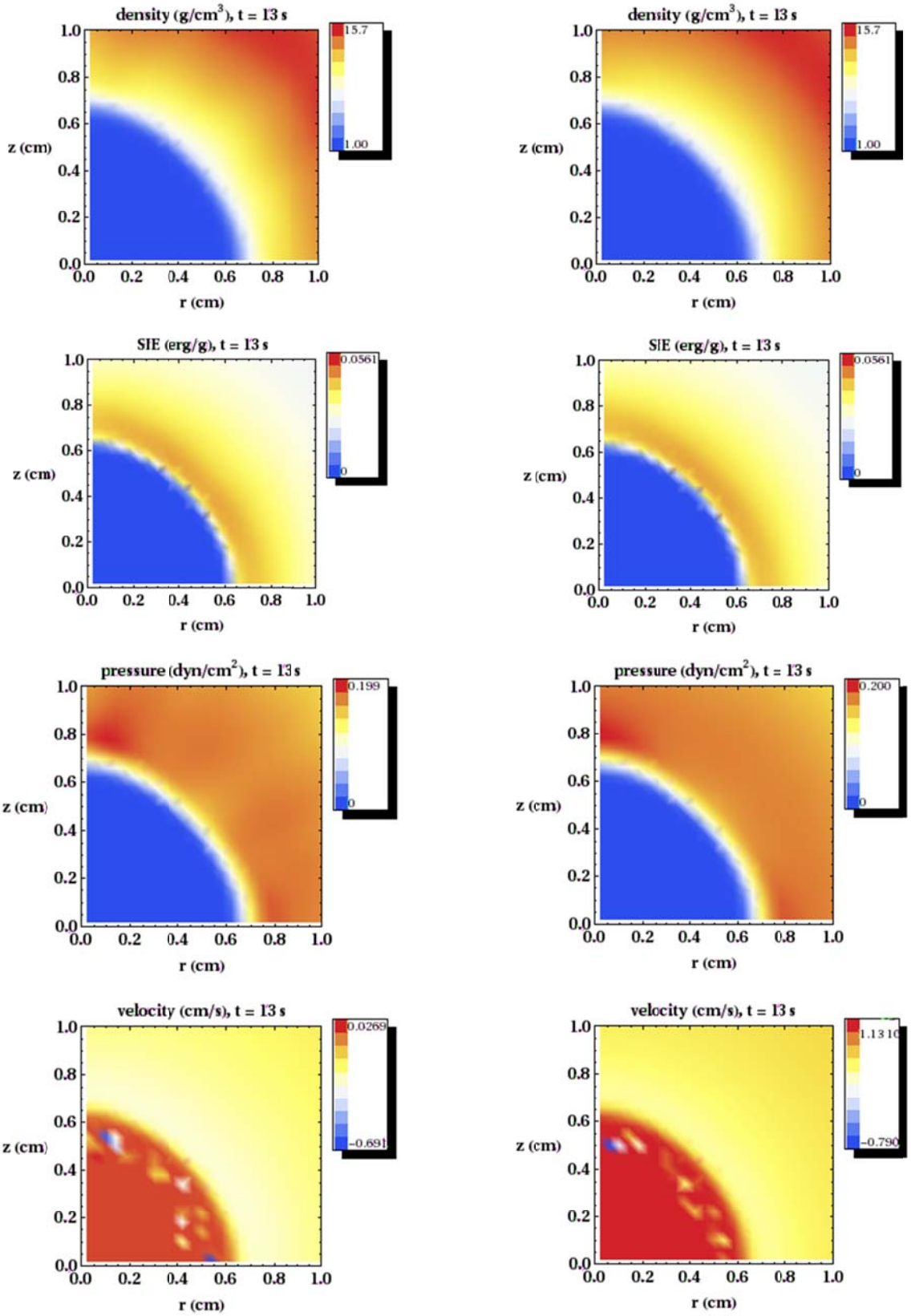

Figure B.1: 2D axi-symmetric SGP results for initial *dr* = *dz* = 0.04 cm at *t* = 13 s (converging flow). Left – `numfine` = 1, right – `numfine` = 5.

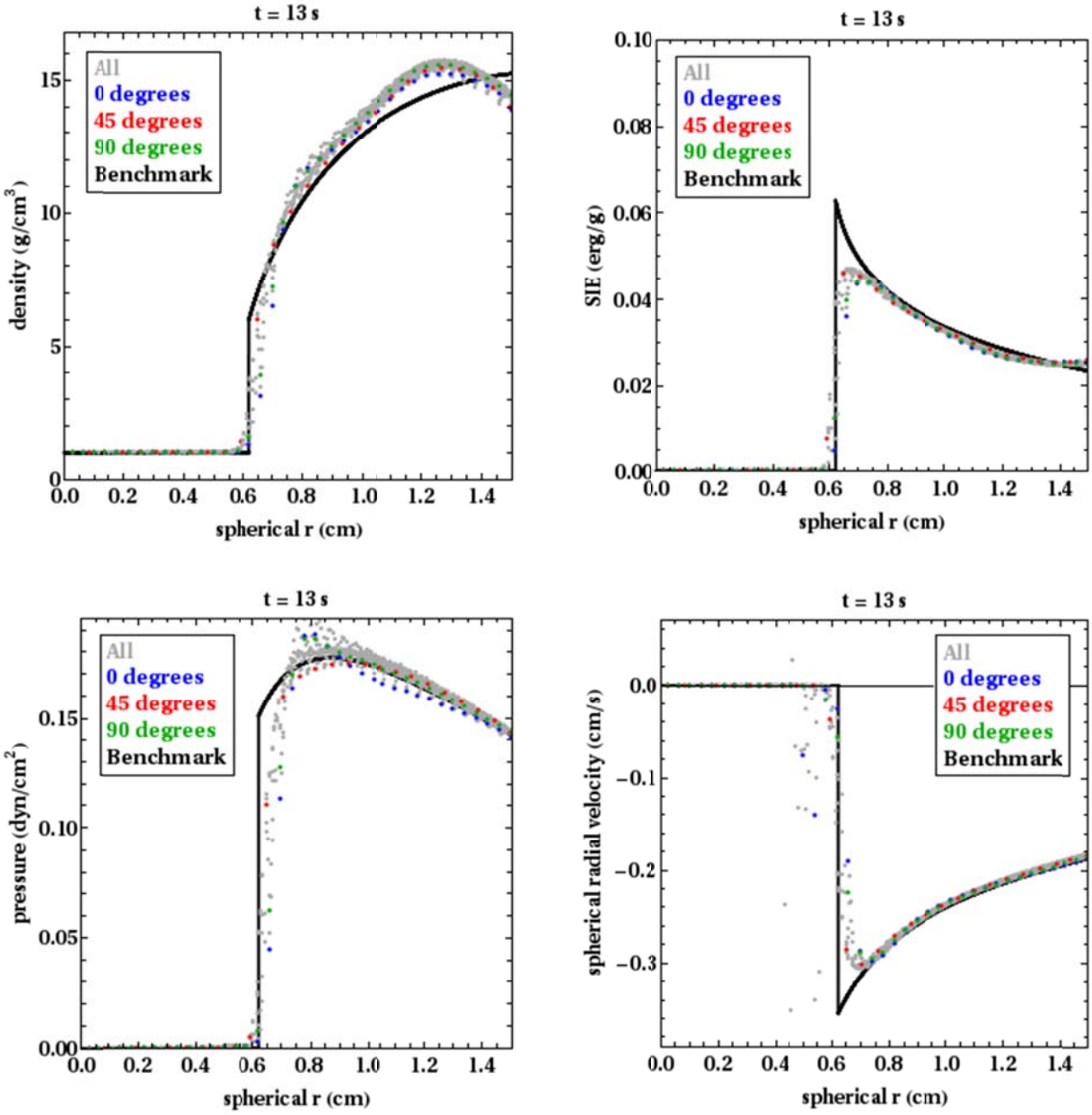

Figure B.2: 2D axi-symmetric SGP line-out results for *dr* = *dz* = 0.04 cm at *t* = 13 s (converging flow), `numfine` = 1.

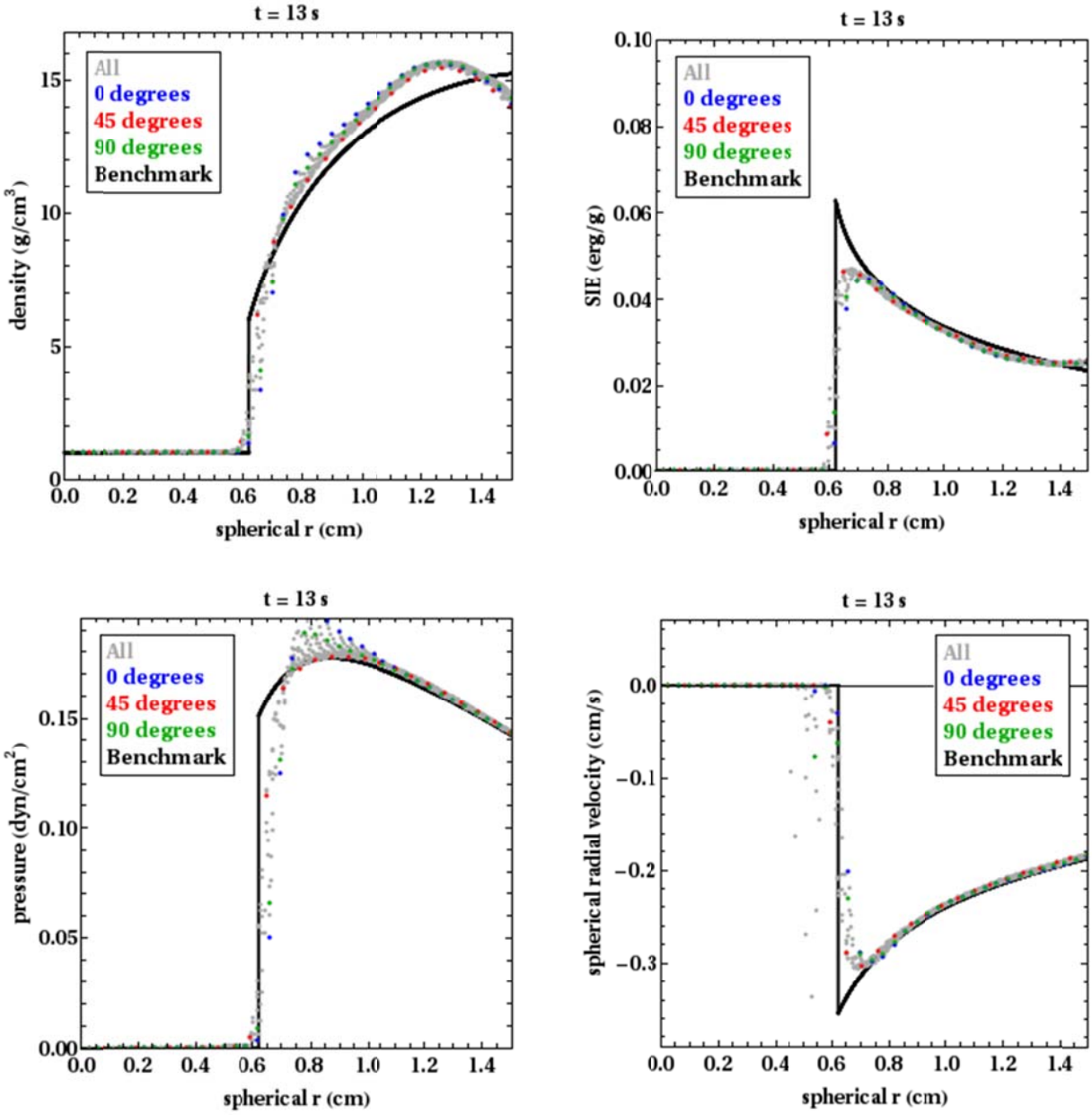

Figure B.3: 2D axi-symmetric SGP line-out results for *dr* = *dz* = 0.04 cm at *t* = 13 s (converging flow), `numfine` = 5.

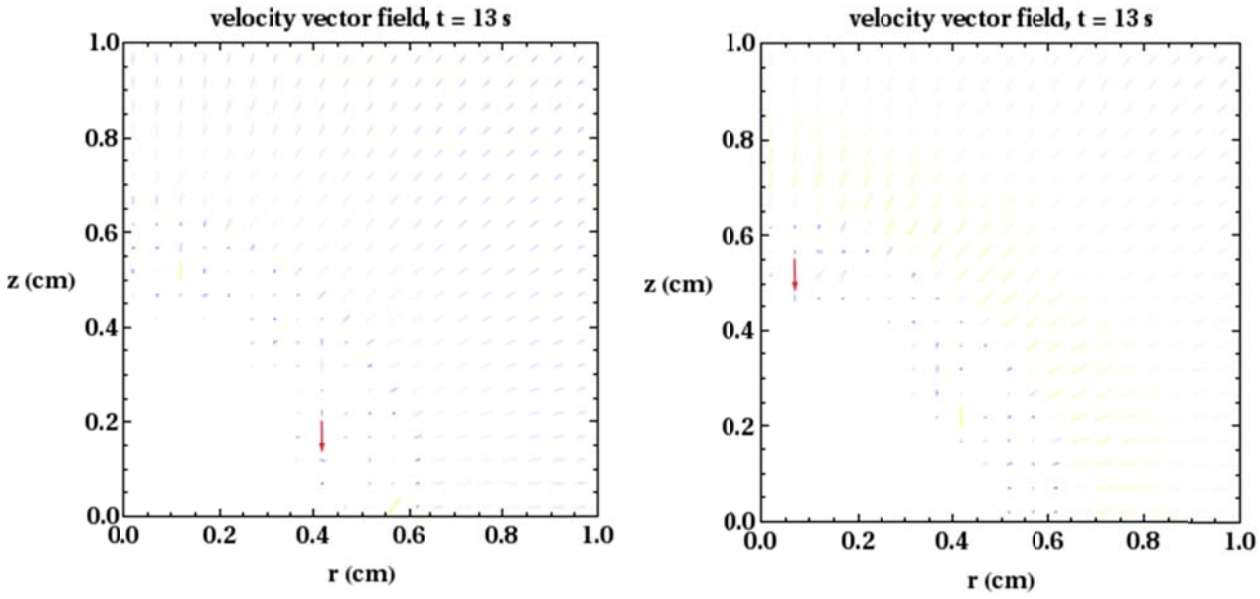

Figure B.4: 2D axi-symmetric SGP velocity vector results for initial *dr* = *dz* = 0.04 cm at *t* = 13 s (converging flow). Left – `numfine` = 1, right – `numfine` = 5.

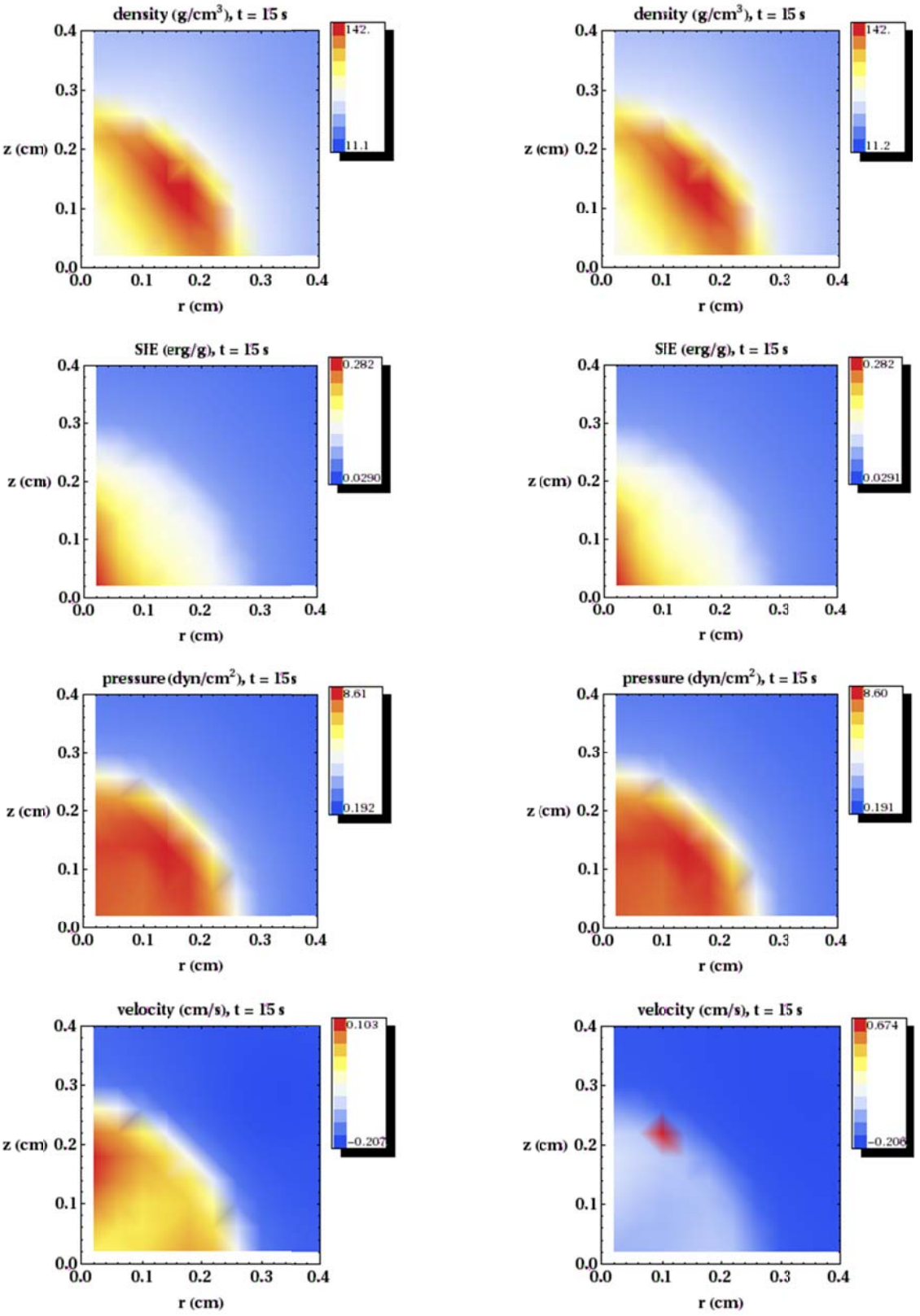

Figure B.5: 2D axi-symmetric SGP results for initial *dr* = *dz* = 0.04 cm at *t* = 15 s (diverging flow). Left – `numfine` = 1, right – `numfine` = 5.

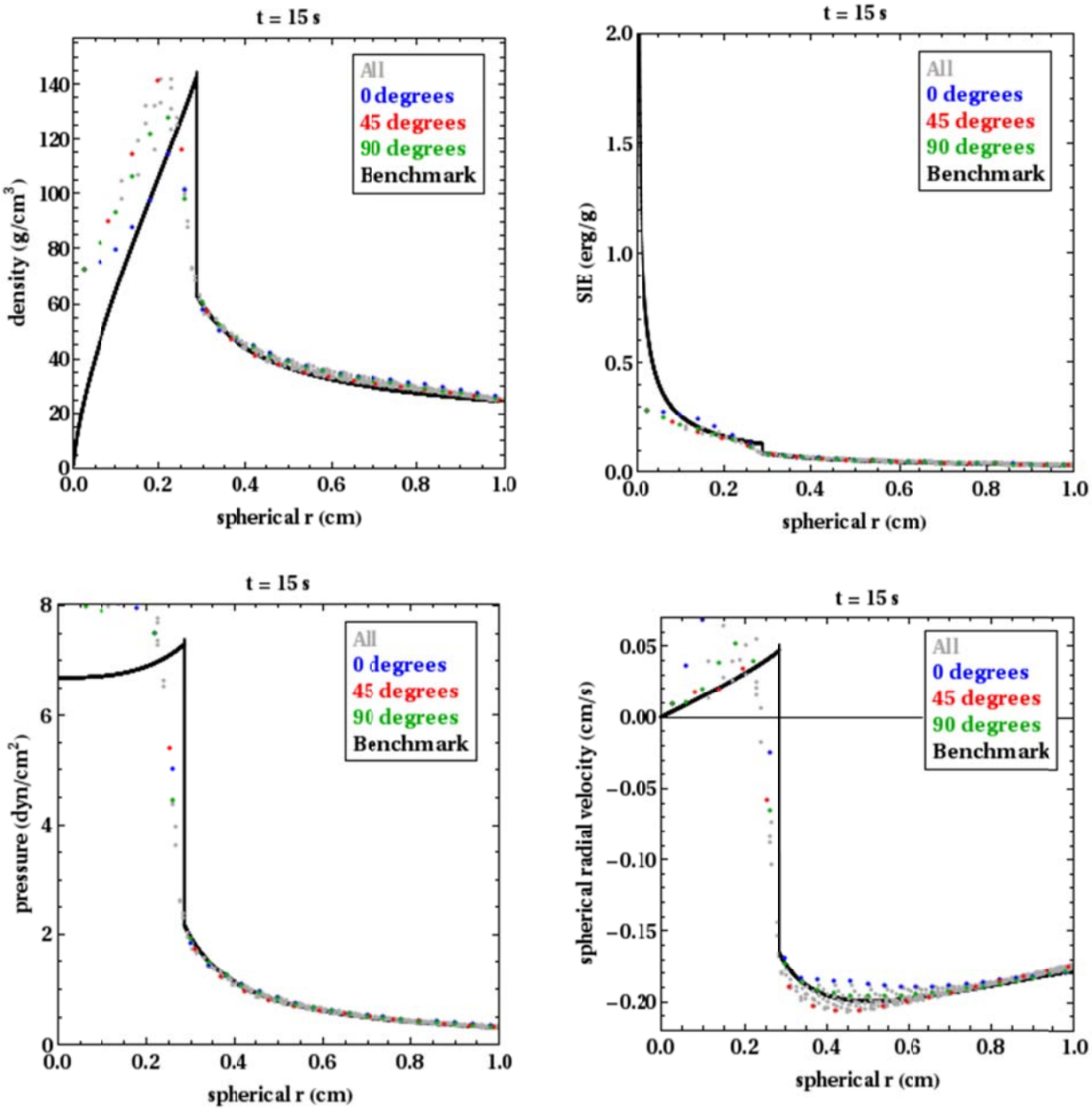

Figure B.6: 2D axi-symmetric SGP line-out results for *dr* = *dz* = 0.04 cm at *t* = 15 s (diverging flow), `numfine` = 1.

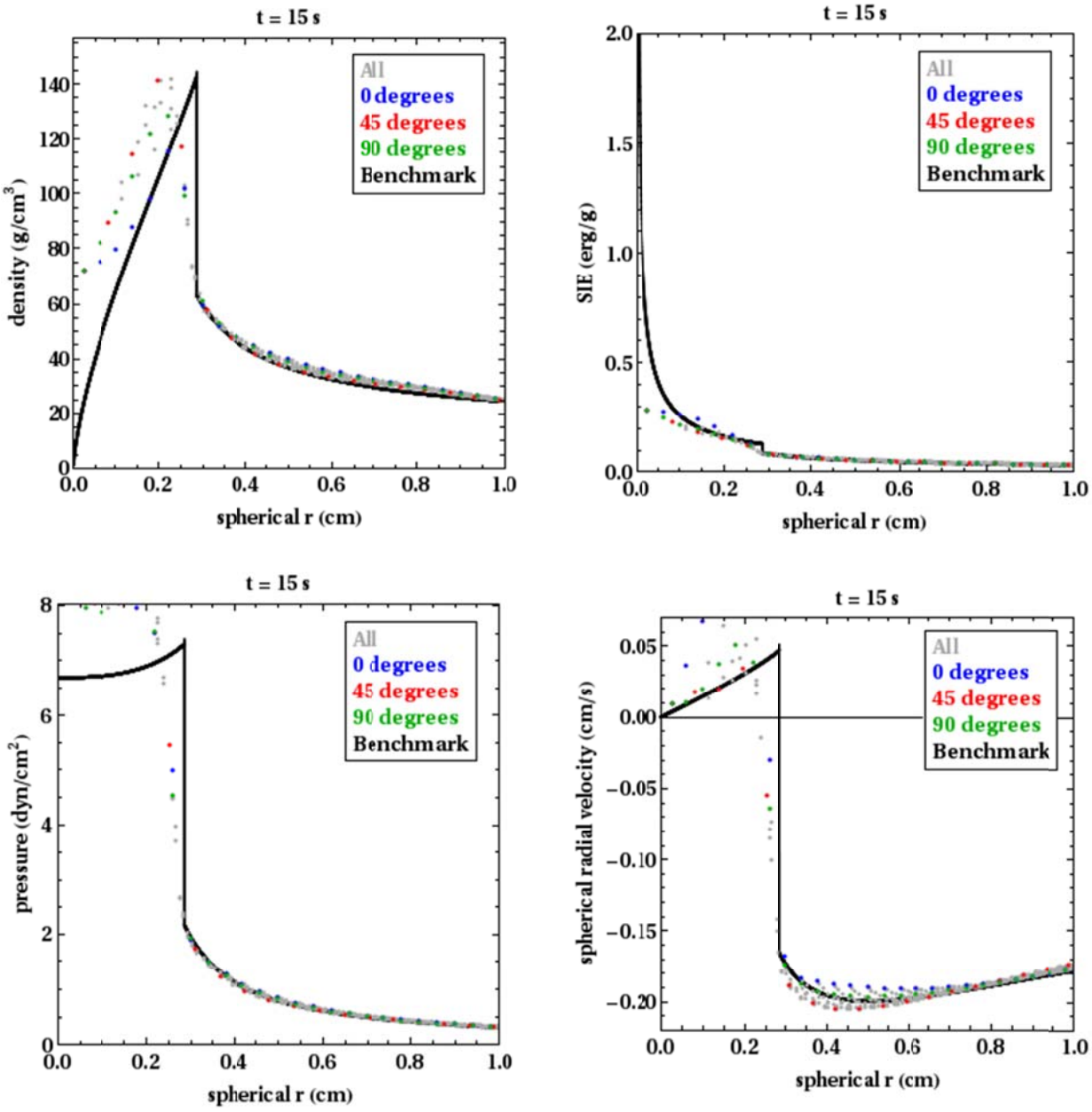

Figure B.7: 2D axi-symmetric SGP line-out results for *dr* = *dz* = 0.04 cm at *t* = 15 s (diverging flow), `numfine` = 5.

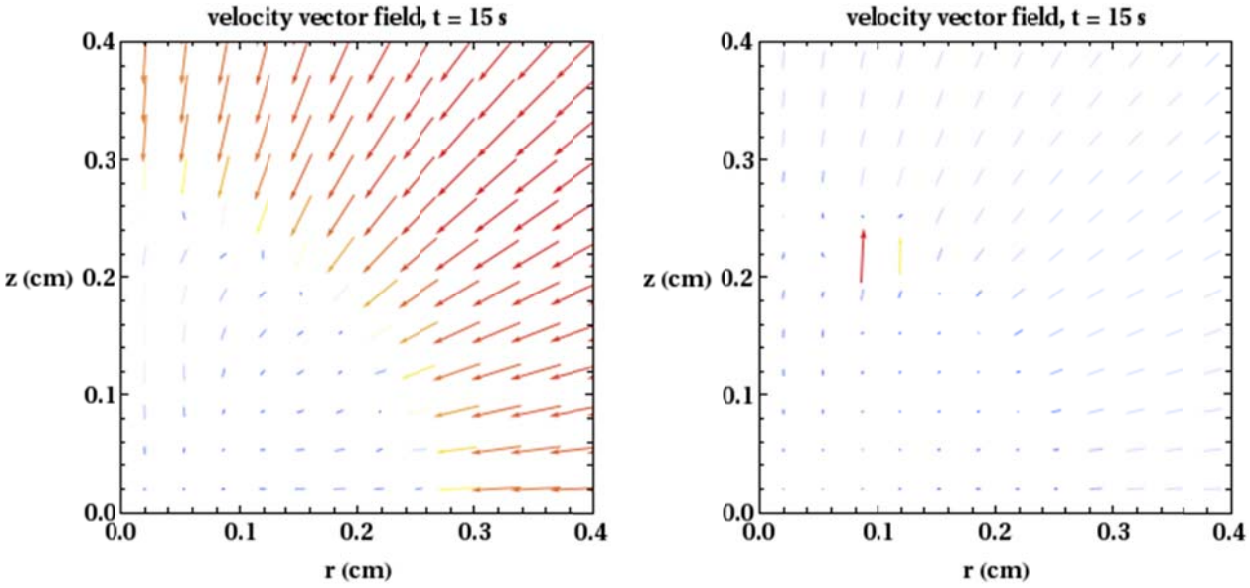

Figure B.8: 2D axi-symmetric SGP velocity vector results for initial *dr* = *dz* = 0.04 cm at *t* = 15 s (diverging flow). Left – `numfine` = 1, right – `numfine` = 5.

B.2: '`rpfix`' and '`enforce_tiny_cutoff`' Options

xRAGE contains three options that alter the way the code's Riemann solver operates[13]. These options, `rpfix`, `rpfix1`, and `rpfix2`, address various solution inaccuracies (e.g., the choice of units used in the Riemann solver, which may not be the same as the default code units). Furthermore, the `enforce_tiny_cutoff` option allows a user to adjust the code's numerical floor setting closer to zero, effectively preventing it from truncating small numbers. Each of these four options are true/false flags.

Figure B.9 shows the results of enabling the three `rpfix` flags in a 1D spherical AMR simulation (Sec. III.B settings), using xRAGE v1009.02 (the `enforce_tiny_cutoff` option is not available in this version of the code). Additional results using other combinations of the flags do not appear to be as effective in reducing the near-origin oscillation at *t* = 15 s.

Figure B.9 shows that the use of all `rpfix` options reduces but does not eliminate the oscillation error.

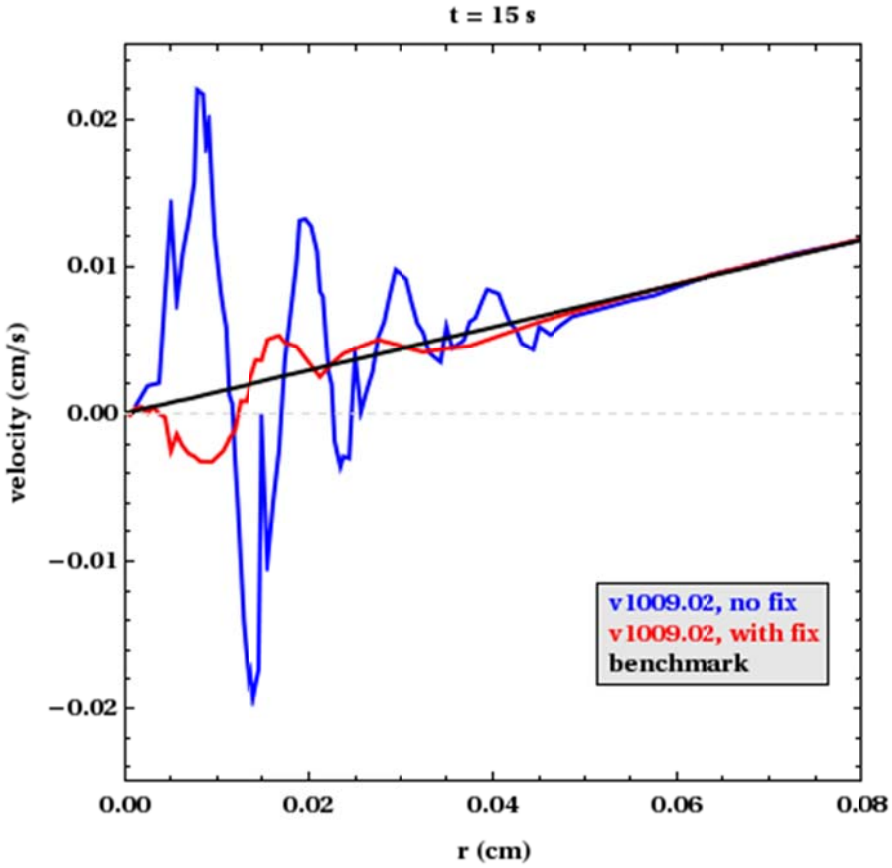

Figure B.9: 1D spherical SGP velocity results at *t* = 15 s (diverging flow), with AMR enabled and all `rpfix` features enabled.

B.3: xRAGE v1009 and v1109

In the xRAGE v1109 release notes[17], it is stated that a 'bug fix' pertaining to 'recon' (i.e., the AMR package) was implemented:

> "Fixed a bug in recon where the energy values for new cells were not computed and filled in. Energy values are used to compute state data for new cells, so problems using AMR could see differences."

Figure B.10 shows the difference between identical simulations run with xRAGE v1009.02 and v1109.02.

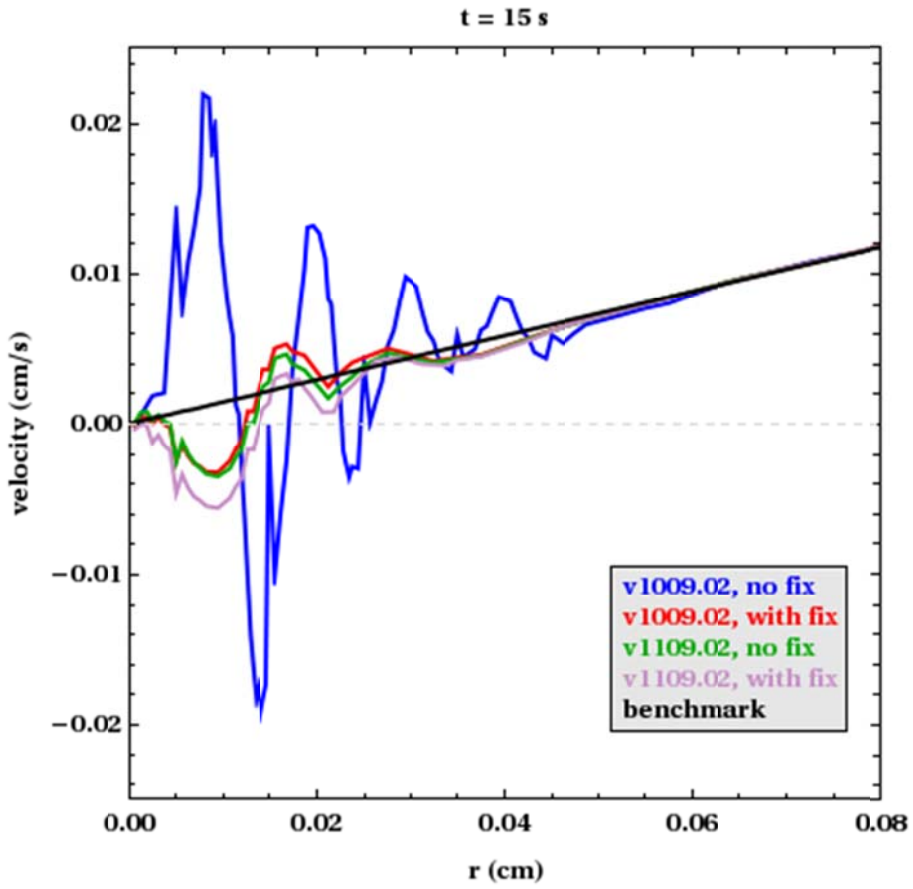

Figure B.10: 1D spherical SGP velocity results at *t* = 15 s (diverging flow), with AMR enabled.

Figure B.10 shows that the reconstruction update implemented as part of v1109 significantly reduces the oscillation error, even without additional flags activated. Figure B.10 also shows that activating the same 'optimal' combination of `rpfix` and `enforce_tiny_cutoff` flags as considered in Sec. A.1 results in the slight regrowth of the oscillation error. It is therefore recommended that xRAGE v1109 (or later) be used for 1D spherical AMR simulations, but without any additional flags activated (as has been done throughout the preceding study).

APPENDIX C: CYLINDRICAL GUDERLEY PROBLEM WITH 2D AXI-SYMMETRY

Recently, an informal series of cylindrical Guderley calculations was performed in xRAGE (v1109.02) in 2D axi-symmetric geometry, on a square, uniform grid. Setup for these calculations is relatively simple and follows essentially the same procedure outlined by Ramsey, et al.[6] for 1D calculations.

Under 2D axi-symmetry, any cylindrical Guderley solution is invariant with respect to the z-direction, and is initialized with r-dependence only, as shown for $\gamma = 1.4$ in Fig. C.1, over the domain $r = (0,4)$ and $z = (0,4)$ cm. For this simulation, the following code options were used but are not necessarily unique:

- Code default units (cgs)
- Specific heat $c_v = 1.0$ erg/(g-eV), so temperature and SIE are equivalent
- Adaptive time step
- Stop time = 2.0 s
- Boundary condition at $r = 0$ cm: code default (symmetric/reflective BC)
- Boundary condition at $r = 4$ cm: code default (reflective BC[13])
- Boundary condition at $z = 0$ cm: code default (rigid wall BC)
- Boundary condition at $z = 4$ cm: code default (reflective BC)
- Initial uniform grid spacing $dx = dy = 0.04$ cm
- Benchmark solution: 1D cylindrical SGP with $dr = 0.001$ cm

This initialization corresponds to convergent flow with the shock located at $r = 1.0$ at $t = 0.0$, and zone initializations using point-wise Guderley solution values of density, SIE, and velocity evaluated at the zone centers (as opposed to cell-averaged initialization using conserved quantities, as discussed at length by Ramsey, et al.[6]).

As the simulation proceeds, the Guderley converging shock proceeds symmetrically in the r-direction; in effect, as if the z-dependence is not included. The converging shock reflects off the entire length of the z-axis at $t = 1.0$, and a symmetric reflected shock forms and propagates outward.

As observed in 1D spherical simulations by Ramsey, et al.[6], the cylindrical calculations exhibit boundary rarefaction errors due to the selection of the xRAGE default boundary condition on the outer r-axis. No such rarefactions are evident on the problem's other boundaries, nor is any symmetry-breaking immediately evident at the selected times of interest.

Figures C.1-C.3 represent the extent to date under which the cylindrical Guderley problem has been investigated using 2D axi-symmetry. A more comprehensive investigation would by necessity involve an initialization using cell-averaged quantities, and perhaps involve quantitative comparison to 1D cylindrical results (e.g., convergence analyses). This effort will be reserved for a future study.

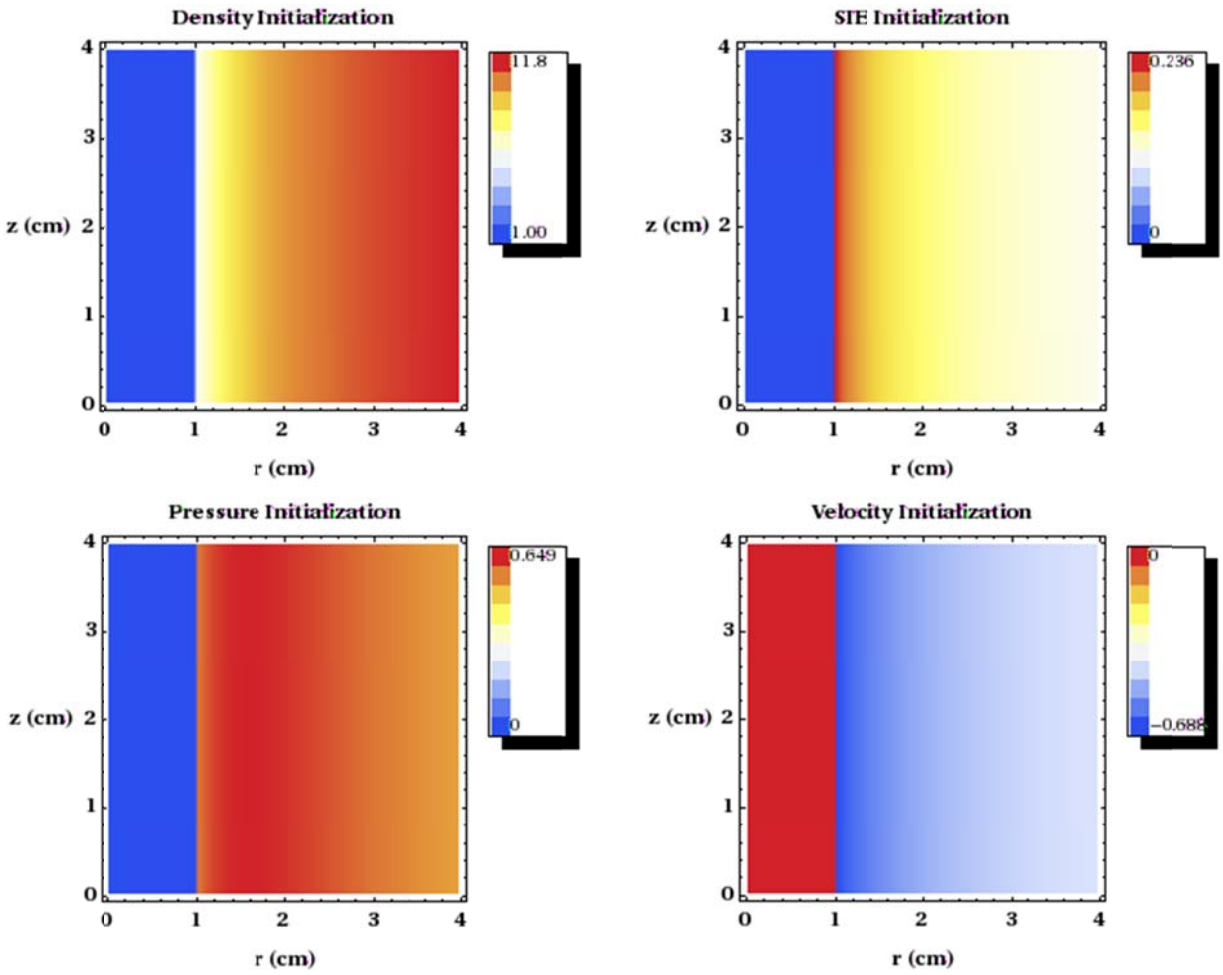

Figure C.1a: Initialization of a γ = 1.4 cylindrical Guderley solution in a 2D axi-symmetric grid.

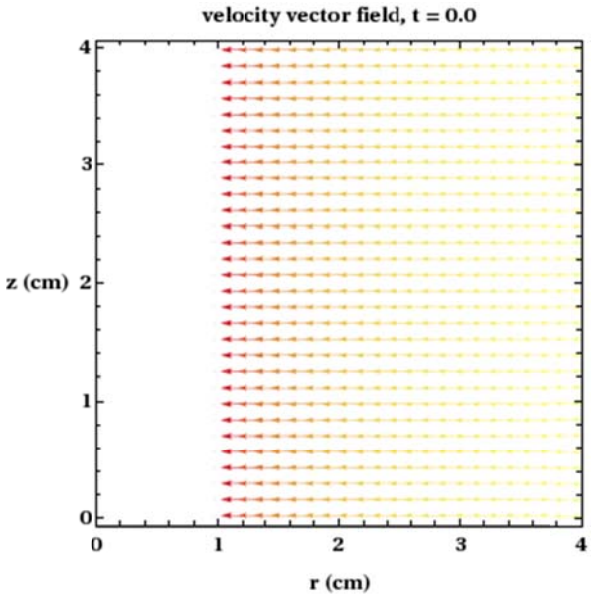

Fig. C.1b: Initialization of a γ = 1.4 cylindrical Guderley solution in a 2D axi-symmetric grid; velocity vectors.

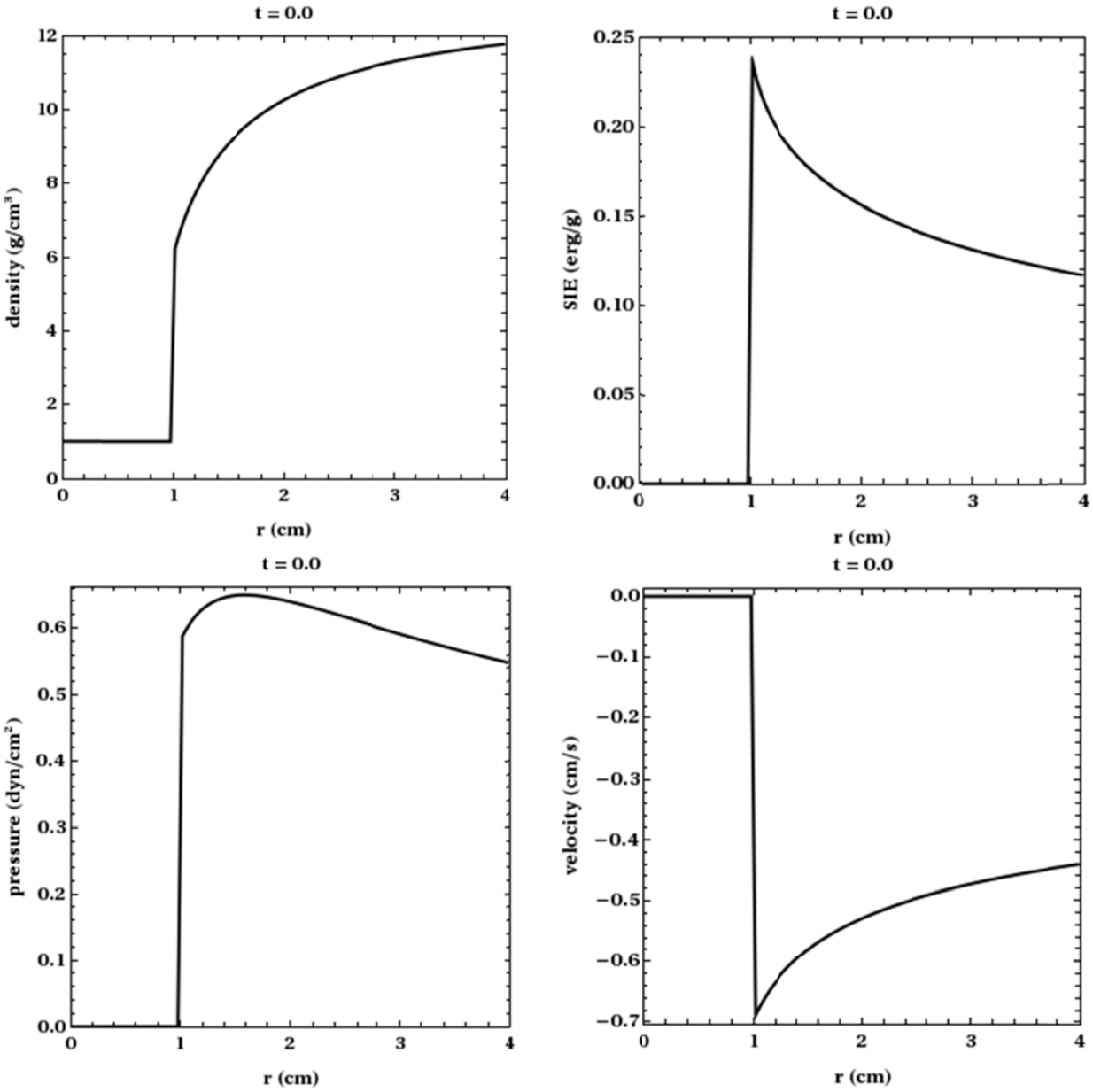

Figure C.1c: Initialization of a γ = 1.4 cylindrical Guderley solution in a 2D axi-symmetric grid; scatter plots.

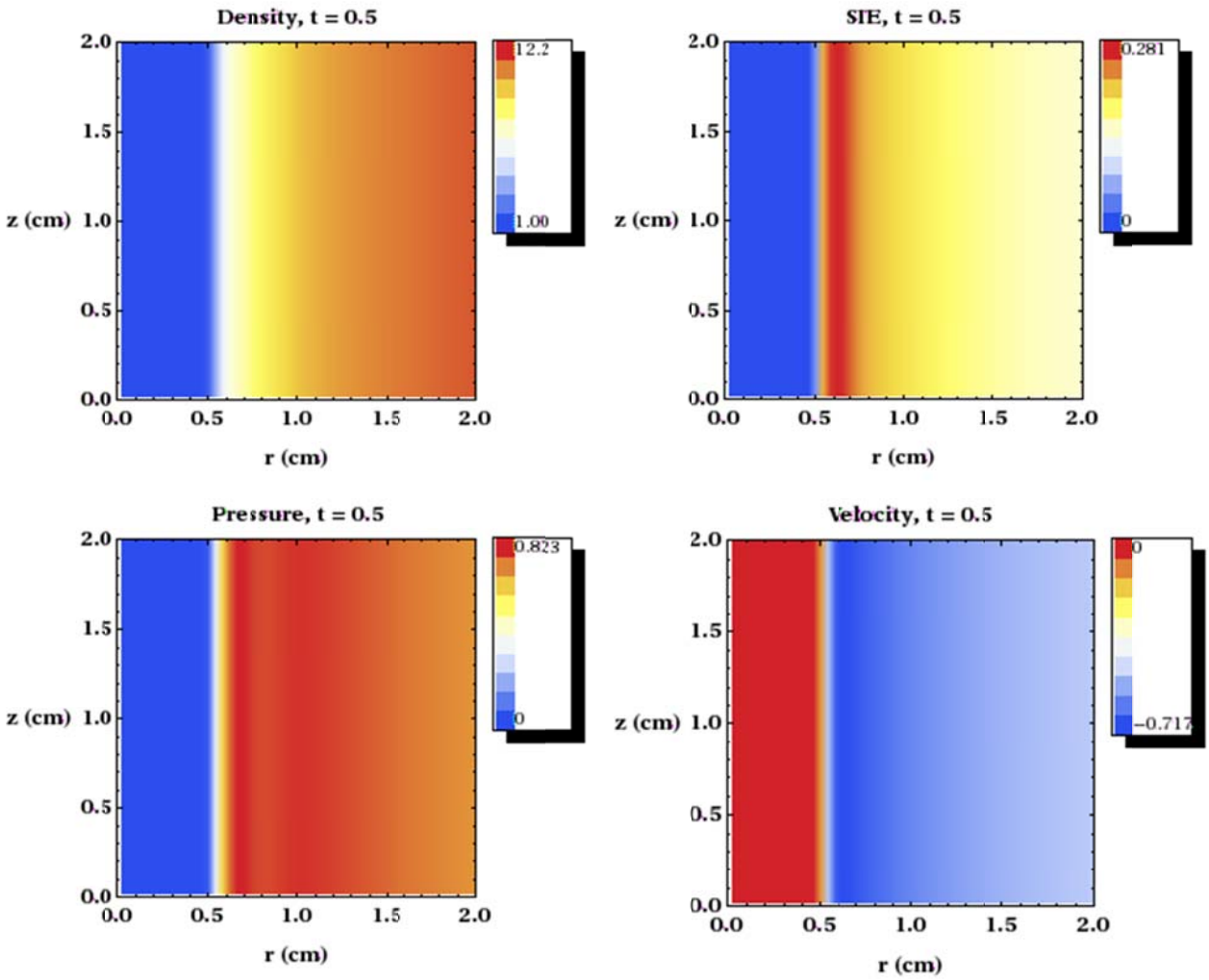

Figure C.2a: Evolution of Fig. C.1 initialization to *t* = 0.5 (converging flow).

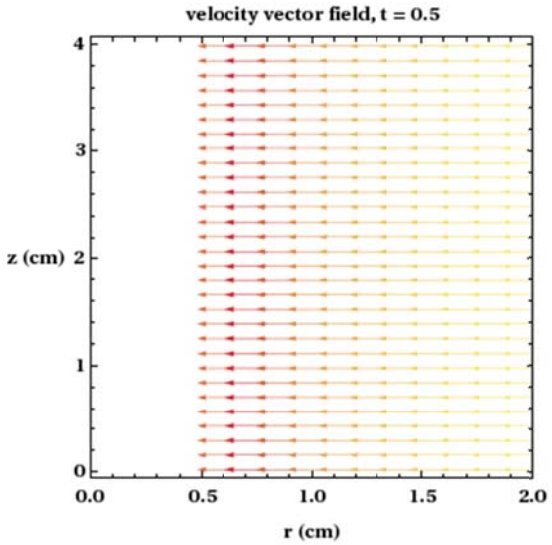

Fig C.2b: Evolution of Fig. C.1 initialization to *t* = 0.5 (converging flow); velocity vectors.

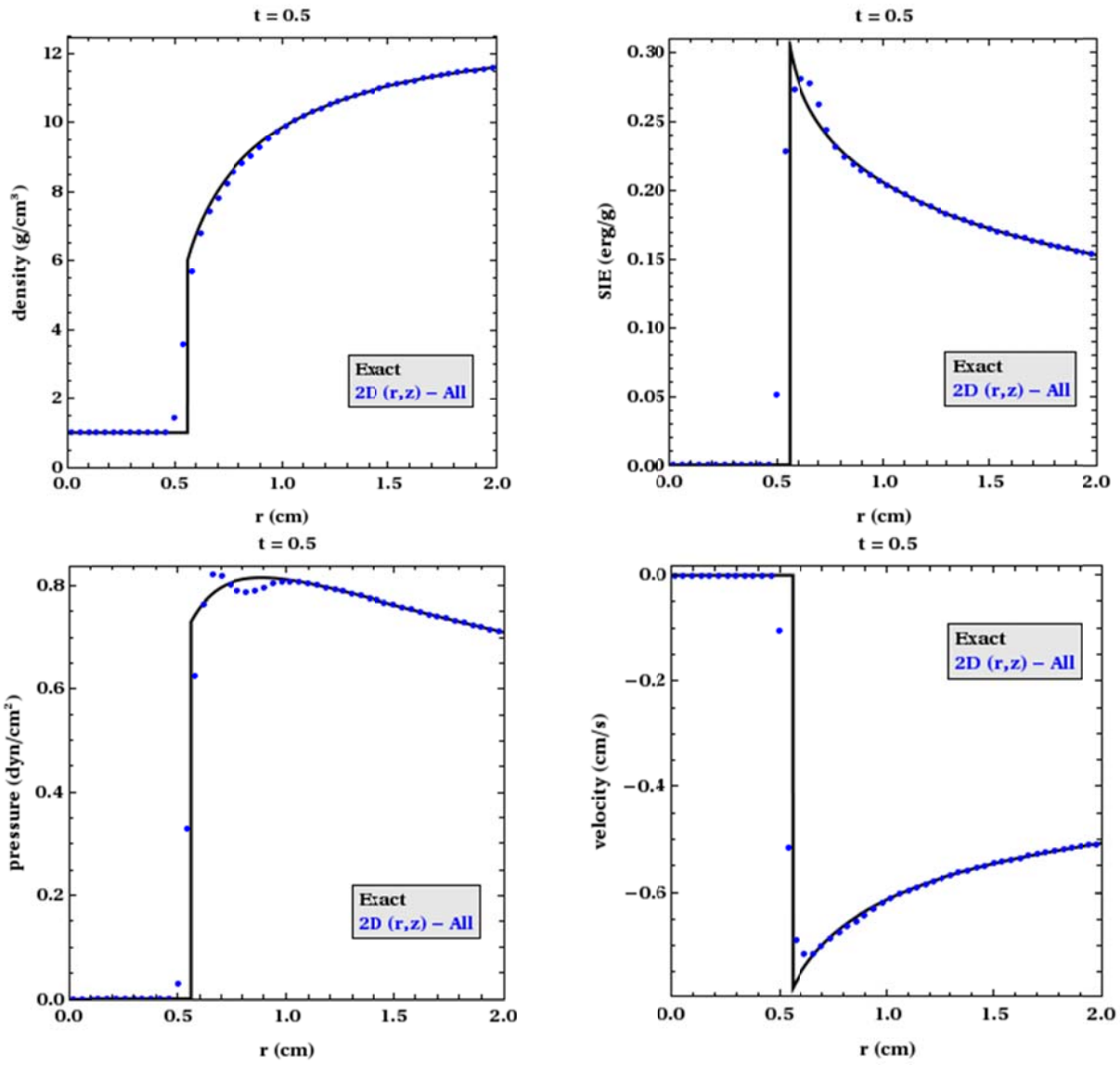

Figure C.2c: Evolution of Fig. C.1 initialization to t = 0.5 (converging flow); scatter plots.

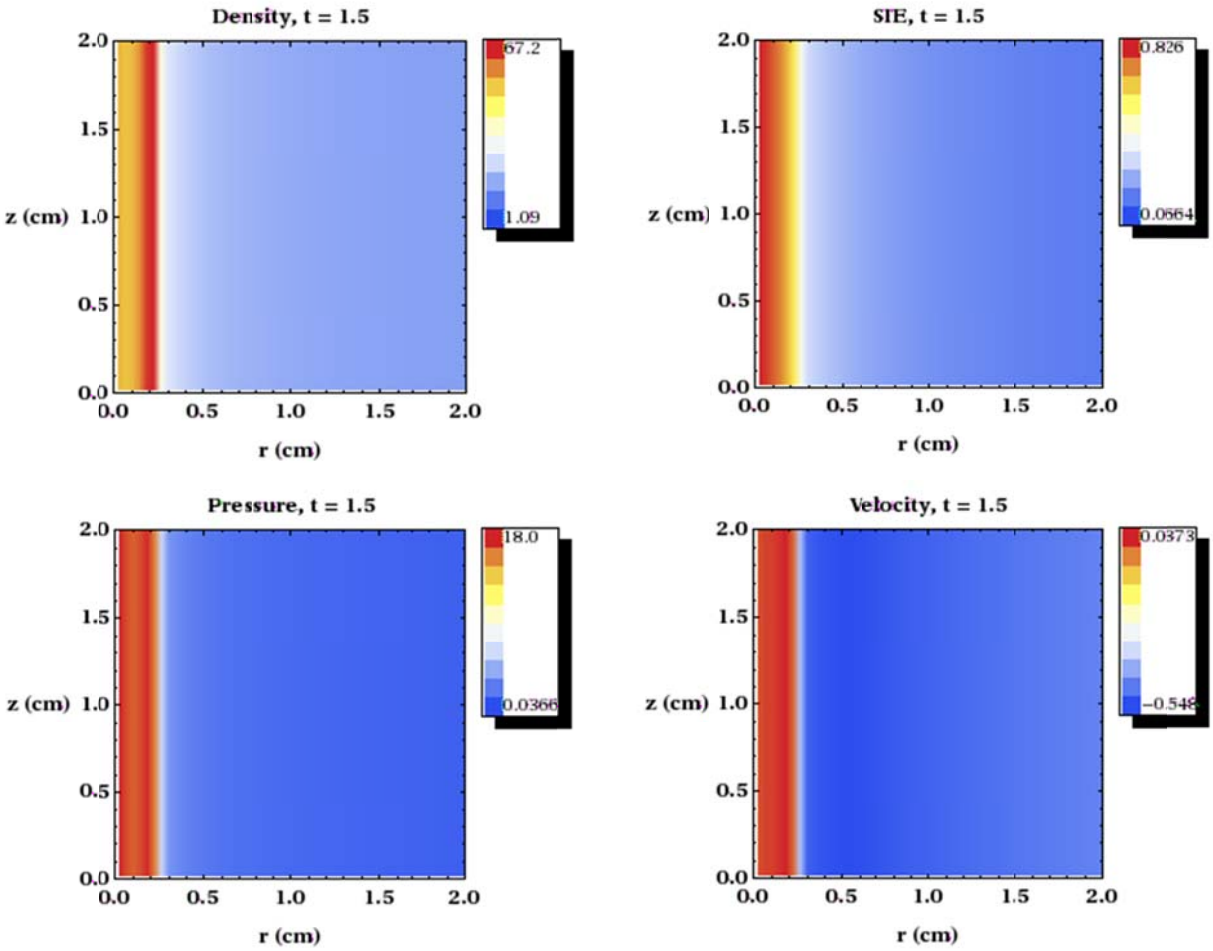

Figure C.3a: Evolution of Fig. C.1 initialization to *t* = 1.5 (diverging flow).

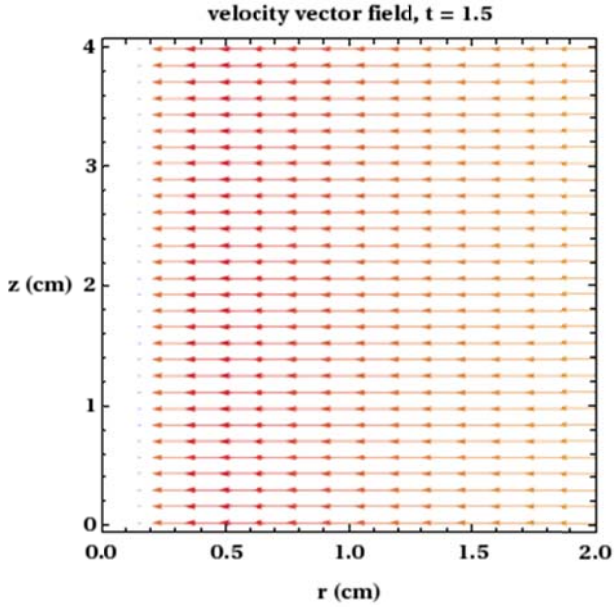

Fig. C.3c: Evolution of Fig. C.1 initialization to *t* = 1.5 (diverging flow); velocity vectors.

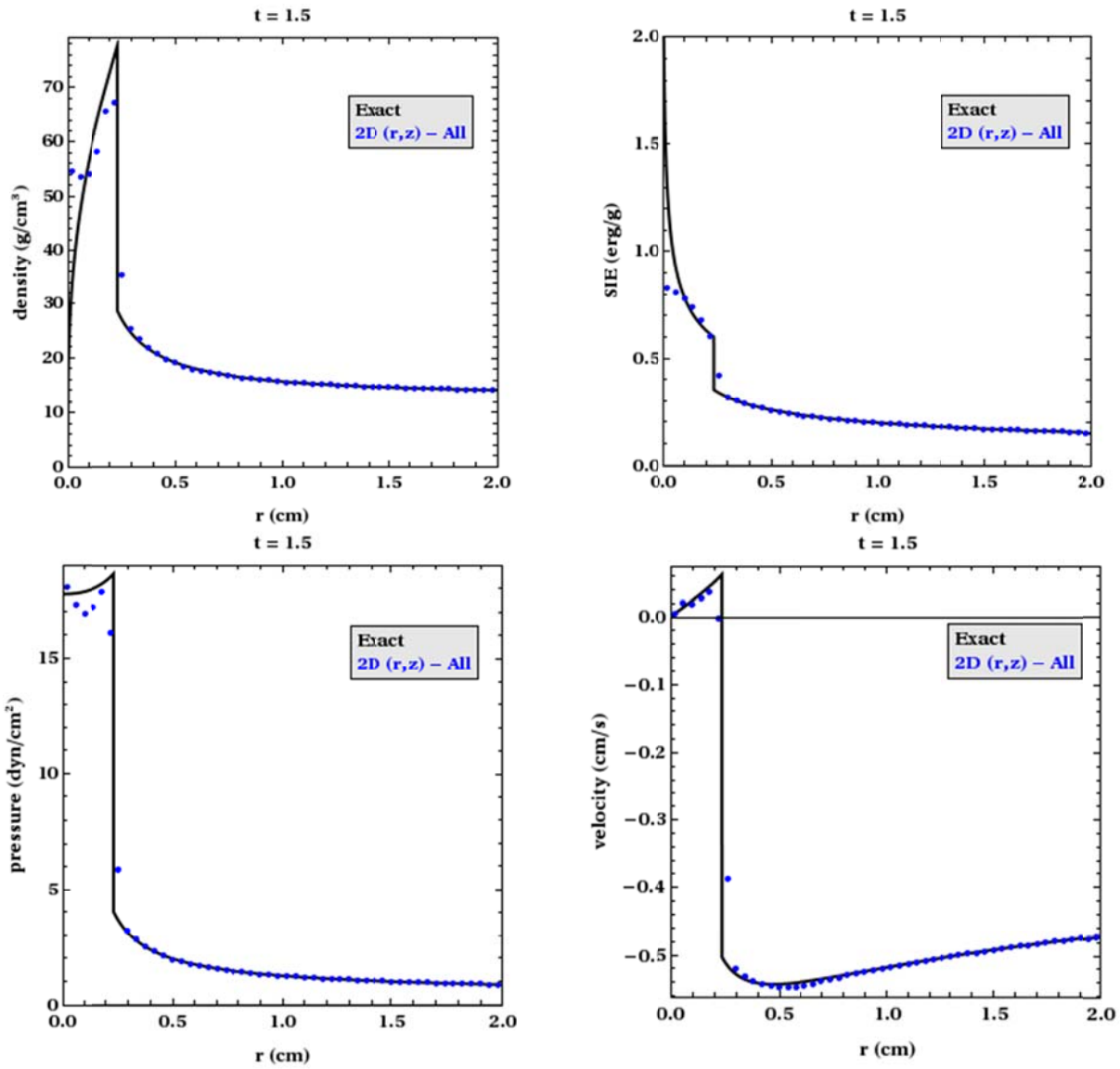

Figure C.3b: Evolution of Fig. C.1 initialization to *t* = 1.5 (diverging flow); scatter plots.

APPENDIX D: SURROGATE GUDERLEY PROBLEM FOR 2D CARTESIAN GEOMETRY

Constructing a 2D Cartesian SGP setup in xRAGE (v1109.02) is very similar to the 2D axi-symmetric case, and is intended to isolate asymmetric wall-heating in the divergent flow regime as an axi-symmetric phenomenon. For these simulations, the following code options were used but are not necessarily unique:

- Code default units (cgs)
- Specific heat c_v = 1.0 erg/(g-eV), so temperature and SIE are equivalent
- Adaptive time step
- Stop time = 30.0 s
- Boundary condition at x = 0 cm: code default (symmetric/reflective BC)
- Boundary condition at x = 10 cm: code default (reflective BC[13])
- Boundary condition at y = 0 cm: code default (rigid wall BC)
- Boundary condition at y = 10 cm: code default (reflective BC)
- Initial uniform grid spacing $dx = dy$ = 0.04 cm
- Benchmark solution: 1D cylindrical SGP with dr = 0.001 cm
- AMR settings (where applicable):
    - A maximum of 5 refinement levels are allowed
    - `pctdiv` = 0.001

The 2D Cartesian SGP is *not* otherwise identical to its 2D axi-symmetric counterpart: in the former problem shocks will not propagate as quickly in the absence of a curvilinear ordinate (and thus the increased stop time, as compared to the 1D spherical and 2D axi-symmetric cases). Even so, the 2D Cartesian SGP is useful for the intended purpose.

Initialization of the 2D Cartesian SGP on a square mesh with and without AMR is subject to the same xRAGE subtleties as discussed in Sec. IV.

D.1: Uniform Grid

Figures D.1-D.4 show selected converging regime (Figs. D.1 and D.3) and diverging regime (Figs. D.2 and D.4) results of a 2D Cartesian SGP calculation, intended only to address the asymmetric wall-heating phenomenon.

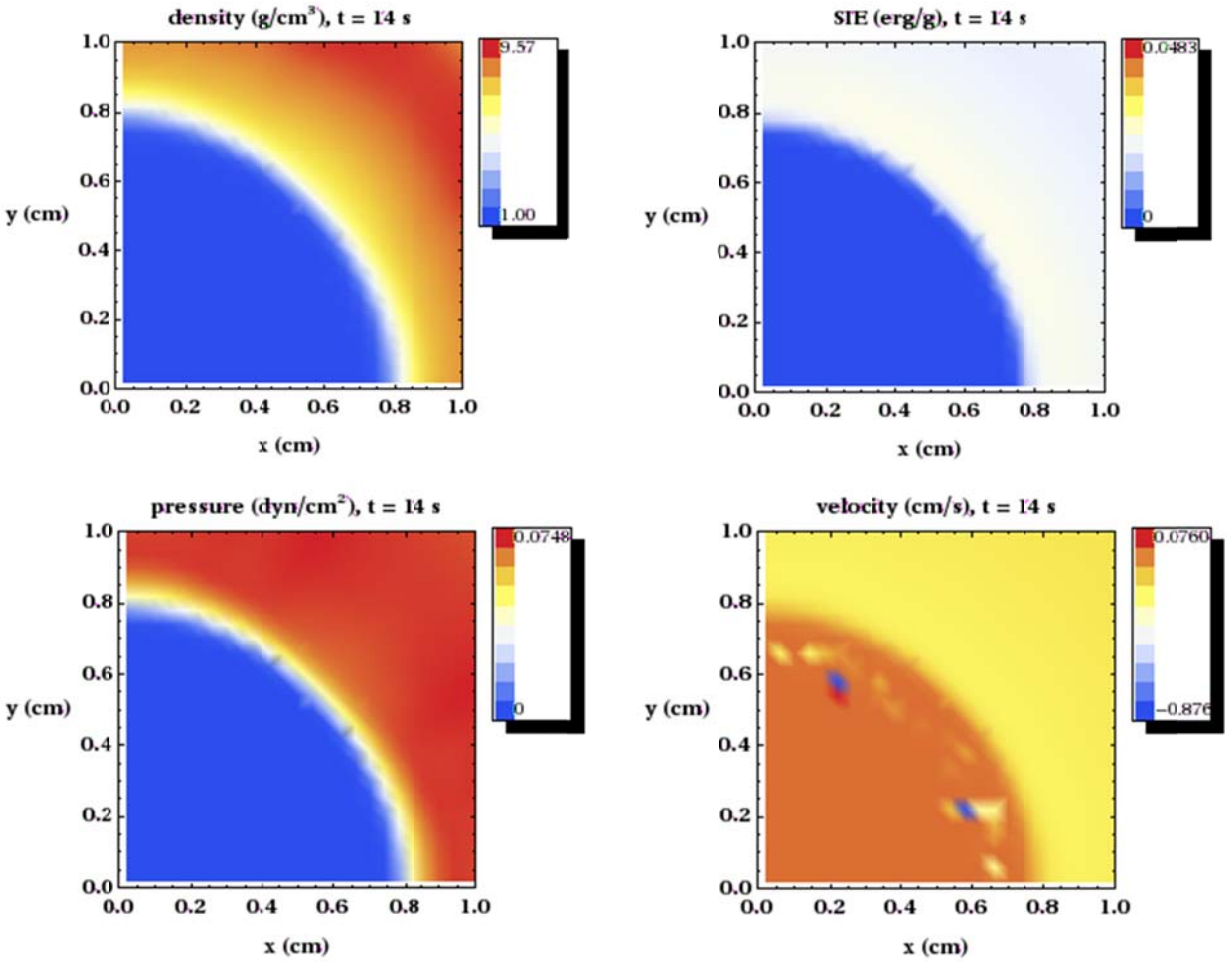

Figure D.1: 2D Cartesian SGP results at *t* = 14 s (converging flow).

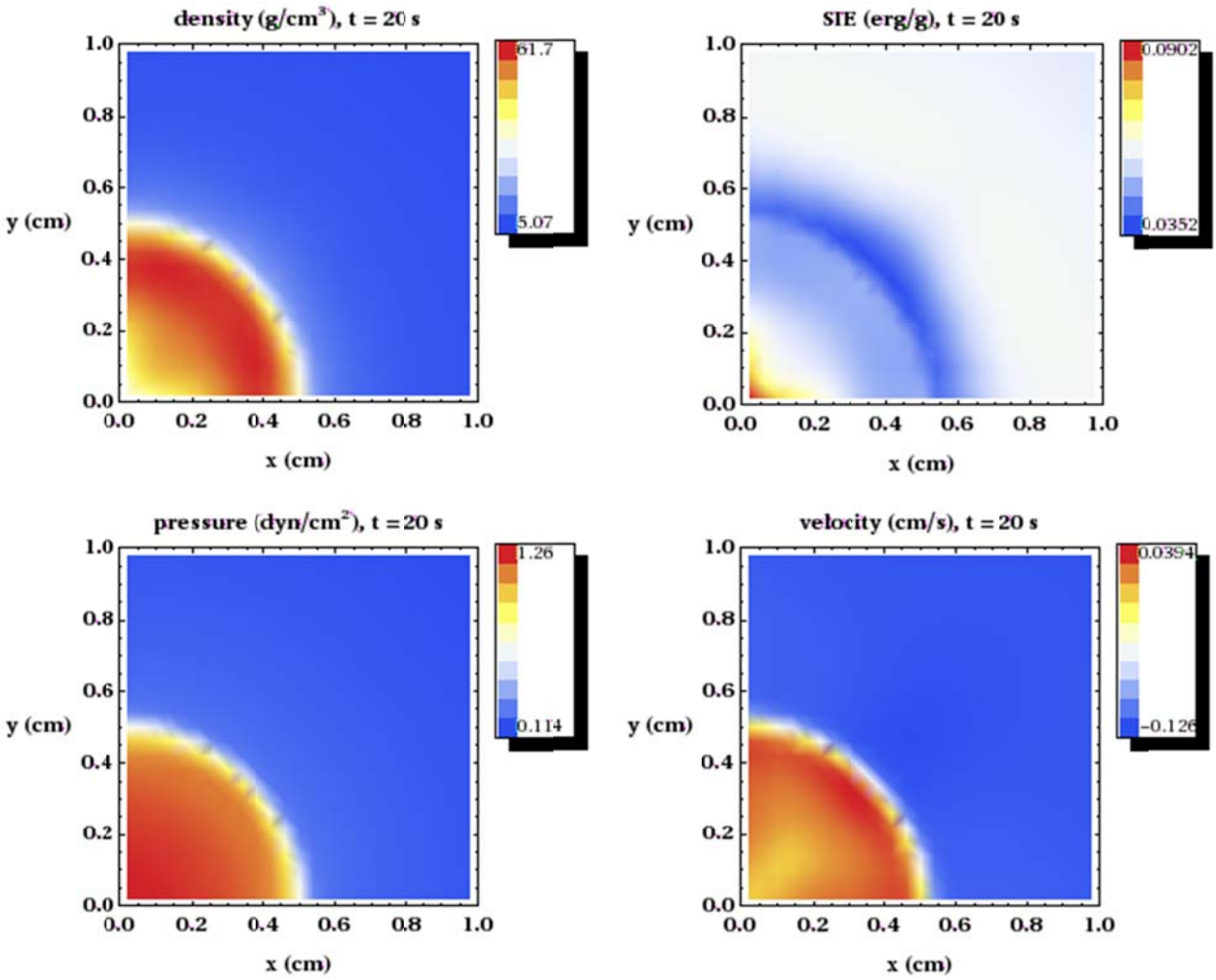

Figure D.2: 2D Cartesian SGP results at *t* = 20 s (diverging flow).

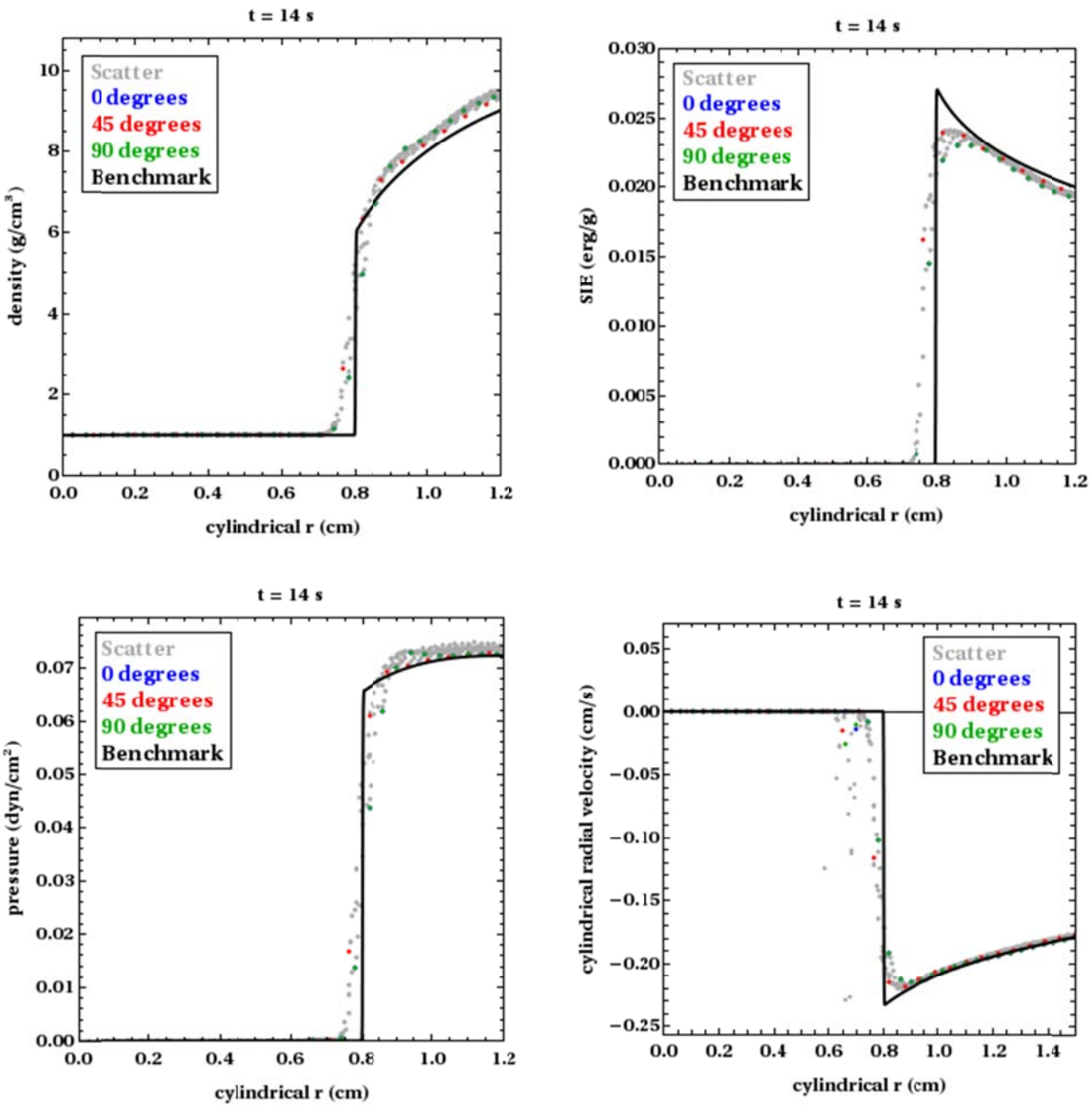

Figure D.3: 2D Cartesian SGP line-out results at *t* = 14 s (converging flow).

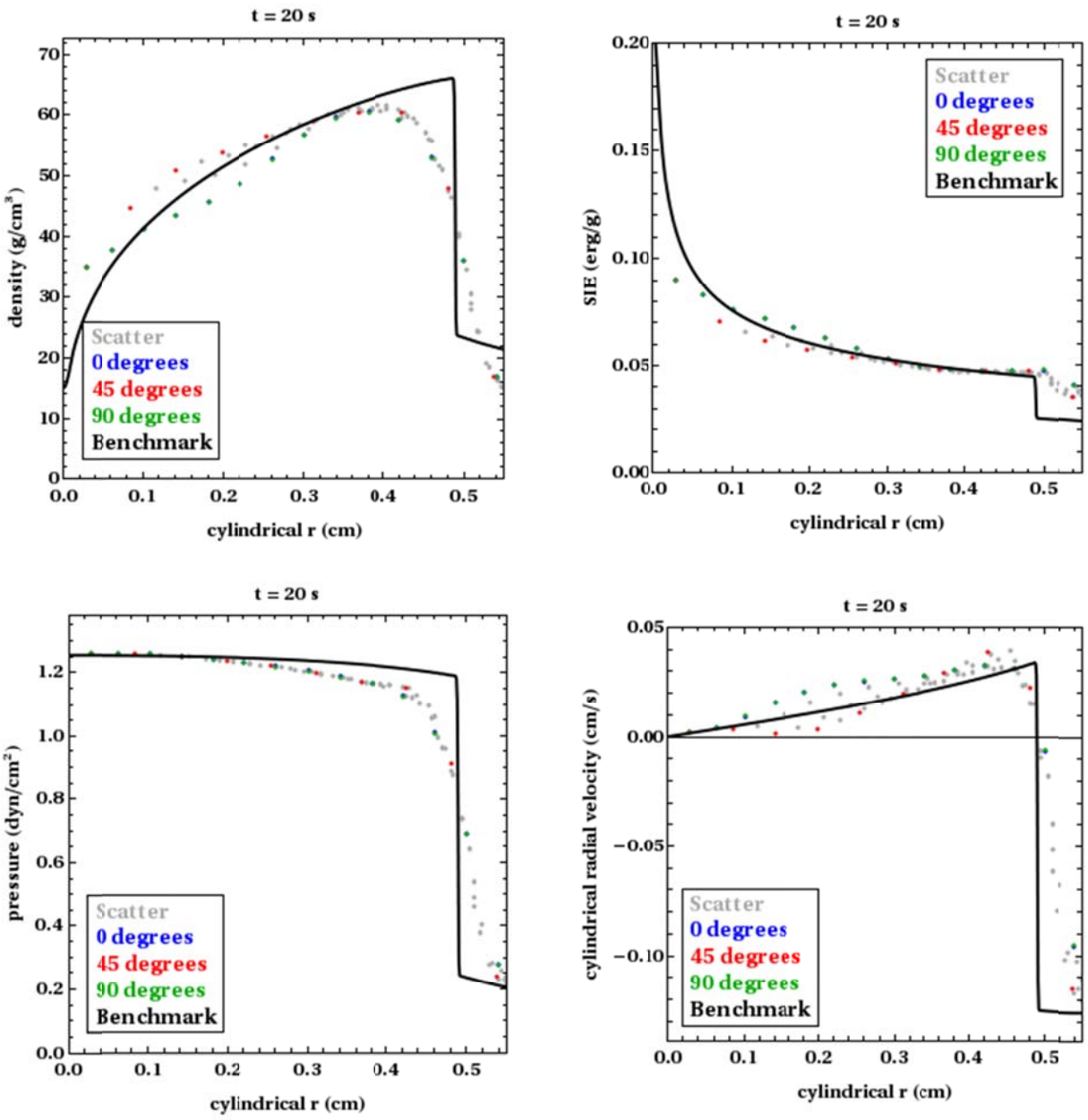

Figure D.4: 2D Cartesian SGP line-out results at t = 20 s (diverging flow).

Figures D.1-D.4 show that flow symmetry is better maintained in the 2D Cartesian (as opposed to the 2D axi-symmetric case). No asymmetric wall heating error is visible in the SIE field at t = 20 s, though a variety of other errors (due to the relatively low grid resolution) are present.

D.2: Adaptive Mesh Refinement

Figures D.5-D.8 show converging regime (Figs. D.5 and D.7) and diverging regime (Figs. D.6 and D.8) results of a 2D Cartesian SGP calculation (with AMR settings enabled), intended only to address the asymmetric wall-heating phenomenon.

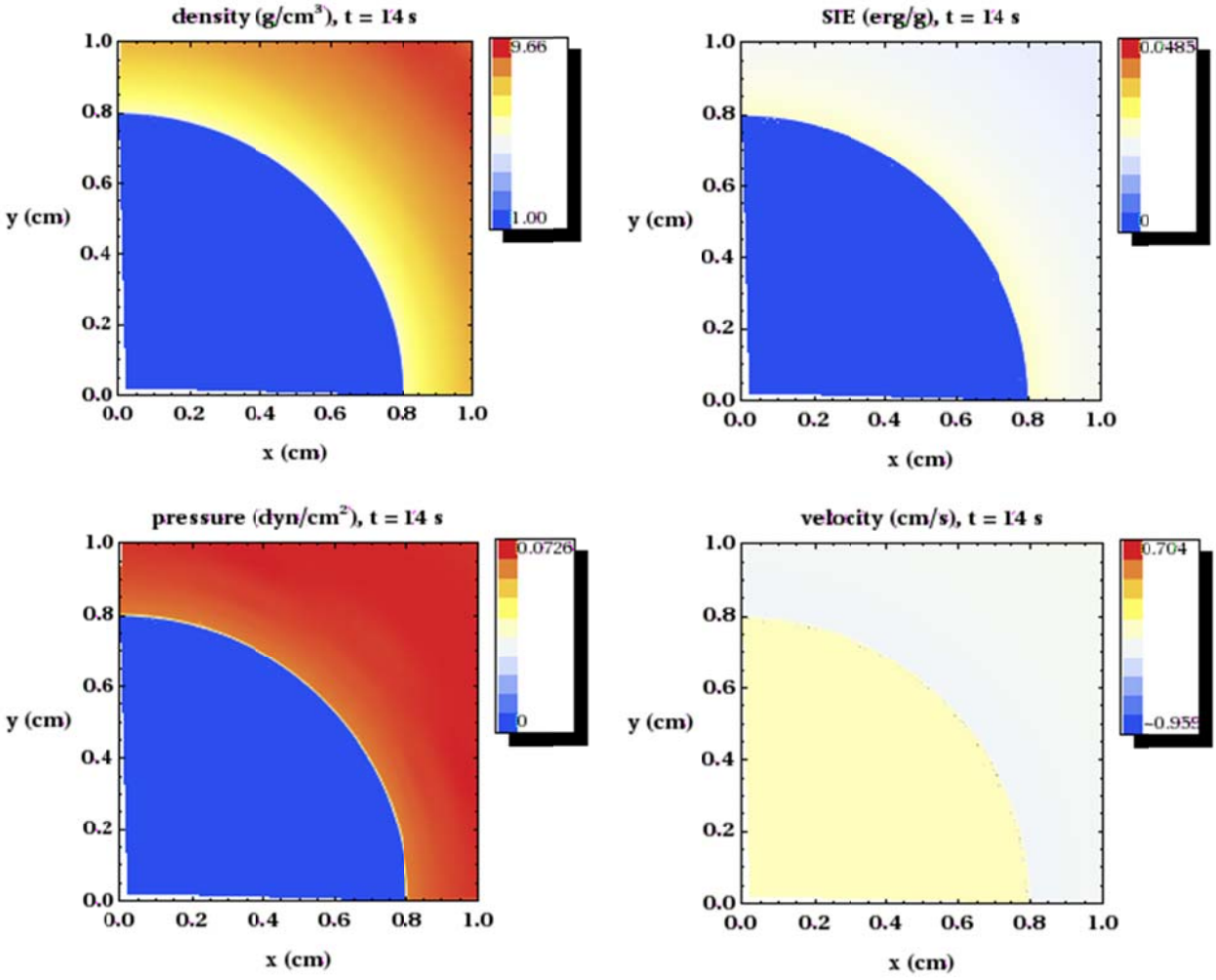

Figure D.5: 2D Cartesian SGP results at *t* = 14 s (converging flow) with AMR.

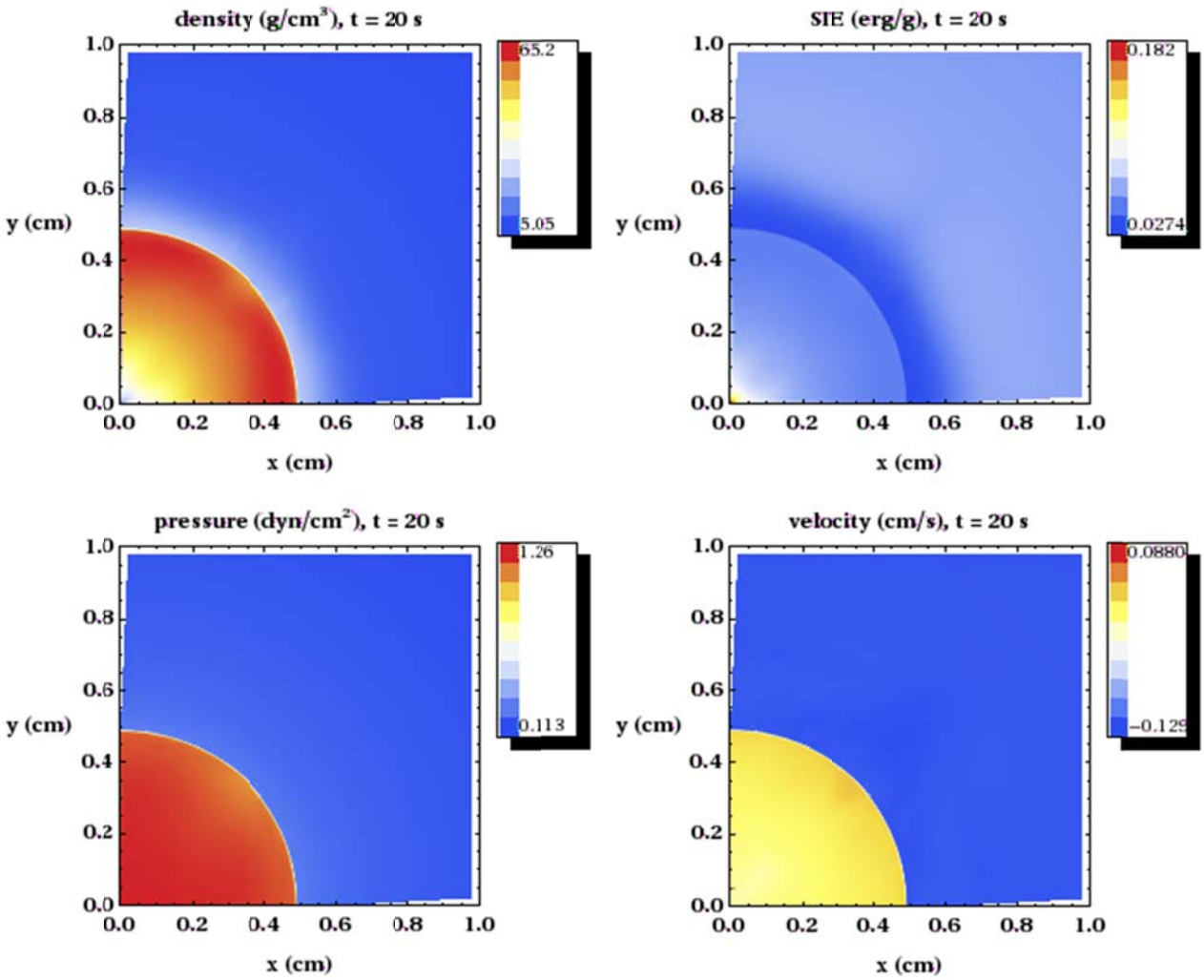

Figure D.6: 2D Cartesian SGP results at *t* = 20 s (diverging flow) with AMR.

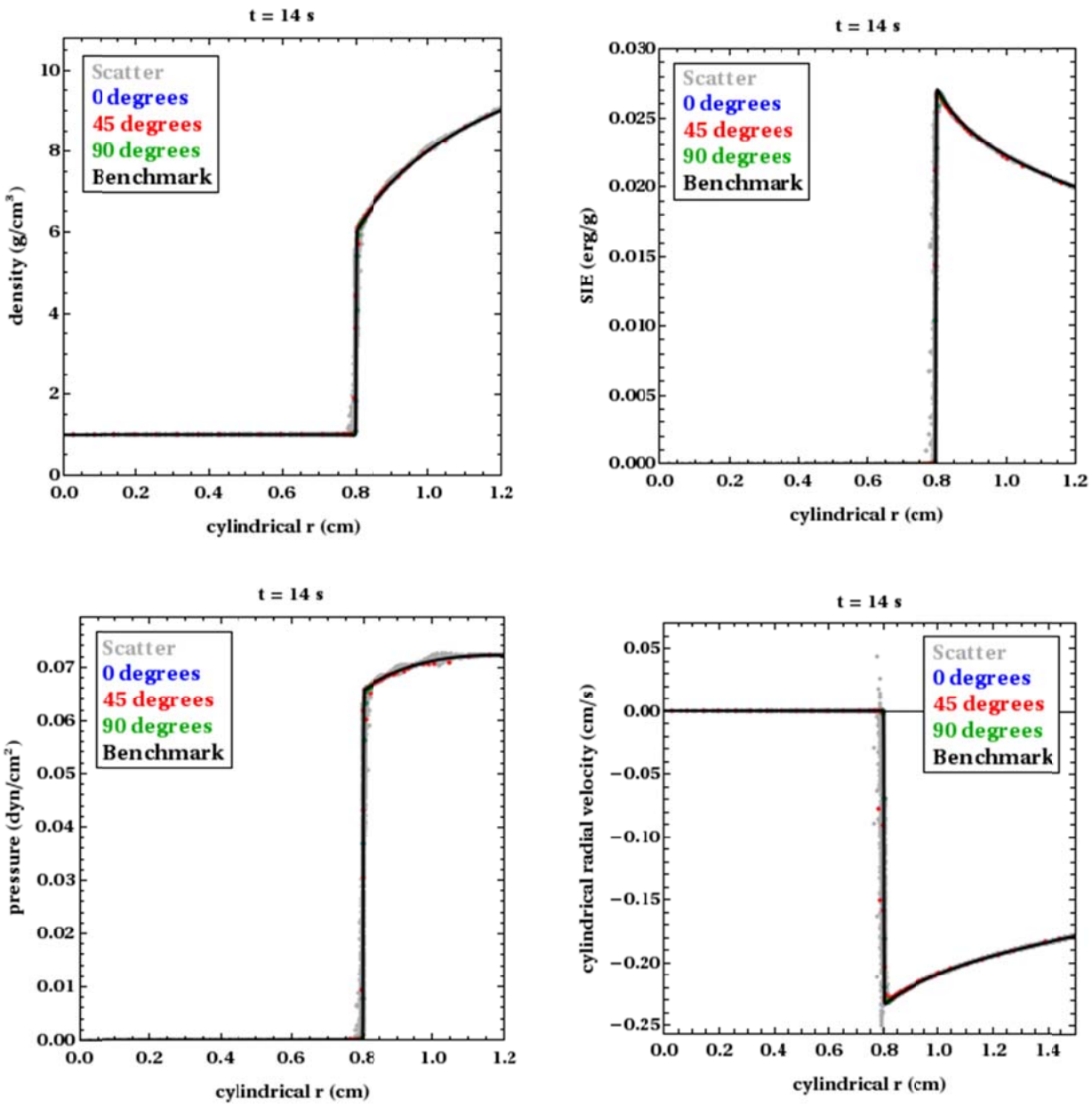

Figure D.7: 2D Cartesian SGP line-out results at *t* = 14 s (converging flow) with AMR.

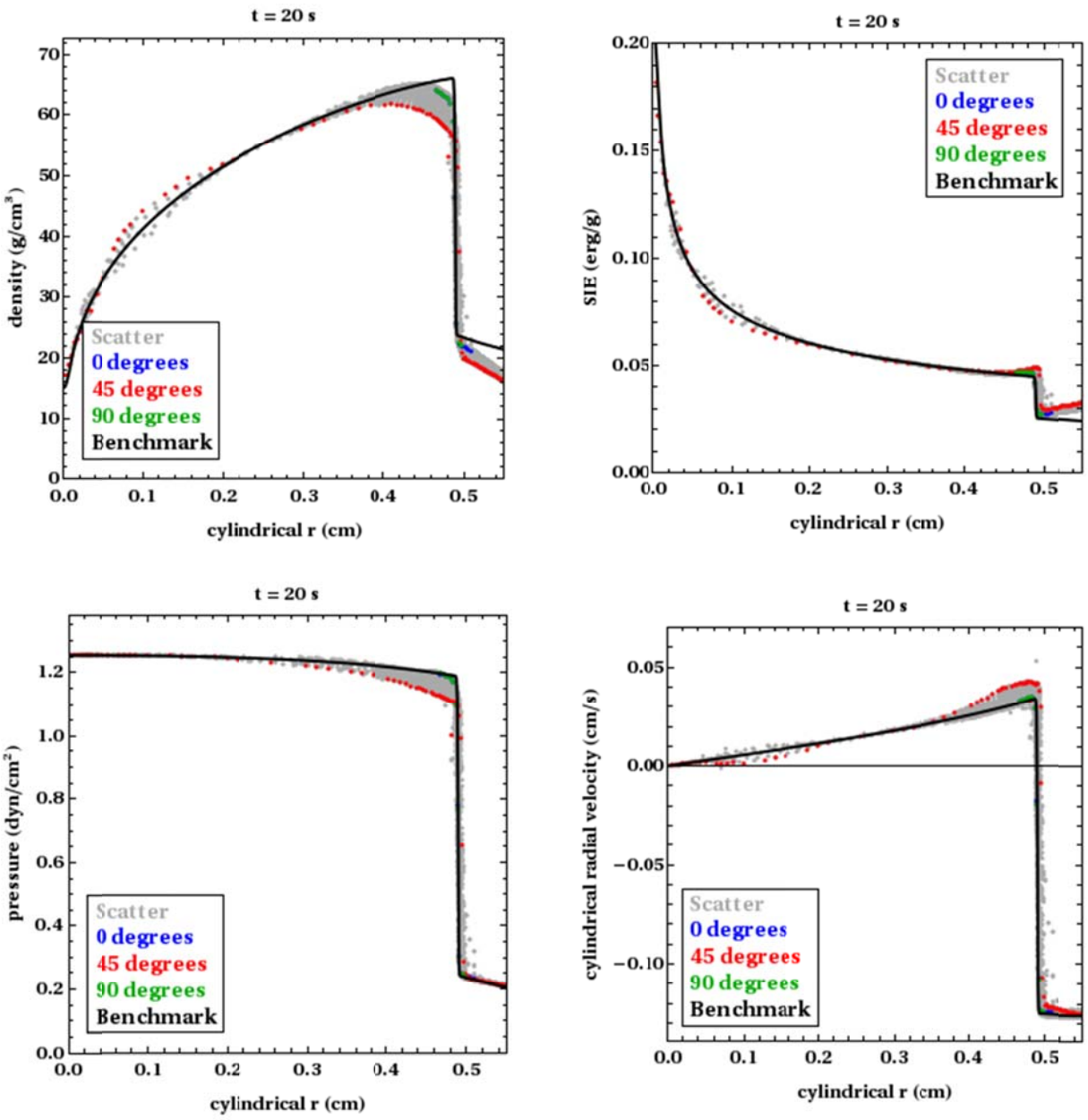

Figure D.8: 2D Cartesian SGP line-out results at *t* = 20 s (diverging flow) with AMR.

Figures D.5-D.8 show that the use of AMR causes much sharper shock profiles to be generated in the 2D Cartesian simulation. As was the previously the case, flow symmetry is better maintained in the 2D Cartesian case (as opposed to the 2D axi-symmetric case). No asymmetric wall heating error is visible in the SIE field at $t = 20$ s. The maximum error in the AMR simulation appears to be found along the 45-degree line.

These results seem to confirm the hypothesis regarding asymmetric wall heating presented in Sec. IV, though additional work must be done to quantitatively assess the quality of the 2D Cartesian result sets.

APPENDIX E: SAMPLE xRAGE INPUT DECKS

E.1: 1D Spherical Symmetry

```
! 1D spherical shock tube problem, gamma = 1.4
! 512000 uniform initial zones over r = (0,10)
! no AMR
! Built by S.D. Ramsey, 1/5/12
!
!-----------------------------------------------------
! CALCULATIONAL CONTROL VARIABLES
!-----------------------------------------------------
!
pname = rsst_no_amr
kread = -1
ncmax = 5000000
tmax = 20.0
tedit = 1.0
dtname = 1.0
dodmpxdt = .true.
ncedit = 0
modcyc = 1000
uselast = .false.
mincellpe = 1
maxcellpe = 1000000
!
dohydro = .true.
doheat = .false.
dorad = .false.
!
!norecon = .false.
!
!-----------------------------------------------------
! ZONING AND AMR SPECIFICATION
!-----------------------------------------------------
!
cylin = .false.
sphere = .true.
!
imxset =  512000
dxset =  1.9531250E-05
!
!numlev = 10
!mxcells = 2000000
!pctdiv = 1.e-3
sizemat(1) = 1.9531250E-05
!
!-----------------------------------------------------
! MATERIAL AND EQUATION OF STATE SPECIFICATION
!-----------------------------------------------------
!
numfine = 1
nummat = 1
keos = 0
matdef(16,1) = 0.4
matdef(30,1) = 1.0
```

```
numreg =  2
!
typreg(1) = 1
diareg(1,1) = 20.0
xreg(1,1) = 0.0
matreg(1) = 1
rhoreg(1) = 6.0
siereg(1) = 0.06
rdreg(1) = 0.0
!
typreg(2) = 1
diareg(1,2) = 8.0
xreg(1,2) = 0.0
matreg(2) = 1
rhoreg(2) = 1.0
siereg(2) = 1.0e-10
rdreg(2) = 0.0
!
```

E.2: 2D Axi-Symmetry

```
! 2D (r,z) spherical shock tube problem, gamma = 1.4
! 1000 x 1000 uniform zones over r = (0,10) and z = (0,10)
! do not include AMR
! Built by S.D. Ramsey, 9/22/11
!
!-----------------------------------------------------
! CALCULATIONAL CONTROL VARIABLES
!-----------------------------------------------------
!
pname = rsst2d_amr
kread = -1
ncmax = 10000000
tmax = 20.0
tedit = 1.0
dtname = 1.0
dodmpxdt = .true.
ncedit = 0
modcyc = 1000
uselast = .false.
mincellpe = 1
maxcellpe = 10000000
!
dohydro = .true.
doheat = .false.
dorad = .false.
!
norecon = .true.
!
!-----------------------------------------------------
! ZONING AND AMR SPECIFICATION
!-----------------------------------------------------
!
cylin = .true.
sphere = .false.
!
```

```
imxset = 1000
jmxset = 1000
dxset = 0.01
dyset = 0.01
!
!numlev = 5
!mxcells = 2000000
!pctdiv = 1.e-3
!
sizemat(1) = 0.01
!
!-----------------------------------------------------
! MATERIAL AND EQUATION OF STATE SPECIFICATION
!-----------------------------------------------------
!
numfine = 1
nummat = 1
keos = 0
matdef(16,1) = 0.4
matdef(30,1) = 1.0
numreg =  2
!
matreg(1) = 1
rhoreg(1) = 6.0
siereg(1) = 0.06
xdreg(1) = 0.0
ydreg(1) = 0.0
xlreg(1) = 0.0
xrreg(1) = 10.0
ybreg(1) = 0.0
yareg(1) = 10.0
!
typreg(2) = 1
diareg(1,2) = 8.0
xreg(1,2) = 0.0
yreg(1,2) = 0.0
matreg(2) = 1
rhoreg(2) = 1.0
siereg(2) = 0.0
xdreg(2) = 0.0
ydreg(2) = 0.0
!
```